Doctoral Dissertation
Doctoral Program in Electronics Engineering (36th cycle)

Integrated Design and Prototyping of a 77 GHz Medium Range Radar Into a Car Rear Lamp

By

Mattia Caffa

******

Supervisor(s):
Prof. Riccardo Maggiora, Supervisor, Politecnico di Torino

Politecnico di Torino
2024

Declaration

I hereby declare that, the content and organization of this dissertation constitute my own original work and do not compromise in any way the rights of third parties, including those relating to the security of personal data.

Mattia Caffa
2024

* This dissertation is presented in partial fulfillment of the requirements for **Ph.D. degree** in the Graduate School of Politecnico di Torino (ScuDo).

Acknowledgements

I would like to spend some words to thank the people who were fundamental to me during these years.

First of all, I would to thank my family for their unwavering support in my decision to pursue further studies and follow my love for engineering.

I would like to thank my advisor Riccardo Maggiora for his guidance, and teaching during the PhD period. His relentless drive to turn ideas into tangible hardware and applications, and his passion for applied research have been both inspiring and enlightening.

I would like to thank Maurice, Stefano, Sara, Gianluca, Daniele, Francesco, and Daniela for the good times spent in the lab, hard-working but also laughing together.

I would like to thank my friends which I can always count on to have support and have fun with.

And, I would like to thank Silvia for her patience and understanding during the writing of this thesis. I am grateful for her constant support, for the countless memorable moments we spent together, and for her presence that makes my everyday life brighter. I am extremely fortunate to have her by my side.

Thank you everyone for being part of this journey.

Summary

The continuing trend towards an increase in the frequency used for automotive radar applications has allowed an overall increase in performance and a reduction of the dimensions of this type of device. This last feature could permit new ways of installation with respect to the standards adopted today by car manufacturers (behind bumpers or in car bodies). Instead of considering the radar as an external device to be installed on the car it could be part of the initial project and included into the design process of a plug-in part.

In this thesis, the integrated design and prototyping of 77 GHz automotive radar into a modern car rear lamp is presented. The radar Printed Circuit Board (PCB) was designed to fit into the lamp without affecting the external look; the optimization of the material thickness of the radar cover and temperature tests have been performed on the system. The embedded radar processing was implemented on a monolithic chip to perform target tracking and the main processing steps are reported.

The results obtained from tests in controlled environments and on the road in traffic scenarios show that including the radar into the design of a lamp from the beginning is a feasible solution. This approach brings some advantages such as improved placing and connections, an undisturbed view, better protection from disturbances and accidents, etc., and provides more customized solutions for car makers.

In Chapter 1 an overview of Advanced Driver-Assistance Systems (ADAS), automotive radar fundamentals, state of the art, and motivations for the project are presented. In Chapter 2 the radar housing and the hardware design choices for the implementation of the integrated radar prototype into the rear lamp are discussed. In Chapter 3 the description of the fully developed radar firmware and the algorithm solutions for different critical points of the applications is presented. In Chapter 4 some of the results obtained in the laboratory, during the tests carried out in the open field, and during the tests carried out on the road in traffic scenario are shown. The results obtained during the test campaign carried out with the radar installed on the

host car are also presented. In Chapter 5 a proposal for more effective modulations for automotive radar waveforms and relative experimental results are presented.

Contents

List of Figures

List of Tables

Chapter 1

Advanced Driver Assistance Systems and Automotive Radar Fundamentals

In recent years, the significance of automotive safety has grown substantially, due to the high numbers of fatal accidents. Since one of the main contributors to these accidents is human error, the trend is to automate and enhance safety technologies to assist the driver and avoid dangerous situations. These safety technologies are called Advanced Driver Assistance Systems (ADAS) and they implement various functionalities such as automatic emergency braking, blind-spot detection, adaptive cruise control, and many more. Many of these functionalities are implemented through the use of radar (an acronym for "Radio Detection and Ranging") sensors, cameras, and lidar (an acronym for "Light Detection and Ranging") sensors.

Radar technology has a key role in the future of ADAS. Indeed, compared to other sensor types, it is the best performing in the largest number of scenarios, especially in non-optimal weather conditions (lidar primary weakness) and when in the dark (differently from camera) as graphically represented in Fig. 1.1 where comparative spider diagrams are reported for each sensor type. With respect to lidars, radars have better performances regarding observable range. While automotive radars can detect objects at distances less than 1 m and up to 350 m, lidars struggle to detect very close targets. Today, automotive radars are millimeter wave sensors (with wavelength $\lambda = 4$ mm) while lidars use infrared light (with $\lambda = 1550$ nm). The range resolution of radar systems depends on the bandwidth of the transmitted signal and is typically inferior to that of lidars. However, newer technologies will permit the construction of higher-frequency radars, enhancing this feature. Lidars also perform much better in terms of angular resolution due to their shorter wavelength and scanning pattern.

(a) Radar (b) Camera

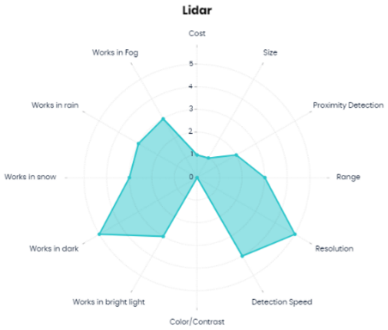

(c) Camera

Fig. 1.1 Automotive Sensors Pros and Cons

Automotive radar angular resolution due to the use of beamforming and Multiple Input Multiple Output (MIMO) techniques depends on the number of antennas and is usually lower with respect to lidars. Another point of strength of radars is their size which allows an easier integration into the car; as a counterpart lidars are bulky and their installation usually affects the appearance of the vehicle. Even if lidar's production cost is decreasing, radars are today way cheaper. The trade-off with cost is very relevant since 10 to 16 sensors are expected to be installed around future vehicles to provide a 360° view of the surroundings. A possible configuration of the sensors for future ADAS is shown in Fig. 1.2 where a mix of medium range radars, short range radars and cameras is used to cover the corners, the side, and the rear of the vehicle; a long range radar sensor together with a lidar sensor covers the front and ultrasound sensors are used for parking.

To implement a fully autonomous vehicle, driver assistance technology will have to progress through 5 levels of automation:

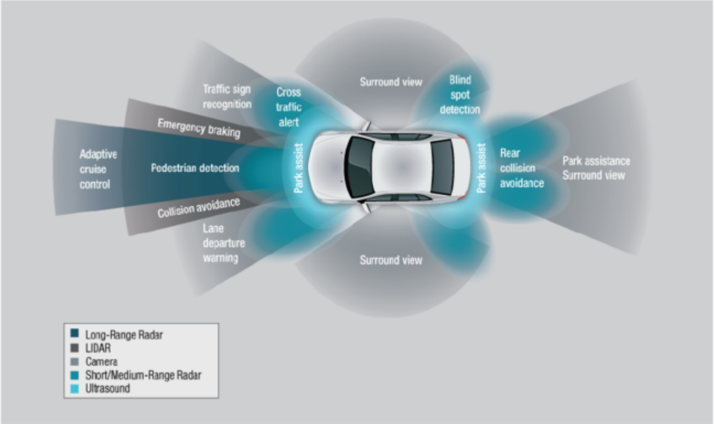

.

Fig. 1.2 Sensors configuration in future ADAS system

- Level 1 (Feet off): single automated systems for driver assistance such as steering or accelerating (cruise control). The driver controls the other aspects of driving.

- Level 2 (Feet/Hands off): The vehicle can control steering and accelerating/decelerating. The driver must pay attention and can take control of the car at any time.

- Level 3 (Eyes off): the vehicle has environmental detection capability utilizing sensor fusion and it can perform driving tasks. Driver override is still required in certain situations.

- Level 4 (Mind off): with respect to level 3, level 4 cars can intervene in critical situations, they can avoid obstacles, and overtake other vehicles.

- Level 5 (Driver off): level 5 autonomous driving requires no driver interaction. Vehicles can steer, accelerate, brake, and monitor road conditions like traffic jams.

Currently, a lot of vehicles on the market have reached level 1, some Original Equipment Manufacturers (OEMs) are selling level 2 vehicles, and the first level 3 vehicles (level 3 auto-pilot which is available at speeds up to 40 mph) have been certified and are entering the market. To achieve levels 4 and 5 of ADAS, which is foreseen to happen after 2030, an increasing number of sensors around the vehicle including radars, cameras, and lidars must be considered.

1.1 State of the Art

As already mentioned, with respect to other sensors, radars have better immunity to weather conditions, longer observable range, low cost, good range resolution, small dimensions, and accurate target position estimation; radar technologies have been actively investigated to enable future ADAS and intelligent transportation systems [1].

Different modulation schemes for radar waveforms have been studied and adopted: the Frequency Modulated Continuous Wave (FMCW) [2] is the most popular for automotive applications due to its ease hardware requirements and low costs, but more recently digital modulation raised in popularity in the form of Orthogonal Frequency Division Multiplexing (OFDM) [3], and Phase Modulated Continuous Wave (PMCW) [4], also thanks to their ability to exploit Joint Communication and Radar Sensing (JCRS) [5], [6]. Each of these modulation have some advantages and disadvantages which have been analyzed in [7], [8], and [9].

Radars can be classified into Short-Range Radars (SRRs), Medium-Range Radars (MRRs), and Long-Range Radars (LRRs) based on their observable range. Each type of radar can cover different ADAS functionalities, for example, LRRs are suitable for Adaptive Cruise Control (ACC). MRRs are good for Lane Change Assist (LCA), Cross Traffic Alert (CTA), and Blind Spot Detection (BSD). SRRs are used for parking and proximity detection [10].

The increasing request to improve angular resolution in automotive radar to separate distant targets is a challenge that has been addressed using the MIMO technique [11] which creates a receiving virtual antenna array that contains a large number of elements and has a larger aperture than the array of physical receiving elements through the use of orthogonal transmit waveforms [12]. This technique is heavily relied upon for automotive radars [13] and recently different high-resolution imaging radars with cascaded radar chips and a very high number of transmitting and receiving virtual elements (over 2000) have been presented [14], [15], [16].

Another solution that has been investigated and still is a topic of research is the adoption of radar-distributed networks [17], [18]. Distributed radar networks allow the achievement of greater aperture sizes and enable finer angular resolution but they require heavy centralized processing and synchronization.

1.2 Motivations and Proposed Solution

Automotive radars are usually installed on cars as external black box devices to be connected to vehicle Controlled Area Network (CAN) bus. The standard placement for automotive radar sensors is in tight spots behind bumpers or emblems [19]. While this offers protection to the antenna and does not affect the exterior design of the vehicle, it introduces different points of concern for the car maker. For example, long cables need to be laid in the chassis, ad hoc spots need to be created in the car body, and radome and painting effects must be evaluated and mitigated.

The incorrect spacing between the bumper (usually a multi-layer structure) and the antenna can lead to multiple reflections. These reflections affect range and velocity estimation [20], worsen the direction of arrival estimation, and degrade the Field of View (FOV) [19]. Another drawback of the bumper is the presence of mud and/or dust and ice or snow accumulating in front of the sensor which introduces disturbances that increase the noise floor and reduce detection performances as shown in the contaminated radome attenuation data reported in [21].

A part of the vehicle that has been in the discussion for the placement of radar sensors is the lamp [22]. Usually, car lamp materials are thinner, adjustable, and without painting bringing consistent advantages to the above-mentioned problems. Lamp housing offers higher protection from external disturbances, better protection in case of minor accidents, and eliminates the need for extra cables.

In [23], the projection lens of a lighting unit is used as an electromagnetic lens for a millimeter wave radar with waveguide antennas. In [22], an antenna integration inside a headlamp for automotive radar applications is presented. The antenna comprises the feed, which is embedded within the electronic unit, and a reflector made of transparent materials.

The project for this Thesis is the design and prototyping of a 77 GHz FMCW automotive corner MRR integrated with a rear lamp without affecting the external look of the lamp itself and its lighting functions. The lamp mechanics and electronics were realized by Magna Lighting. The corner MRR was installed on the car as depicted in Fig. 1.3 to cover the blind spots. The radar was designed to have characteristics in line with typical MRR on the market with a maximum observable range between 60-100 m, a range resolution better than 50 cm, a pointing angle of 35-45°, an azimuth field of view ±70° in the close range that it is reduced to ±5° at the maximum range.

Corner radars are necessary for BSD and LCA applications since they cover an area that a rear sensor, dedicated to reaching further distances, cannot cover with its own field of view. The BSD is a system that warns the driver if another vehicle is located in the spots (that goes from the side to the rear corners of the vehicles) that a rear-view mirror does not cover. The LCA is a system that warns the driver if a change of lane is not possible by detecting closing vehicles with higher relative velocities on adjacent lanes. An MRR corner radar, together with other SRR sensors, can also be helpful in a CTA application. The CTA is a system that warns the driver if a vehicle or a person is crossing behind the host vehicle. This type of system is used especially when getting out of parking with low visibility of the street behind.

Fig. 1.3 Medium Range Corner Radar

The integrated design aims to combine the advantages of placing the radar into the rear lamp while also optimizing the radar performances by means of tuning PCB electronics, material thicknesses, position and geometry of the antennas, customizing the software, and improving thermal dissipation.

The radar installation into the rear lamps together with other sensors around the car would allow to achieve a comprehensive 360-degree view all-around the vehicle's surroundings.

1.3 FMCW Radar

The conventional modulation of automotive radar waveforms adopted by manufacturers in recent decades is the FMCW. The adoption of different modulations for future automotive radars is a current topic of research and will be discussed in this work in Chapter 5. A description of the FMCW radar principles, and signal processing is provided in the following paragraphs.

An FMCW radar periodically transmits a certain number of linearly frequency-modulated waveforms called chirps. Fig. 1.4 shows the chirp behavior: the chirp of duration T_c is modulated with increasing or decreasing frequency starting from the frequency f_0 and has a bandwidth $B = ST_c$ where S is the frequency slope of the modulation; as the frequency increases, the chirp oscillation accelerates in the time domain.

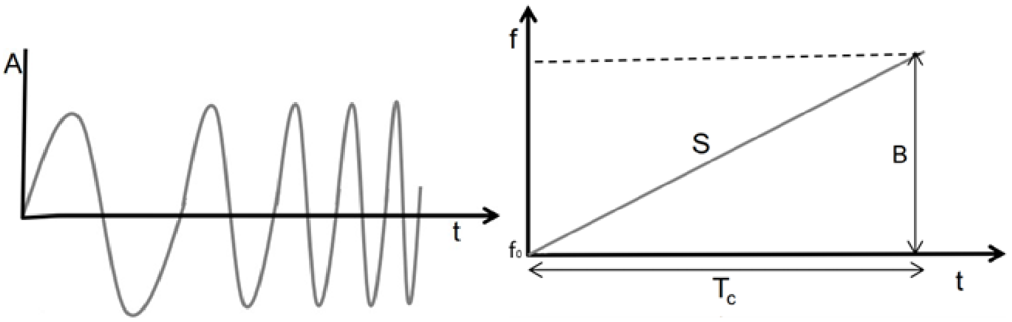

(a) Chirp in time domain (b) Chirp frequency vs time plot

Fig. 1.4 Chirp Signal

The transmitted chirp can be written as a function of time as,

$$s_{TX}(t) = exp(j2\pi f_0 t + j\pi \frac{B}{T_c} t^2) \tag{1.1}$$

The ideal scattered signal received from a target at the boresight and at distance R, after a propagation delay $\tau = 2R/c$, where c is the speed of light, and with a relative radial velocity $v = \frac{\lambda f_d}{2}$ with respect to the radar, where λ is the wavelength and f_d the Doppler frequency is

$$s_{RX}(t) = As_{TX}(t - \tau) exp(j2\pi f_d t) \tag{1.2}$$

where A is the amplitude of the received signal.

After mixing the received signal with the transmitted signal, the low-pass filtered beat-frequency signal is obtained,

$$s_{RXm}(t) = Aexp(-j2\pi(\frac{B\tau}{T_c} - f_d)t) exp(j\pi \frac{B\tau^2}{T_c} - j2\pi f_0 \tau). \tag{1.3}$$

The signal is sampled with the Analog-to-Digital Converters (ADCs). The first exponential of eq. 1.3 contains the target information of range and Doppler. The second exponential is a phase term which is time-invariant, it is constant across all Fast Fourier Transform (FFT) samples, and it does not influence the range and Doppler calculation. The range response of the radar is derived by calculating an FFT on the beat-frequency signal. As it is clear from eq. 1.3, in the beat frequency signal the Doppler (f_d) and range information(τ) are coupled together. For this reason, other techniques as the transmission of multiple chirps are required to measure target velocities.

A block diagram of the hardware required for an FMCW radar is reported in Fig. 1.5. A synthesizer generates the ramp which is transmitted and then mixed with the received signal. The mixed signal is then low-pass filtered, sampled, and converted to the digital domain and processed to extract information from the detection.

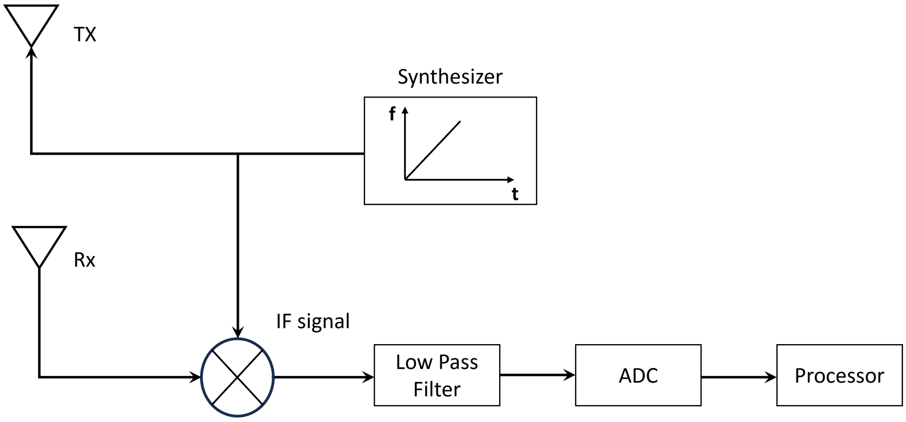

Fig. 1.5 FMCW block diagram

The result of this process can be better understood by observing Fig. 1.6 where the frequency vs time behavior of the transmitted and received chirps and intermediate frequency (IF) is reported. After the mixing of the transmitted and received chirps, a constant frequency tone $IF = S\tau$ of duration $T_t = T_c - \tau$ is obtained. For automotive applications, where maximum ranges are typically in the order of a few hundred meters, usually $\tau << T_c$ and $T_t \simeq T_c$.

Fig. 1.7 shows the sequence of N chirps that an FMCW radar transmits with a pulse repetition frequency $PRF = \frac{1}{T_c}$ and total duration $T_f = NT_C$ which is usually called frame; a frame is required for a single range-Doppler detection of the targets; successive frames are transmitted periodically to perform sequential detections.

The Doppler of the targets modulates all the chirps with a sine wave of frequency $f_d = \frac{2v}{\lambda}$, which modifies the phase of the sequential chirps but not their frequency ($f_d <<< \frac{1}{T_C}$). The Doppler frequency can be extracted with a second FFT, calculated

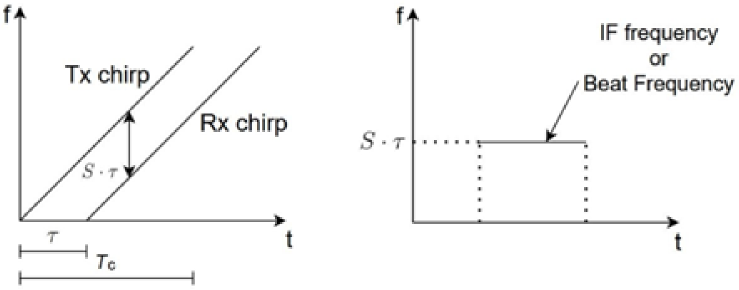

Fig. 1.6 Beat frequency signal obtained after mixing

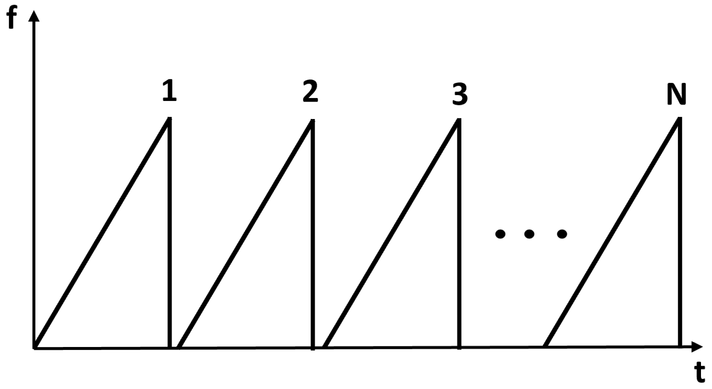

Fig. 1.7 Radar Frame

per each range bin along the different chirps in the frame, thus obtaining the target velocity.

The two most important parameters for a radar are the resolution and the maximum limit for the quantity that needs to be measured. Resolution is the minimum distance at which two targets can be separated in a certain dimension.

From the analysis of the signal, these two values can be obtained for both range and velocity. The minimum variation in the intermediate frequency that can be measured is the inverse of the observation time T_C. The range resolution R_{res} is

$$R_{res} = \frac{c}{2ST_c} = \frac{c}{2B}. \tag{1.4}$$

where c is the speed of light and B is the bandwidth. Eq. 1.4 shows that the range resolution is only dependent on the bandwidth of the chirp. The radar signals are always sampled by ADCs that have limited sampling frequencies (F_s). Since Nyquist theorem needs to be respected for proper acquisition of the signal, assuming I and Q sampling the maximum range is

$$R_{max} = \frac{F_s c T c}{2B}. \tag{1.5}$$

Since the targets' velocity causes a phase variation in the IF signal, the velocity resolution (v_{res}) of the radar depends on its capability of separating phase differences. The phase difference measured along two successive chirps due to an object moving at speed v is

$$\Delta\Phi = \frac{4\pi v T_c}{\lambda}. \tag{1.6}$$

Knowing that an FFT applied on a sequence of length N (number of chirps) can separate two frequencies as long as their $\Delta\Phi = \frac{2\pi}{N}$, it can be shown that v_{res} depends only on N and T_c and therefore only on the frame duration, and is

$$v_{res} = \frac{\lambda}{2NT_c} = \frac{\lambda}{2T_f}. \tag{1.7}$$

The maximum measurable velocity is instead limited by the fact both positive and negative variations need to be measured (closing and opening vehicles). The measure is unambiguous only if the phase variation is $\Delta\Phi < \pi$ and it is

$$v_{max} = \frac{\lambda}{4T_c}. \tag{1.8}$$

In this case, the maximum velocity depends only on the chirp duration. Hence, if T_c is reduced to improve v_{max} the velocity resolution is worsened. The only alternative is to increase the number of chirps N at the cost of active transmission duty cycle and heavier processing.

The Angle of Arrival (AoA) of the scattered signal by targets can be measured by means of beamforming or MIMO techniques. Both of these techniques require multiple transmitters (TX) and/or multiple receivers (RX). To apply beamforming, multiple RXs (or TXs) are required and a phase shift dependent on the RX (or TX) positions is applied to the received signal in the analog or digital domain. For the beamforming case, the AoA resolution depends on the number of RXs (or TXs).

In the MIMO case, the same angular resolution can be obtained with a reduced number of RX antennas but also multiple TXs are required to create a virtual array. In the case of a uniformly spaced MIMO array, the AoA resolution depends on the product of the number of TX and RX.

The disadvantage of this method is that the signals from different TXs need to be orthogonal in order to be distinguishable at the RX side. The most common method to achieve orthogonality is time division multiplexing (TDM). For TDM, the signals are separated in time, and the transmission is alternated with 1 TX at a time.

Usually, uniform virtual arrays with N elements equally spaced at a distance d are exploited. The maximum Field of View (FOV) that can be covered by antennas spaced apart of a distance d is

$$\theta_{max} = \sin^{-1}(\frac{\lambda}{2d}). \tag{1.9}$$

From eq. 1.9, it is straightforward to derive that the maximum FOV is obtained for $d = \frac{\lambda}{2}$ for which $\theta_{max} = 90°$. The angular resolution (θ_{res}) of a uniform virtual array is dependent on the angle of arrival, θ, and is

$$\theta_{res} = \frac{\lambda}{Ndcos\theta}. \tag{1.10}$$

Angular resolution is usually quoted assuming $d = \frac{\lambda}{2}$ and $\theta = 0°$, resulting in an angular resolution

$$\theta_{res} = \frac{2}{N}. \tag{1.11}$$

Chapter 2

System Description and Hardware Design

2.1 Radar Housing

The rear lamp selected for the integrated design is reported in Fig. 2.1. The mounting angle of the rear lamp is 35° with respect to the car axis making it suitable for a corner radar installation. The rectangular part indicated by the arrow, hereafter referred to as the 'petal', is illuminated from below with Organic Light-Emitting Diode (OLED) technology and was selected to host the radar board. The petal dimensions are 60 mm X 29 mm which is an extremely small area and this is the constraint for the radar board dimensions.

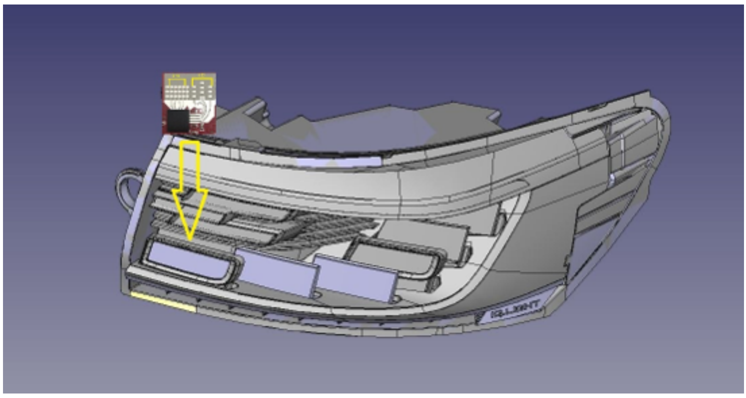

Fig. 2.1 Target rear lamp and radar positioned behind petal

The target application for this prototype was a corner MRR with a maximum vehicle detection range of 75 m. To not affect the design and the lighting, the radar board was placed behind the petal. The radar board was connected to a second dedicated board designed for radar power supply.

A section of the lamp structure in front of the radar is shown in Fig. 2.2. The petal has two layers of different materials and thicknesses and an outer lens in front of it.

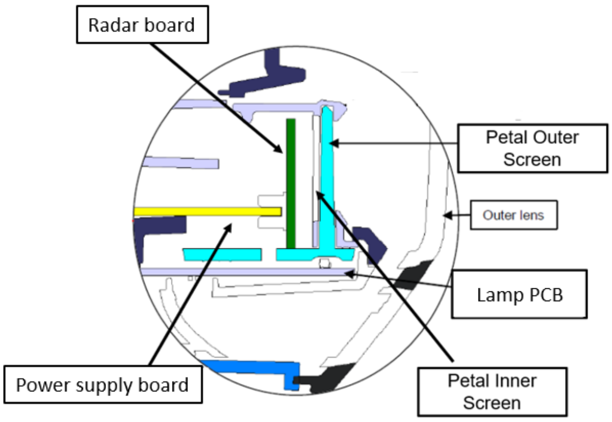

Fig. 2.2 Transverse cut of the lamp in front of the radar

The transmission coefficients (S_{21}) of the outer lens, the petal outer and inner screen were measured in the 60-90 GHz frequency band in order to evaluate their relative dielectric constant (ε_r) and loss tangent ($\tan\delta$).

The setup for this measurement is reported in Fig. 2.3 and consisted of:

- Two equal horns with 10 dB gain, positioned 10 cm apart.
- A vector network analyzer connected to both TX horn and RX horn.
- A planar sample of the Material Under Test (MUT) with an area that was large enough to reduce edge effects positioned between TX horn and RX horn.

Specific for the measurement:

- Direct and diffracted contributions were separated by time gating procedure.
- Transmission coefficient was measured in a wide frequency range (to allow accurate time gating) normalized to the case without the sample.
- Measurement bandwidth was 30 GHz (E-band), resulting in a gating resolution of 0.03 ns, thus allowing ripple mitigation.

The S_{21} entry of the S matrix was measured in phase and magnitude, at first with free space (air) in between the antennas and then with the MUT panel. By comparison of the two measurements both the values of ε_r and $\tan\delta$ can be calculated. Phase measurements were compared to theoretical values and ε_r for normal incidence ($\theta_i = 0°$) was obtained from the theory of stratified media. The transmission coefficient of the slab structure composed of air-MUT-air (S_{21s}) was estimated considering normal incidence and treating the incident field on the material as a plane wave. The S_{21} element of the S matrix of a lossless slab structure with three media and refractive indexes n_1, n_2, n_3 and $n_1 = n3$

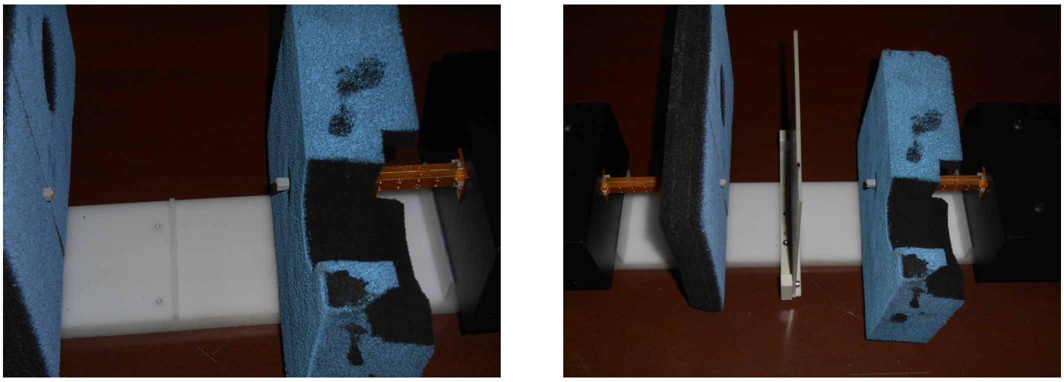

(a) S_{21} Measurements without MUT

(b) S_{21} Measurements with MUT

(c) Measurements setup

Fig. 2.3 Set-up for the measurements of the transmission coefficient to calculate ε_r and $\tan\delta$ of MUTs

$$S_{21} = \frac{(1-\Gamma_{12})^2 e^{-j2\Psi}}{1-\Gamma_{12}^2 e^{-j2\Psi}} \tag{2.1}$$

where Γ_{12} is the Fresnel reflection coefficient at the interface between media 1-2 and Ψ is the propagation factor. For a general interface with n1<n2 the Fresnel reflection

coefficient is

$$\Gamma_{12} = \frac{n2 - n1}{n2 + n1}. \tag{2.2}$$

Since the refractive index of air is $n_1 = 1$, the refractive index of the MUT, n_2, that satisfies the phase relation between the S_{21} measured with and without the MUT can be found. Since the measured materials are plastic once, the magnetic permeability is $\mu_r = 1$ and the dielectric constant can be calculated as

$$\varepsilon_r = \frac{n^2}{\mu_r} = n^2. \tag{2.3}$$

Once the lossless S_{21s} is known, thanks to the magnitude measurements of the S_{21} with and without MUT the attenuation due to dielectric loss of the MUT can be calculated. The value of $tan\delta$ is derived by comparing the measured value of transmission coefficient S_{21m}, obtained knowing the MUT length (MUT_l) with the contribution given by the lossless slab structure and the dielectric. The measured $\tan\delta$ is the value for which the relation

$$S_{21m_{dB}} = \alpha_{L_{dB}} MUT_l + S_{21s_{dB}} \tag{2.4}$$

is verified, and where

$$\alpha_{L_{dB}} = \frac{27.3\sqrt{\varepsilon_r}\tan\delta}{\lambda_0} \tag{2.5}$$

is the attenuation in dB/length due to dielectric losses.

The results of the measurement obtained with the MUT thicknesses of the original petal are reported in Table 2.1.

Table 2.1 Lamp materials thickness and dielectric properties

Part	Thickness	ε_r	$tan\delta$
Outer Lens	3.5 mm	2.62	0.004
Petal Outer Screen	2.8 mm	2.43	0.004
Petal Inner screen	1.17 mm	2.82	0.004

The reflection coefficient of the slab structure composed by air-MUT-air (S_{11s}) can be calculated as

$$S_{11s} = \frac{\Gamma_{12}(1 - e^{-j2\Psi})}{1 + \Gamma_{12}^2 e^{-j2\Psi}}. \tag{2.6}$$

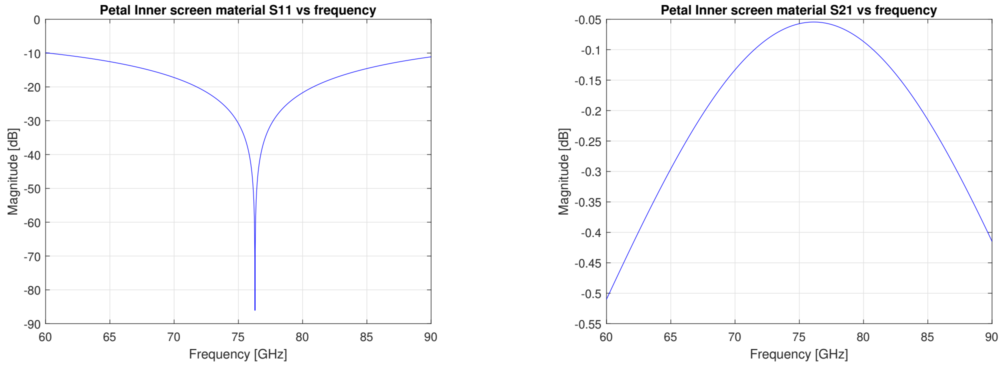

(a) Petal inner screen material S_{11}

(b) Petal inner screen material S_{21}

Fig. 2.4 Petal Inner Screen material characteristics (1.17 mm)

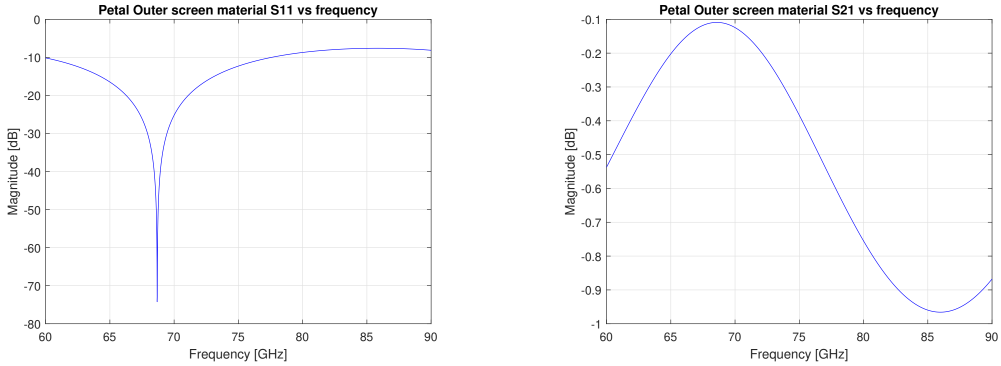

(a) Petal Outer screen material S_{11}

(b) Petal Outer screen material S_{21}

Fig. 2.5 Petal Outer screen material characteristics (2.8 mm)

The reflection and transmission coefficients for each MUT, and for the thicknesses reportd in Table 2.1 are shown in Fig. 2.4, Fig. 2.5, and Fig. 2.6.

Considering the band from 77 to 81 GHz it can be observed that for all three materials, the insertion loss is relatively low (<1 dB). As regards the reflection coefficient, for the outer lens, it is less than -30 dB in the band of interest. The value is sufficiently good and the material does not need further optimization. The reflection coefficient of the inner screen is optimal around 76.5 GHz but it is still good at 81 GHz ($S_{11} < -20$ dB). For the outer screen, the reflections are quite high ($S_{11} > -10$ dB in the band of interest), and thickness adjustments are required to move the minimum value in the center of the frequency of interest.

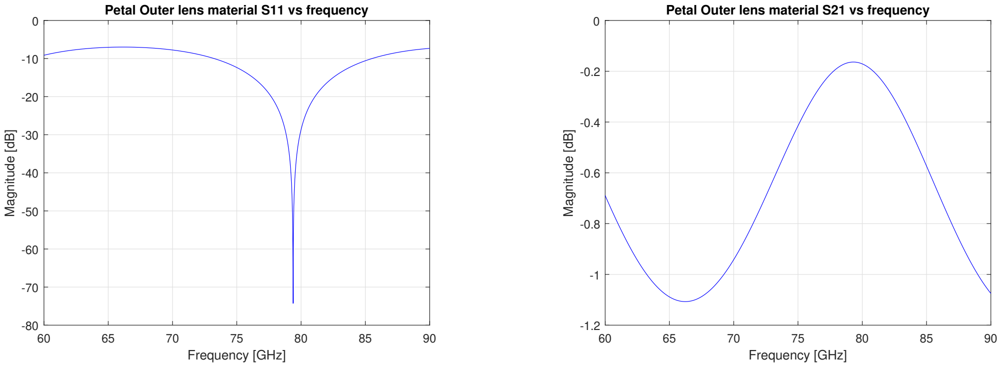

(a) Outer lens material S11

(b) Outer lens material S21

Fig. 2.6 Outer lens material characteristics (3.5 mm)

By propagating the reflection effect from the outmost to the innermost layer the S_{11Tot} and S_{21Tot} of the full petal structure can be derived. While attenuation losses are for sure to be considered but limited, the most impacting factor in such a structure is the S_{11Tot} which needs to be as small as possible to avoid ghost target appearances and Signal to Noise Ratio (SNR) degradation.

Since changing the petal materials was not possible, the thickness of the petal outer layers was optimized with the goal of mitigating the reflection coefficient S_{11Tot} in a band of 500 MHz from 77-77.5 GHz. The optimal value was found by calculating the reflection coefficient for multiple frequencies, varying the outer layer thickness, and choosing the value that gave better performances over the bandwidth. The optimal thickness for the petal outer screen is 2.3 mm. Fig. 2.7 shows the S_{11Tot} of the multi-layer structure in front of the radar for the 60-90 GHz frequency band with two different thicknesses of the petal outer screen material (original and optimized). Drastic improvements of S_{11Tot} were obtained. In the original case the S_{11Tot} was worse than -10.5 dB in the whole 77-81 GHz bandwidth. The structure with the optimized thickness has a reflection coefficient lower than -18 dB in the 77-77.5 GHz frequency band. Since the usual bandwidth adopted for MRR is lower than 500 MHz the obtained results can give a noticeable improvement in the radar performances with the correct selection of radar transmitting frequency and antenna bandwidth. From the $tan\delta$ measurements and layer thicknesses, the one-way attenuation losses of the structure at 77 GHz have been estimated to be 0.6 dB which is a comparable value with respect to the ones of typical bumpers [20]

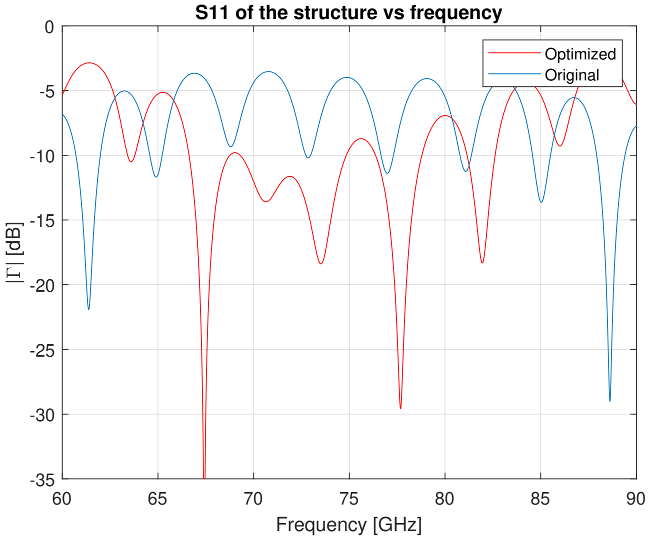

Fig. 2.7 Reflection coefficient of the lamp structure in front of the radar vs frequency with original and optimized thickness of the petal outer screen

2.2 Proposed Architectural Solution

As mentioned in Chapter 2.1 the radar had to fit behind a tiny petal of dimension 60 mm x 29 mm. Given the limited dimensions the proposed solution was based on the realization of two boards: the radar power supply board which generates the necessary low-noise power rails and manages the communication of the radar with the outside world, and the radar board which hosts an integrated radar chip, the transmitting and receiving antennas, the voltage supply filters, and the other required components to handle communication. The radar power supply board, needed to fit into the lamp orthogonally connected to the radar board, and mechanical constraints were carefully taken into account for its components placement.

Thanks to the advancements in integrated chip design, today fully integrated automotive radars on chip are available on the market. This kind of solution allows a reduction of space occupation on the board and includes the capability of internal real-time processing of the captured data. For this reason, the proposed radar board hosts the AWR1843 [24] chip-set manufactured by Texas Instruments. It belongs to the AWR1x family of single-chip mmWave radar sensors for ADAS applications. This device is built with TI's low-power 45 nm RF CMOS technology and operates in the entire 76–81 GHz automotive frequency band: it can sweep a frequency range up to 1 GHz in the 76-77 GHz band for long range applications or a frequency range up to 4 GHz in the 77-81 GHz band for high resolution/short range applications. To

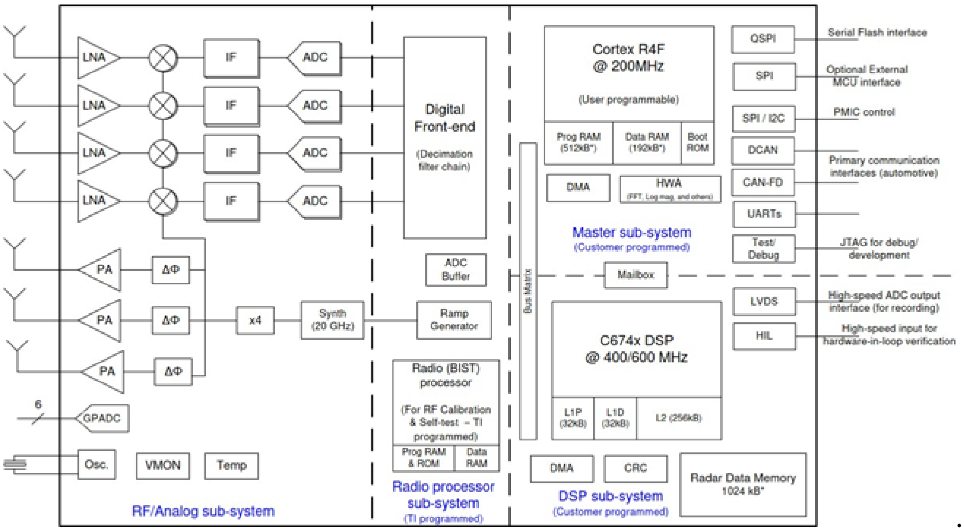

Fig. 2.8 AWR1843 chipset block scheme

generate an FMCW signal at the desired carrier frequency, the AWR1843 integrates an internal 40 MHz crystal oscillator followed by a clean-up Phased Locked Loop (PLL) and a Radio Frequency (RF) synthesizer circuit. From the 20 GHz synthesized signal, a 4X multiplier generates the proper signals for the TXs and the RXs. An RF noise figure of 15 dB and phase noise at 1 MHz offset in the 77-81 GHz band of -93 dBc/Hz is specified by the manufacturer. Operations with 3 TXs and 4 RXs with In-phase and Quadrature (I/Q) channels are fully supported. The chip integrates an R4F ARM processor for automotive interfacing and a high-performance C674x Digital Signal Processor (DSP) for radar signal processing.

In Fig. 2.8 the functional block diagram of radar on chip is presented. On the left side, the 3 TX and 4 RX RF chains are shown. The upscaled signal from the synthesizer is sent both to the power amplifiers (12 dBm output per channel maximum) for transmission and to the mixer to be mixed with the received signal. All 3 TX channels have independent, programmable phase and amplitude control. The RX chain after the mixer presents two programmable high-pass filters (to reduce saturation effects due to the strong target's presence in proximity of the radar) and has a maximum IF bandwidth of 10 MHz. Two ADC buffers are also present to allow the processing of samples received in one buffer while the other one is being filled. On the right side, there are the R4F ARM processor and the DSP with their dedicated memories. In particular, the DSP has 3 memories of different sizes (L1, L2, L3) and access speeds. The fast access to the L1 memory is necessary to compute and store the range FFTs in real-time (in a time shorter than the chirp duration). The L2 memory gives the user a compromise between fast access and memory size to store buffers that are accessed multiple times but are not used in the part of the processing that requires fast computations. The L3 memory is a slower and bigger memory that is shared between DSP and ARM allowing an easy exchange of data between the two cores.

The AWR1843 offers different solutions to interface with external devices such as Quad Serial Peripheral Interface (QSPI), Serial Peripheral Interface (SPI), Inter-Integrated Circuit (I^2C), Controlled Area Network (CAN), Universal Asynchronous Receiver Transmitter (UART), Joint Test Action Group (JTAG), and Low Voltage Differential Signalling (LVDS).

The radar power supply board and the radar board work as an integrated solution as shown in the block diagram of Fig. 2.9. The radar outputs are transmitted via Serial Peripheral Interface (SPI) through the radar power supply board to a KSZ8851SNL [25] evaluation board (SPI-to-Ethernet converter) and then to a Laptop PC to be displayed on a user interface and to be stored for further post-processing. Commands are transmitted from the Laptop PC through Ethernet to the KSZ8851SNL and then, via SPI to the radar.

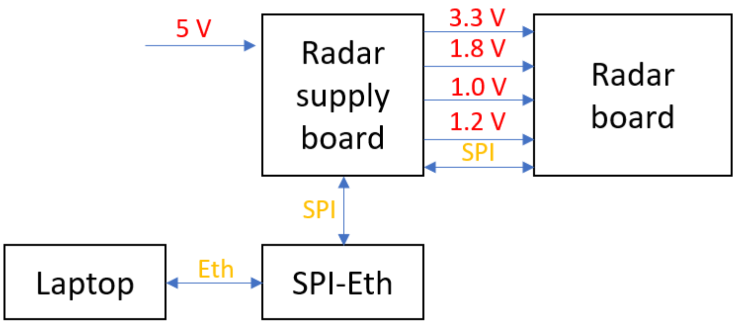

Fig. 2.9 Block Diagram of the two boards solution with SPI-Ethernet communication

As a parallel solution to the radar prototype with SPI for the tests, a solution of the radar in which the radar power board is fully integrated into the original lamp motherboard and the radar data are transmitted directly on the CAN bus was realized. The AWR1843 chip supports both the CAN and CAN-FD protocols, however, they present lower throughput with respect to the SPI (1 Mb/s and 8 Mb/s respectively vs the 40 Mb/s of the SPI). For this reason, the output of this solution is only a list of tracked targets with fundamental information (position and velocity). Since CAN communication requires only two cables, the SPI routes were exploited and the radar power board layout did not require any modification besides the addition of a CAN transceiver to manage the Radar CAN node. The CAN transceiver is connected both to a micro-controller, already present on the lamp motherboard, which manages the lighting control unit of the lamp, and to a vehicle connector from which the signal can be converted to USB and visualized on a Laptop PC as shown in Fig. 2.10.

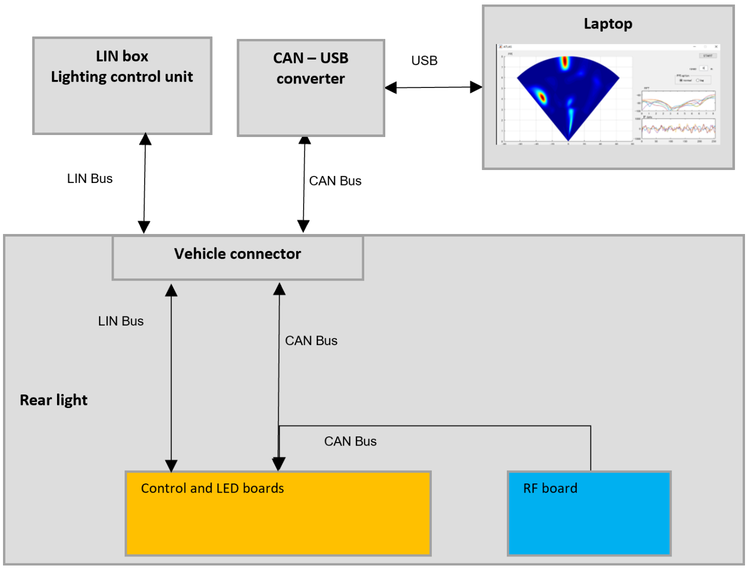

Fig. 2.10 Block Diagram of the integrated CAN solution

2.3 First Prototype

2.3.1 Radar Power Board

The input power rails required by the AWR1843 chip are generated from a 5V power supply. A MAX1502 radar [26] DC-DC dual buck switching regulator generates the 3.3 V voltage, used by the SPI communication interfaces, and the 1.8 V voltage, used by the RF VCO, internal clock module, and baseband circuitry. The switching frequency is set to 2 MHz. Due to the very high sensitivity of the radar sensor toward noise on the supply voltage, it was necessary to strongly filter the harmonics generated by the DC-DC converter.

A 1.24 V rail is required to supply the embedded ARM processor and DSP while 1.0 V is required to supply the RF chain. Both voltages are obtained with

TPS7A5301 [27] low noise, low drop-out regulators starting from the 1.8 V and the 1.24 V repetitively. Fig. 2.11 reports a block diagram for the power supply board.

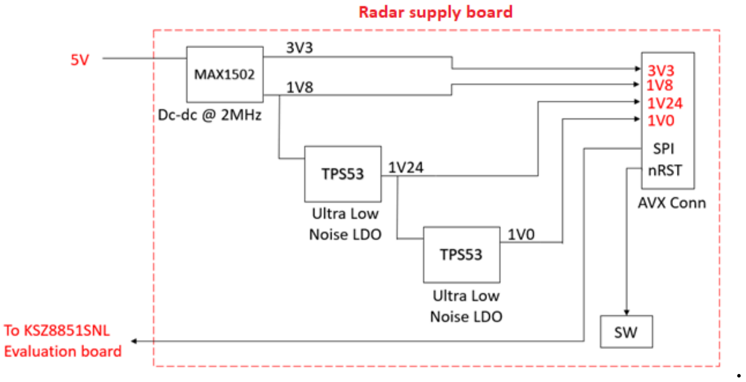

Fig. 2.11 Radar power supply board block diagram

The SPI interface lanes from the radar board are rerouted by the radar power board to the SPI to Ethernet controller KSZ8851SNL chip on an external evaluation board. This connection allows high bit rate data transfer up to 25 Mbit/s and is essential to transmit verbose data during the radar testing and validation phases. All the components installed on the radar power supply board are automotive compliant (AEC-Qxx qualified [28]). The radar power board is orthogonally inserted in an edge connector mounted on the radar board.

The radar power board (shown in Fig. 2.12) fits into the lamp housing and is stabilized with mechanical holders to minimize vibrations

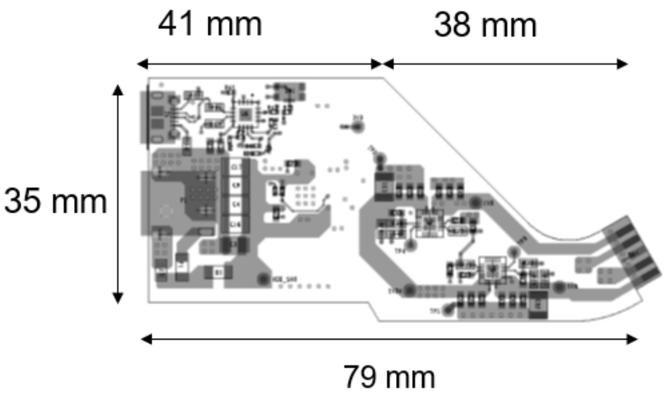

Fig. 2.12 Radar Power board final form (Top layer)

The radar power board is a standard FR-4, 4 layers stack-up. The top and bottom cores are Panasonic R-1551 2x7628 0.412 mm thick while the central prepreg layer is a Panasonic R-1566 7628 0.6 mm core. Fig. 2.13 reports the stack-up details as well as the adopted via technology (through vias only).

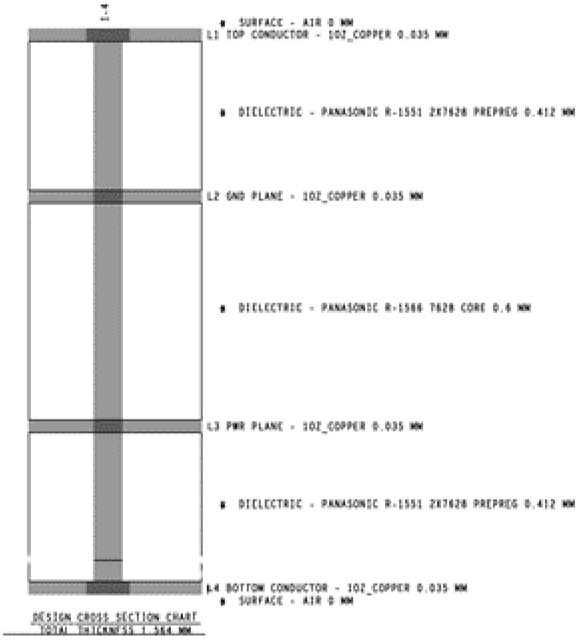

Fig. 2.13 Radar Power board stack-up details

2.3.2 Radar Board

The radar board has the goal of generating and receiving the FMCW radar signal, processing the received data, and sending the outputs through SPI or CAN. As previously mentioned, two solutions were realized:

- A solution for testing and validation of the radar, which requires a high throughput to analyze the complete radar response, transmits data via SPI protocol.
- A fully integrated solution that is connected directly to the rear lamp motherboard and transmits data via CAN protocol.

A block diagram of the radar board is reported in Fig. 2.14: the realized PCB hosts the AWR1843 chip, a 40 MHz crystal oscillator, a QSPI memory for booting [29], filters, a JTAG connector required for debug purposes, a connector for power supply and SPI/CAN communications, and the antennas.

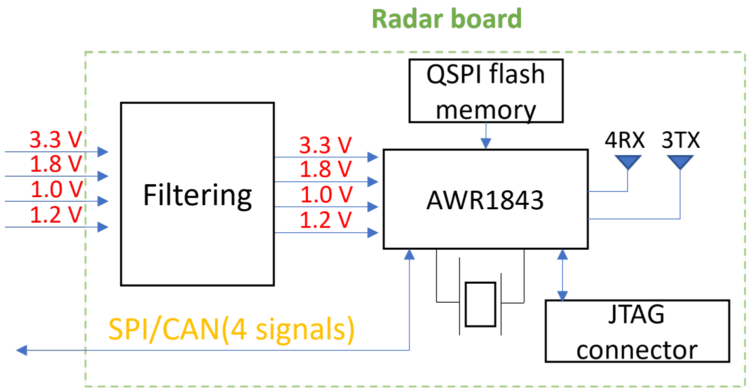

Fig. 2.14 Radar board block diagram

Thanks to the pin-to-pin compatibility of the SPI/CAN peripherals, it was possible to maintain the same board architecture for both solutions. With a minimal change only in the radar board connector, the radar board can be directly plugged into the rear lamp motherboard integrated with the radar power supply board components, and it can communicate on the car CAN bus. The difference between the two radar boards is only in how the boards are connected to the radar power board: in the SPI solution, the radar power board is connected to the back of the radar board while in the CAN solution, the radar is plugged into the lamp motherboards.

Since the AWR1843 does not transmit continuous waves but fast chirps, the current exhibits an impulsive behavior. The connector between the two boards was chosen for its high current rating per pin (2.5 A) and it was selected as the 00-9159-650 from AVX. The connector is installed in such a way that the radar power board can be inserted orthogonally into the radar board. Pictures of the realized prototypes for the two solutions are reported in Fig. 2.15. Fig. 2.15a shows the SPI solution outside the rear lamp with the two manufactured boards connected together and the SPI to Ethernet conversion board dedicated to data communication to a Laptop PC. Fig. 2.15b shows the CAN solution with the radar board inserted into the petal and plugged into the rear lamp motherboard integrated with power supply board components.

Radars in general have stringent requirements regarding the power supply noise rejection since this noise can heavily affect the radar performances. For this reason, a filter was designed to reduce the noise level on all the power supply rails of the radar board. The band of interest for the radar spectrum goes from DC to the maximum IF frequency. The maximum IF frequency of AWR1843 is 10 MHz, therefore the

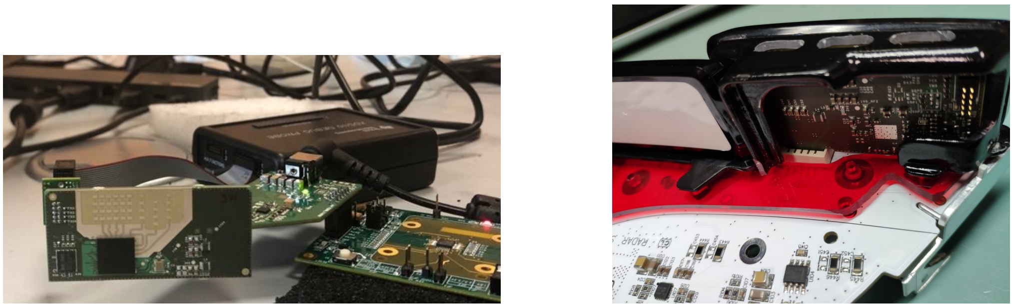

(a) SPI solution

(b) CAN solution

Fig. 2.15 Realized prototypes for the two solutions

noise suppression must be as good as possible in the 0-10 MHz band. An LC filter was implemented as shown in the schematic of Fig. 2.16a. The filter has two configurations: one with capacitors and a series inductor and one with a ferrite bead instead of the inductor. The power supply rails used by the RF front end mount the ferrite bead that allows deeper band filtering. The overall effect is an attenuation of at least -55 dB from 100 kHz to 10 MHz which is acceptable for our task. Further filtering for the lower frequencies is also performed internally by the AWR1843 receiver chain with two tunable frequency filters.

The transmitting and receiving antennas are both vertically polarized microstrip patch arrays of 4 elements printed on a ROGER4835 [30] substrate (ε_r=3.48) with a 10 dB gain at 77 GHz, ±28° horizontal 3dB-beamwidth and ±14° vertical 3dB-beamwidth. Unfortunately, the limited space did not allow for more vertical array elements to further increase the gain. All the antennas are positioned behind the petal and with a clear field of view not limited by the lamp structure. The antennas are disposed on the radar board to obtain a uniform MIMO virtual array [11] with one 8-element horizontal row and a second 4-element horizontal row displaced vertically as in the scheme of Fig. 2.17a.

This configuration enables both azimuth and elevation direction of arrival estimation. The virtual elements are spaced of a distance $d = \frac{\lambda}{2}$ horizontally and vertically in order to maximize the field of view. In Fig. 2.17b the antennas placed on the top layer of the realized radar board are shown. Two passive elements have been added on the side of RX1 and RX4 to maintain symmetry and avoid differences in the response in the receiving antennas' behavior.

The 50 Ω matching condition between the antenna and the radar chip needs to be satisfied to maximize the power delivery from one to the other. The optimal solution

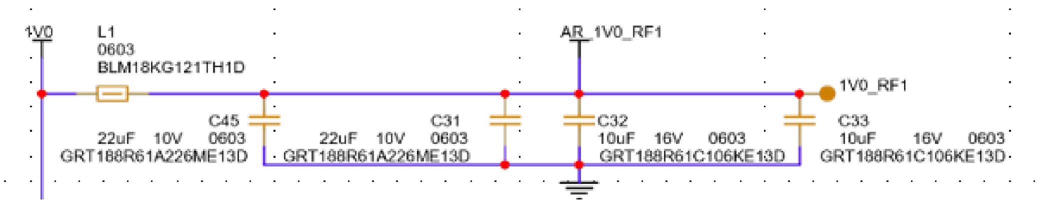

(a) LC filter with ferrite bead schematic

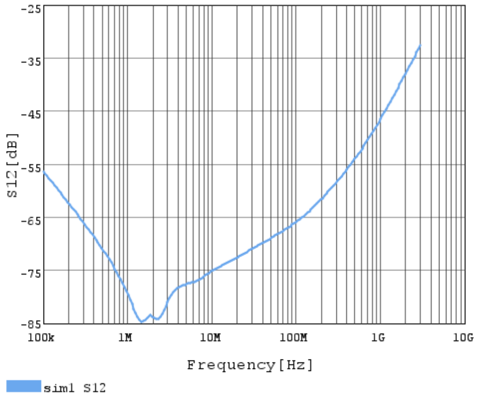

(b) LC filter transmission coefficient

Fig. 2.16 LC filter design

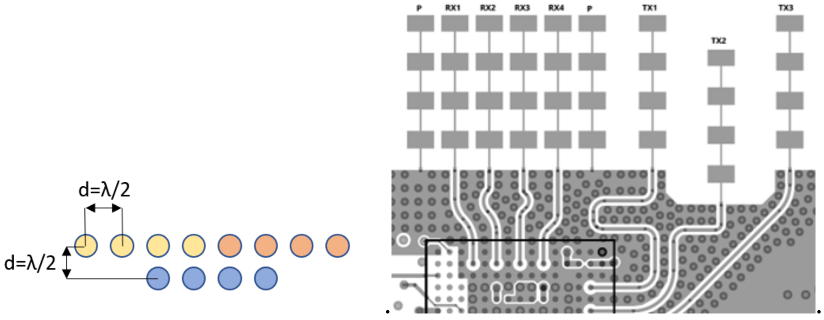

(a) MIMO virtual array (b) Radar board antenna view

Fig. 2.17 Antenna Positioning

to connect the two is to design the feeding line as a Ground Coplanar Waveguide (GCPW). The advantage of the GCPW is that the ground pours on the side of the signal line allowing the placing of ground via arrays around the signal trace reducing the radiated loss along the line and protecting it from interfering signals. The design parameters used to implement a 50 Ω GCPW are reported in Fig. 2.18.

The 6-layer stack-up adopted for the radar PCB is reported in Fig. 2.19. The top and ground metal layers are printed on a Rogers RO4835 core with a thickness of

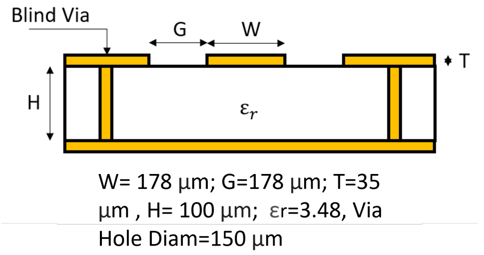

Fig. 2.18 GCPW design parameters

0.1 mm while the remaining conducting layers are intervalled with FR4 cores and prepreg. To shield the antenna feeding lines it was necessary to adopt blind vias; normal through-hole vias are not suitable for this operation due to their parasitic parameters.

Fig. 2.19 Radar PCB stack-up

Since the desired detection range goal for a vehicle with a typical Radar Cross Section (RCS) $\sigma_{dB} = 10\ dBm^2$ is $R_{max} = 75$ m, we can calculate the expected SNR for this type of target to verify if the antenna gain is enough. For this purpose, some considerations need to be made:

- The radar equivalent temperature is assumed to be at the maximum temperature limit of the chip $T = 398$ K.
- Typical values of chirp duration T_c for automotive radars can go from 10 μs to 100 μs depending on the application. The shorter the T_c, the worse the SNR is for the same number of transmitted chirps. The chirp duration includes some idle time and end time during which the TX channels are not active. For the evaluation of the SNR only the active part of the chirp (the part that is actually

sampled) T_{ca} has to be considered. It is assumed $T_{ca} = 36.6\mu$s which is the value adopted for the realized radar (more details on the radar parameters will be given in Chapter 3).

- The transmitted power per TX channel specified on the data sheet of the AWR1843 is $P_T = 12$ dBm. However, it should be supposed that the actual output power can be a bit lower than this value due to manufacturing imperfections of both the chip and the board. A $P_t = 11$ dBm lowered by 1 dB with respect to the nominal value, is considered as a reasonable enough assumption.
- The Noise Figure (NF) of the receiver channels of the AWR1843 is 15 dB in the 77-81 GHz bandwidth.
- The two-way losses due to propagation in the lamp material are assumed to be $L_{dB} = 4$ dB which is an overestimation given the result of measurements and simulations of the optimized petal presented in Chapter 1. This is a conservative assumption to be on the safe side of the design.
- The number of chirps transmitted by each of the three TX antennas and integrated per each frame is $N_c = 64$.
- The compression gain for FMCW radar is given by the time-bandwidth product BT_{ca}, with $B = 457$ MHz.
- The targets should also be detected when they are not at the boresight (where the gain is not at this peak). The goal is to detect a target at 30° at the maximum range of 75 m. The antenna gain at 30°, considered for this calculation, for both TX (G_{TX}) and RX (G_{RX}), is 6.5 dB.
- The radar processing can detect targets if the SNR of their peak is at least 10 dB. This is a conservative assumption for the design; targets can be detected, in practice, even with worse SNR.

From radar FMCW theory after the reception, the SNR of the scattered signal from a $\sigma = 10m^2$ at distance R_{max} is

$$SNR = \frac{P_T G_{RX} G_{TX} \sigma N_{TX} N_c B T_c}{(4\pi)^3 R^4 kTBL} = 20.7 = 13.2\ dB \tag{2.7}$$

where k is the Boltzmann constant. This result provides a good margin to successfully detect $\sigma_{dB} = 10\ dBm^2$ targets at the maximum range. Furthermore, if it is required, some improvement on the SNR can still be obtained by increasing the number of integrated chirps (at the cost of memory occupation and processing time) or their duration (at the cost of lowering maximum unambiguous velocity).

The top and bottom layers of the realized radar board are reported in Fig. 2.20. Fig. 2.20a shows the top layer of the radar board with a uniform MIMO antenna scheme. Fig. 2.20b shows the bottom layer of the radar board for the SPI solution with the connector in the center of the PCB, and for the CAN solution with the edge connector on the bottom side of the PCB.

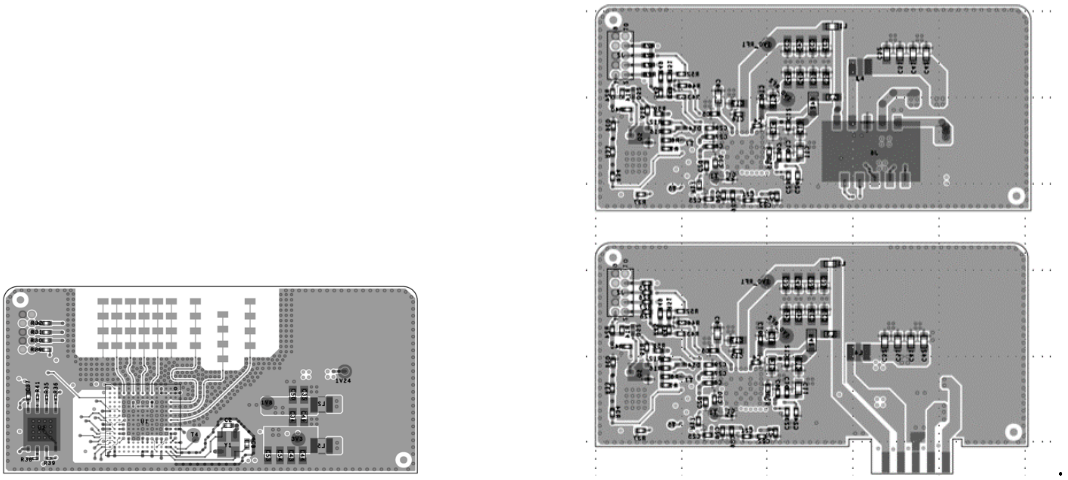

(a) Top Layer of the first prototype

(b) Bottom layer of first prototype (SPI/CAN)

Fig. 2.20 Top and bottom layers of the radar board for the first prototype

The first prototype reached the goal of demonstrating the radar capability to detect and track targets at the desired range. During the tests of the first prototype, whose results have been presented by the author in [31], and summarized in Chapter 4, the following considerations were raised:

- Angular resolution can be a bottleneck in detecting multiple close targets in real traffic scenarios. The angular resolution of the radar should be improved as much as possible.
- The DC-DC switching frequency falls into the radar spectrum and the filtering is not enough to suppress it. Either an improved filtering or a power supply chain with a lower impact on the range frequency of interest of the radar should be adopted.

- The connector between the radar power board and the radar board can have some degradation due to friction after short usage. The degraded connector does not withstand the radar's impulsive power supply current, increasing substantially the SNR of the detection and causing the radar to not operate properly. A new type of connector is mandatory.

- The radar temperature tests showed that in the worst-case scenario (Ambient Temperature: 70 °C) the chip's internal temperature can increase above the maximum temperature rating. Some adjustments to component placement, housing, and board geometry are required to stay within the chip maximum ratings.

2.4 Second Prototype

The goal for the second prototype was to perform the validation tests with the radar installed on the car. The prototype was realized taking into account the considerations raised after the tests performed with the first prototype. Both the radar power board and the radar board were modified to improve performance and solve all the mentioned issues.

2.4.1 Radar Power Board

For the radar power board, the main problem was the DC-DC converter. The MAX15021 has a tunable switching frequency which can go from 0.5 to 4 MHZ. Whatever the chosen switching frequency is, it always falls in the band of interest for the radar detection ($IF_{max} = 10MHz$). From the test performed both by looking at the spectrum of the radar power board supply rails on a Spectrum Analyzer and by observing the radar range-Doppler matrix output it was clear that the noise introduced by the DC-DC converter was too high and not filtered enough. Therefore, it was chosen to modify the power supply chain by choosing a DC-DC converter with a feature called spread spectrum: the purpose of the spread spectrum is to eliminate peak emissions at specific frequencies by spreading emissions across a wider range of frequencies. The chip was selected among the chip family LM636X5-Q1 [32] from Texas Instruments. They are synchronous, step-down DC/DC converters designed for automotive applications. The various chips in the family differ in the maximum load current they can support with an input from 3 to 36 V. This feature is useful to power up the radar directly from the 12 V car battery. Differently from the MAX15021, the LM636X5-Q1 family does not allow double rails conversions to both 3.3 V and 1.8 V and for this reason, the subsequent power supply stages were modified. Three different low-noise LDOs were cascaded (TPS7A5301) one after the other for the conversions: 3.3 V-1.8 V, 1.8 V-1.24 V, and 1.24 V-1.0 V. From the analysis of the current required from the radar, it resulted that when the radar is transmitting, the current request on the 3.3 V rail is higher than 1.5 A. The selected chip among the LM636X5-Q1 family was the LM63635 with 3.5 A of maximum load current. The final block scheme of the power supply chain with the DC-DC converter and the three LDOs is reported in Fig. 2.21

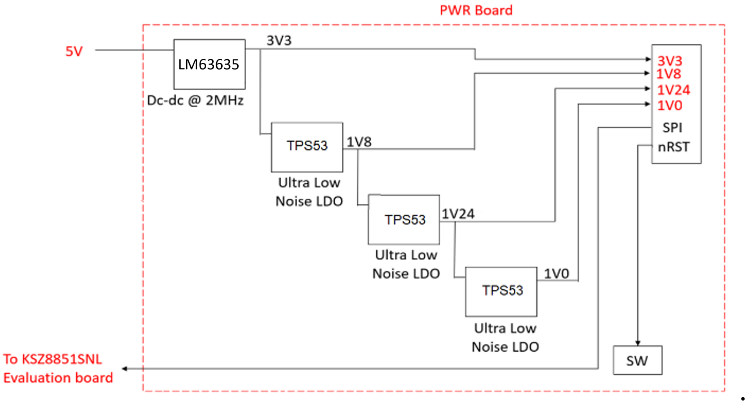

Fig. 2.21 Second Radar power supply board block diagram

The second issue was related to the degradation of the connector which was changed to a more stable solution with an M-F pin header. The selected connector is the TSW-105-05-G-D male connector which can also sustain high peak current and is more suited for radar applications. From the test performed on this second prototype no degradation in performance was noticed due to friction.

2.4.2 Radar Board

For the radar board, different upgrades were implemented to solve the mentioned issues:

- Component positioning was modified to lower the temperature that the radar can reach when operating in critical conditions. Since the AWR1843 chip is the principal source of heat, it was moved toward the center of the radar board and some more space was created in the lower part to help heat distribution in all directions.

- The possibility of adding a feed-through capacitor in series to the already implemented LC power supply filters, was considered. The considered component was the NFM31PC276B0J3L, a 27 μF, 3 pins feed-trough capacitor. The expected filter transmission coefficient is reported in Fig. 2.22 with attenuation greater than -80 dB over the whole DC-10 MHz bandwidth.

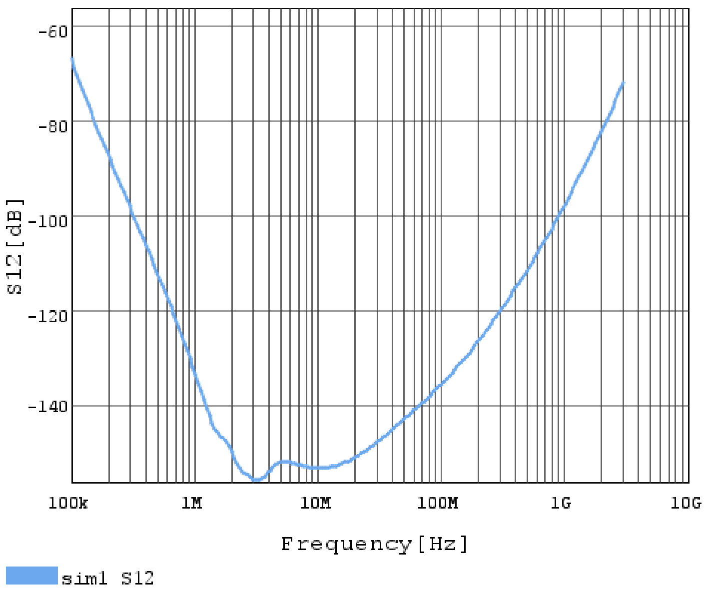

Fig. 2.22 Expected filter with feed-through capacitor transmission coefficient

- As for the second version of the radar power board, also for the radar board the connector was changed. In this case, the selected component was the corresponding header female connector of the same family mounted on the radar power board. To still support the two solutions (with SPI and CAN) the board has been designed in such a way that the same connector can be utilized for both as shown in Fig. 2.23b. The connector with the pins directed toward the bottom is the one which is installed for the motherboard of the rear lamp, while the connector of the radar power board is inserted orthogonally to the radar board.

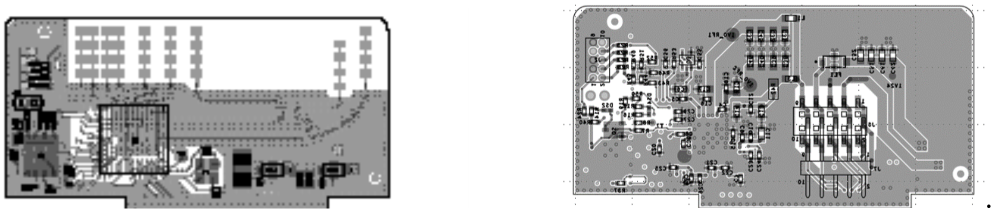

(a) Top Layer of the second prototype

(b) Bottom layer of the second prototype

Fig. 2.23 Top and bottom layers of the radar board for the second prototype

- A new antenna scheme described in following Chapter 2.4.3 was implemented to improve the angular resolution of the radar. The top layer of the realized radar board with the new antenna scheme is reported in 2.23a.

2.4.3 Minimum Redundancy MIMO

The angular resolution is a fundamental parameter for an automotive radar since the ability to resolve targets in the angular dimension is very important in a road environment where multiple vehicles, persons, and objects can be detected even in a few-degree interval at the same range. The most common way to improve the angular resolution is to increase the number of virtual antennas with more uniformly spaced TXs and RXs. However, this comes at the cost of space occupation, increased number of radar chips power consumption, and heavier processing.

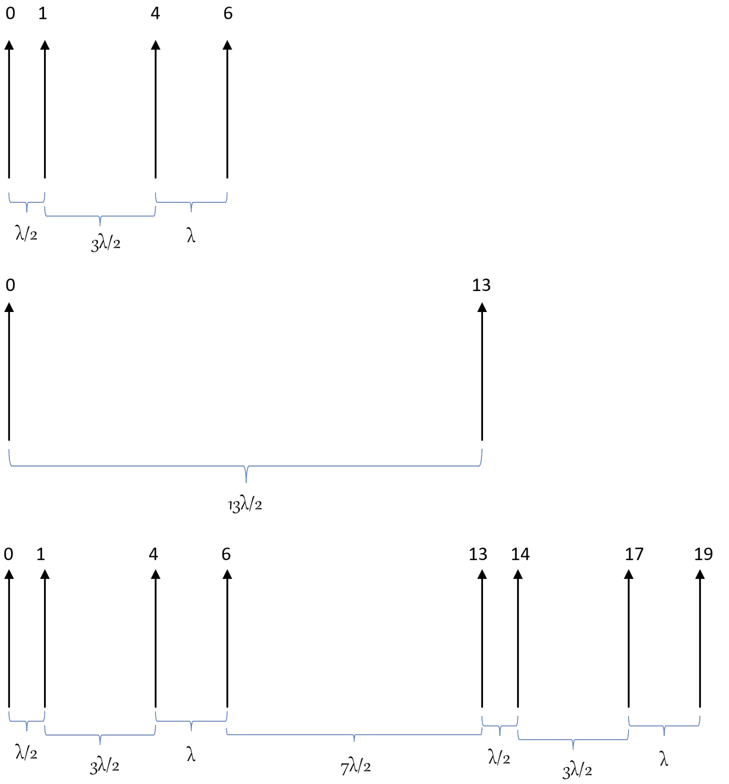

Fig. 2.24 MR MIMO Virtual Array

The Minimum Redundancy MIMO (MR MIMO) consists of placing the antenna in a non-uniform way. The MR MIMO described in [33] is an extension of the minimum redundancy linear array concept first described in [34]. The idea is that the number of array elements should be minimized as long as the spacing between TX-RX pairs of the array elements includes all the integers between 1 and L (desired normalized aperture).

For the MIMO radar case, the spacing between pairs can be expressed as

$$\{u_{Tm} - u_{Rn} - u'_{Tm} + u'_{Rn} \mid m = 0, 1, \ldots, M,\ n = 0, 1, \ldots, N\} \tag{2.8}$$

where u_T, m and $u_{R,n}$ are the normalized antenna positions, u and u' represent two different pairs, and M and N are the number of TX and RX elements. The MR MIMO configuration can be derived by solving the optimization problem

$$\begin{aligned} \min_{\{u_{Tm}\},\{u_{Rn}\}} \quad & N + M \\ \text{subject to} \quad & |\{u_{Tm}\}| = M, \quad |\{u_{Rn}\}| = N \\ & \{u_{Tm} - u_{Rn} - u'_{Tm} + u'_{Rn}\} \supset \{1, 2, \ldots, L\}. \end{aligned}$$

For relatively small L the problem can be solved by means of an exhaustive search algorithm.

The problem can be applied to the case of the radar board horizontal antennas with 2 TX, and 4 RX antenna elements. The maximum aperture that can be achieved is L=19, while with a uniform aperture, the aperture is L=7. The maximum aperture achievable with a complete array was verified through an exhaustive search of all the possible combinations of antenna relative positions, with L varying in the range between 5 and 40. The resulting normalized antenna positions are $\{u_{Tm}\} = \{0, 13\}$ and $\{u_{Rn}\} = 0, 1, 4, 6$. This result is obtained with the same number of TXs and RXs of the uniform array at the only cost of space on the radar board.

The MR MIMO configuration to improve azimuth resolution is reported in Fig. 2.24. The resulting virtual array presents all the phase differences required to obtain a complete uniform array from element 0 to element 19.

Chapter 3

Firmware Design

3.1 Frame structure and Radar Parameters

The frame structure used for the transmitted radar signal is composed of two Sub-Frames (SF) as shown in Fig. 3.1. In the first SF, the three TXs use the Time Division Multiplexing (TDM) MIMO scheme for azimuth and elevation direction of arrival. All the TXs in this frame use linear frequency modulated waveform with the same duration and slope and whose parameters are reported in Table 3.1.

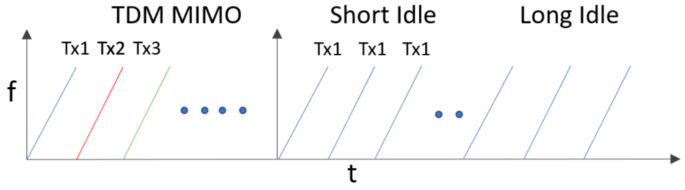

Fig. 3.1 Frame structure

Table 3.1 Key Radar Parameters for the TDM MIMO frame

Symbol	Description	Value
BW	Bandwidth	457 MHz
Tc	Chirp Duration	50.57 μs
T_{sa}	Sampling Duration	36.57 μs
S	Slope	12.5 MHz/s
N	Number of Chirps per TX	64
Fs	Sampling Frequency	7 MHz

The second frame has two bursts of linear frequency modulated waveforms which are sent with all TXs transmitting simultaneously and whose parameters are reported in Table 3.2. They have different idle times in order to have different Pulse Repetition Frequency (PRF) and consequently different maximum unambiguous velocities.

Table 3.2 Key Radar Parameters for the second frame

Symbol	Description	Value
BW	Bandwidth	457 MHz
Tc1	Chirp Duration Fast	50.57 μs
Tc2	Chirp Duration Slow	55.57 μs
T_{sa_1}	Sampling Duration Fast	36.57 μs
T_{sa_2}	Sampling Duration Slow	36.57 μs
S	Slope	12.5 MHz/s
N	Number of Chirps per TX	64
Fs	Sampling Frequency	7 MHz

In this way, it is possible to estimate velocity larger than the maximum unambiguous one as explained in detail in Chapter 3.7. Finally, the radar performances derived from the frame structure design are reported in Table 3.3: the range resolution and maximum range are the same for the two SFs while, since during the second SF all TXs are transmitting simultaneously, the natural maximum unambiguous velocity is higher for the second SF.

Table 3.3 Performance Parameters of the radar

Symbol	Description	Value
δR	Range Resolution	0.3 m
R_{max}	Maximum Unambiguous Range	75.45 m
δv_1	Velocity Resolution of 1^{st} SF	0.2 m/s
δv_2	Velocity Resolution of 2^{nd} SF	0.6 m/s
v_{max_1}	Maximum unambiguous velocity of 1^{st} SF	± 23.1 km/s
v_{max_2}	Maximum unambiguous velocity 2^{nd} SF	± 69.3 km/s

3.2 Radar Firmware Structure

The firmware for this application was fully developed on the AWR1843 chipset hosted by the radar board. Even if the chip supports a real-time operative system with multitasking operations, the firmware was implemented without an operative system to enable better control of all functions to reduce firmware memory requirements and to increase efficiency. The complete radar processing was implemented on the integrated C674x DSP while a tracking algorithm and the data transfer interface were implemented on the integrated R4F ARM processor. The DSP is directly connected to the BIST Subsystem (BSS) which controls the RF front-end. The DSP sends commands to the BIST by calling specific Application Program interfaces (API) provided by Texas Instruments.

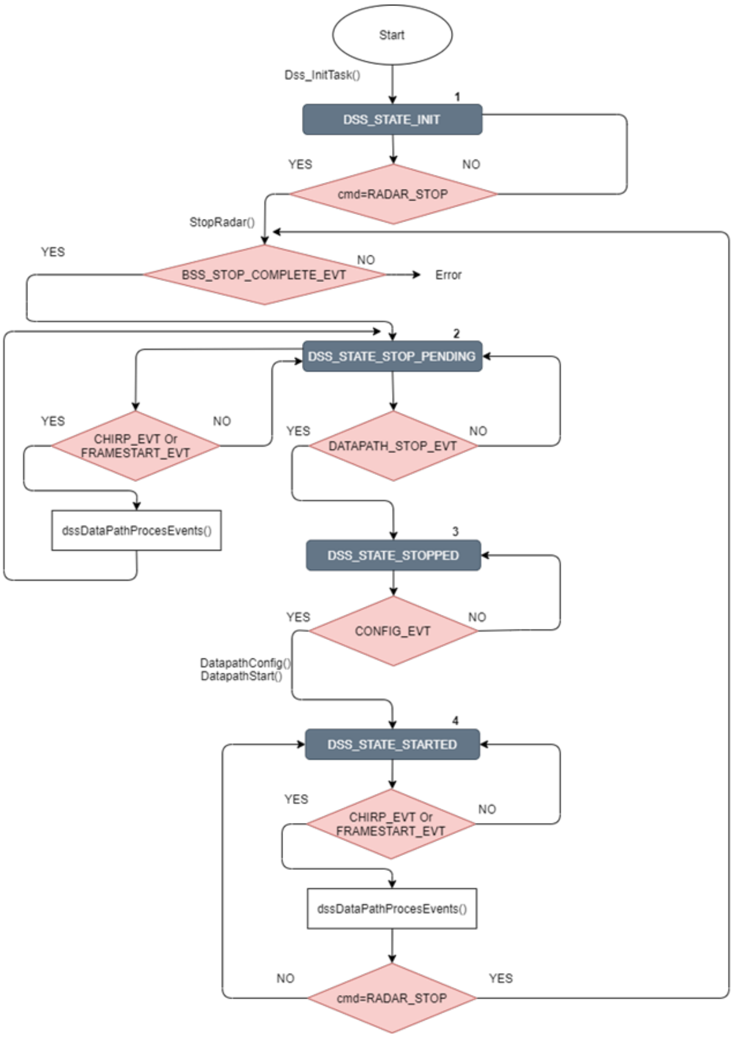

Fig. 3.2 DSP state Diagram

The R4 ARM also acts as the Master Subsystem (MSS) for the application. It issues commands such as start and stop of operations and sends the parameters for radar initialization to the DSP through the internal mailbox of AWR1843. The DSP

Subsystem (DSS) after initializing the BSS with the received parameters starts to continuously check the mailboxes to see if any message has been received from the MSS and to check if any interrupt event has been raised. The possible interrupt events are:

1. **CONFIG_EVT**: This event is posted when DSS receives a configuration message from MSS. Datapath is initialized and after a RADAR_START command is received radar operations are started.
2. **FRAMESTART_EVT**: This event is posted by BIST firmware. It indicates the beginning of the radar frame.
3. **CHIRP_EVT**: This event is posted by BIST firmware. It indicates that one of the ADC buffers is filled with ADC samples.
4. **BSS_STOP_COMPLETE_EVT**: This event is posted by DSS after it has received a RADAR_STOP command. It stops the sensor.
5. **DATAPATH_STOP_EVT**: This event is posted by DSS when BIST stop is completed. It moves DSS into the stop state and communicates it to the MSS

The DSS works as a finite state machine and its possible states are:

1. **DSS_STATE_INIT**: starting idle state.
2. **DSS_STATE_STOP_PENDING**: preparing for stop state.
3. **DSS_STATE_STOPPED**: stop state.
4. **DSS_STATE_STARTED**: operating state.

Fig. 3.2 reports the state diagram of the DSS. At start-up, DSS is initialized and is moved to the idle state DSS_STATE_INIT.

When in DSS_STATE_INIT state:

- If **RADAR_STOP** command is received, BSS is stopped with BSS_STOP_COMPLETE_EVT and DSS is moved to DSS_STATE_STOP_PENDING.

When in DSS_STATE_STOP_PENDING state:

- If **CHIRP_EVT** or **FRAMESTART_EVT** are detected, they are served, and the state is maintained.

- If **DATAPATH_STOP_EVT** is detected, DSS is moved in DSS_STATE_STOPPED.

When in DSS_STATE_STOPPED state:

- If **CONFIG_EVT** is detected, DSS is configured, started, and moved in DSS_STATE_STARTED.

When DSS_STATE_STARTED state:

- If **CHIRP_EVT** or **FRAMESTART_EVT** are detected, they are served, and the state is maintained.
- If **RADAR_STOP** command is received, BSS is stopped and DSS is moved to DSS_STATE_STOP_PENDING.

3.3 Radar Processing

As mentioned in Chapter 1.3 the radar processing requires the computation of multiple FFTs on the received signal to extract range, velocity, and AoA information of the targets. A typical high level radar processing of a radar frame is reported in Fig. 3.3: a first FFT is computed on the I/Q sampled beating frequency signal to extract range information; a second FFT is computed for each range bin across all the chirps to extract the Doppler information; and a third FFT is computed for each range/ doppler bin across the virtual antennas to extract AoA information. These radar processing steps were implemented on the integrated DSP of the AWR1843 chipset.

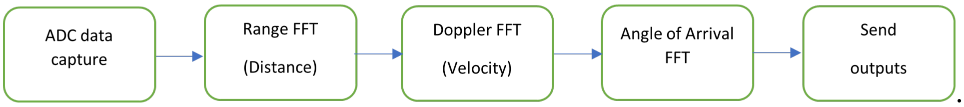

Fig. 3.3 Radar signal processing chain

Due to the presence of two SFs, the processing chain was repeated for both of them, and at the end of the two SFs an algorithm to estimate the ego velocity of the radar host and another to associate the detected points of the two SFs were implemented. However, the two SFs as mentioned in Chapter 3.1 are different, and for this reason, they require slightly different processing. The first SF is necessary to have a better angular resolution thanks to the three transmitting TXs. As explained in Chapter 3.6, since the system exploits TDM to achieve orthogonality the velocity of targets is required to correct the Doppler-induced phase shift across multiple TX antennas and perform the AoA FFT. This issue is not present, instead, if all TXs are transmitting simultaneously during the frame. At first, the angle of arrival is computed in the first SF with the signal of only one TX while the FFT input vector with signals received from all the TXs is kept in memory. At the end of both SFs, when the velocity has been measured and the targets of the two SFs have been associated the AoA FFT is recomputed with all the MR MIMO elements to obtain the final angular resolution.

The second SF implements velocity disambiguation (algorithm described in detail in Chapter 3.7), performing Doppler FFT on both the fast and the slow chirps. Another difference between the SFs is that for the second SF, the detected points are grouped by a peak grouping algorithm to facilitate association. The first SF, instead does not group any points since the tracking algorithm requires a minimum number of points per generated track to work properly. The local maximum of the detected peaks in the range-Doppler matrix are identified as Point Cloud Masters (PCM) while the points around the local maximum both in range and Doppler are identified as Point Cloud Slaves (PCS) of that maximum. The detected points of the second SF, with the obtained disambiguated velocities, are associated with the PCMs of the first SF.

A detailed description of the radar firmware implemented on the DSP with memory allocation, memory transfer, and order of operations is given in the following paragraphs.The AWR1843 as already mentioned has two ADC buffers (Ping-Pong) 32 kB each to permit processing while receiving data. In the buffer, the data for each antenna are accumulated consequently (first all chirps for RX0, then all the chirps for RX1, and so on). When one of them is full, with a number of chirps equal to the parameter NumChirpPerChirpEvent set in the DSP firmware, a $CHIRP\_EVT$ is raised and the processing on the chirps in the full buffer starts while the other buffer gets filled (with new data). Given the number of ADC samples per chirp ($N_{ADC} = 256$), bytes required for an I/Q sample ($N_B = 4$ B, 16 bits for the imaginary, 16 bits for the real part), and the number of RX ($N_{RX} = 4$), the maximum value for NumChirpPerChirpEvent is 8 since, $8N_{ADC}N_BN_{RX} = 32$ kB.

When the $CHIRP\_EVT$ is raised the **chirpProcess** function is executed. For the first SF, The chirpProcess function operations, summarized in Fig. 3.4, are:

- Data are Enhanced Direct Memory Access (EDMA) transferred from ADC buffer in L3 memory to ADCdataIn in L1 memory of the DSP in a Ping-Pong manner while counters are updated to keep note of chirp and TX numbers.
- Windowing is applied to the samples: a Blackman window [35] is applied for range FFT.
- Range FFT is performed on the I/Q samples.
- Outputs are EDMA transferred in L3 memory to the RadarCube where all values are stored for each TX, each RX, each chirp, and each range bin. These operations are repeated for each $CHIRP\_EVT$ alternating the two ADC buffers as input of the 1D chain until a number of chirps equal to the variable numChirpPerFrame (numChirpPerFrame= NumDopplerBin*numTX) chirps have been processed.

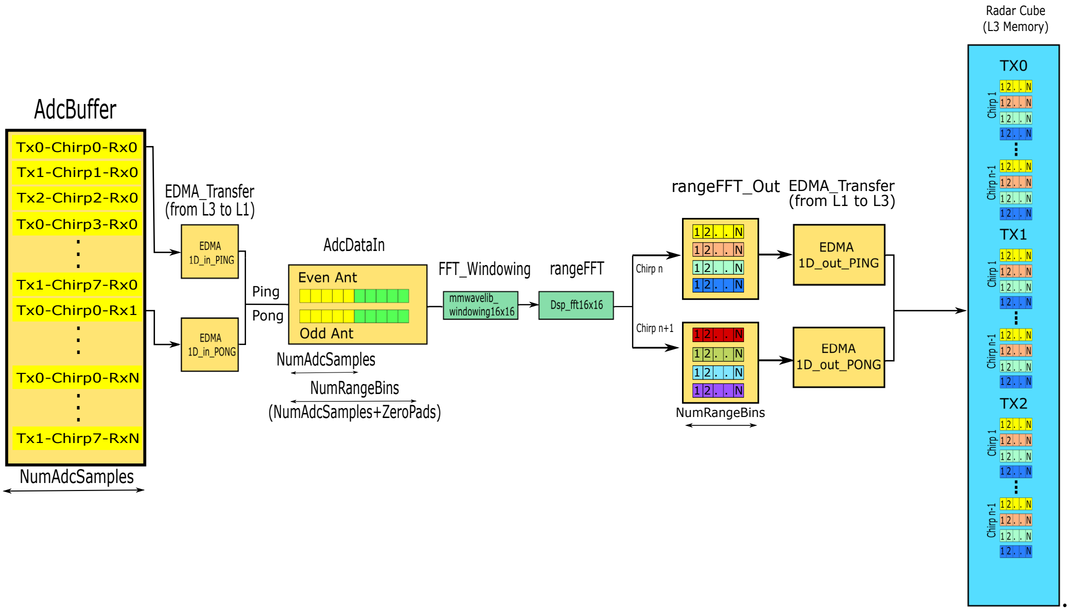

Fig. 3.4 Range FFT Datapath for first SF

When the RadarCube structure has been filled with all the processed chirps of the frame, the occupied memory can be viewed as a 3D structure as shown in Fig. 3.5 where in one dimension there are the range samples (Fast time) of a chirp, in one dimension there are all the different chirps (slow time), and in the third one, there are the receiving antenna channels.

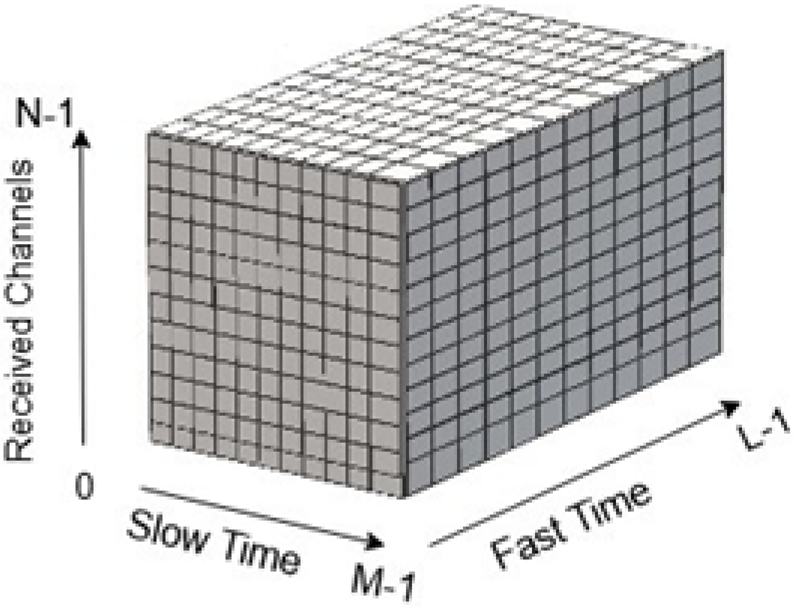

Fig. 3.5 Radar Cube representation

After the completion of chirpProcessing for all chirps, the **interFrameProcessing** function is executed. The interframeProcessing function computes:

- Doppler FFTs for velocity calculation.
- Results are stored as absolute values (only magnitudes to reduce memory occupation) in DetMatrix previously allocated in L3 memory.
- Constant False Alarm Rate (CFAR) in both Doppler and range direction.
- FFT for AoA estimation.
- Calculation of XY coordinates of detected objects.

The interframeProcessing function can be subdivided into velocity-targets calculation and Azimuth-XY calculation. The velocity-targets calculation steps, summarized in Fig. 3.6 and Fig. 3.7, are:

- Data are EDMA transferred from RadarCube in L3 memory to dstPingPong buffer in L1 memory alternating odd and even chirps in a ping-pong manner.
- Windowing is applied to the samples: a Hanning window is applied for Doppler FFT.
- Doppler FFT is performed on the samples.
- Magnitudes of the detected values of all the receiving antennas are summed in log2 basis (Q8 format) for each Doppler bin.
- Outputs are EDMA transferred in L3 memory to the DetMatrix where values are stored for each range and each Doppler bin.
- CFAR threshold in Doppler direction is applied for each range bin.
- A bit corresponding to the range and Doppler of the objects that passed the threshold at a certain Doppler line is set in DopplerLineMask in L2 memory.
- CFAR threshold in range direction is applied for each Doppler line that has passed the previous threshold.
- A grouping function classifies the points that have passed both CFAR threshold as PCMs and PCSs. PCM and PCSs of the same peak are linked by an index which is saved in their structure.

- Range index, Doppler index, and magnitude values are stored, for each detected object in an ad hoc structure.

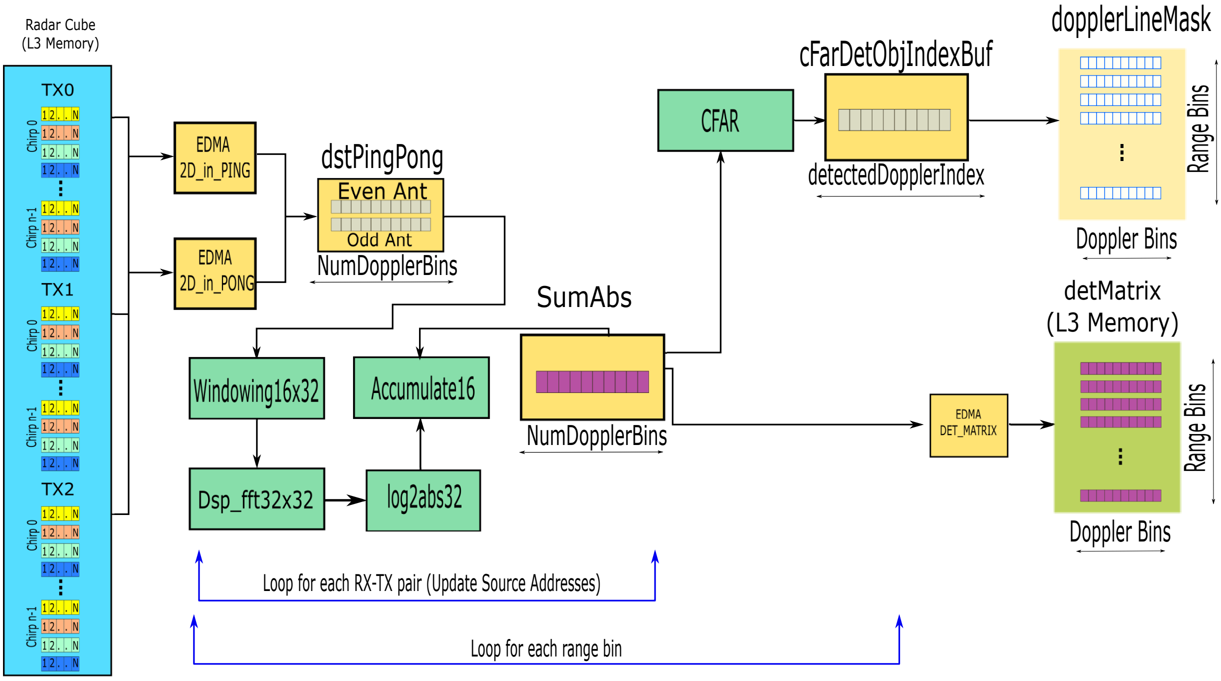

Fig. 3.6 Doppler FFT datapath (part 1)

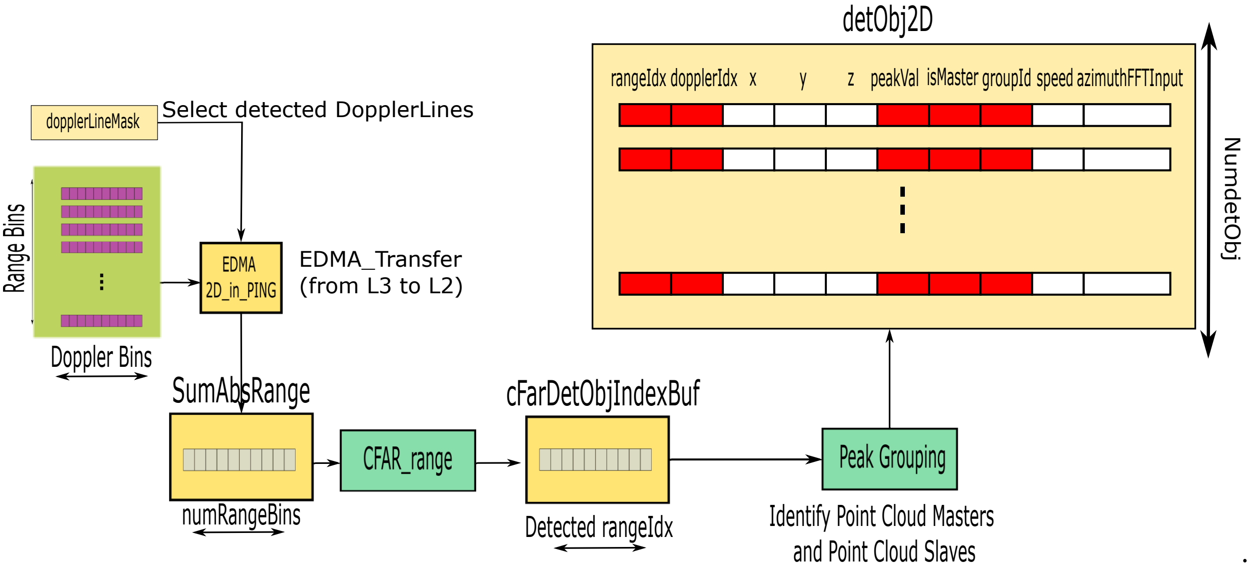

Fig. 3.7 Doppler FFT datapath (part 2)

For azimuth-XY calculation, summarized in Fig. 3.8, the steps are:

- Data of the detected objects are EDMA transferred from RadarCube in L3 memory to dstPingPong buffer in L1 memory.
- Single point Discrete Fourier Transform (DFT) (32-bit precision for both real and imaginary parts) with windowing is performed at the detected range indices (since FFT for Doppler calculation is stored just in magnitude 16-bit precision).

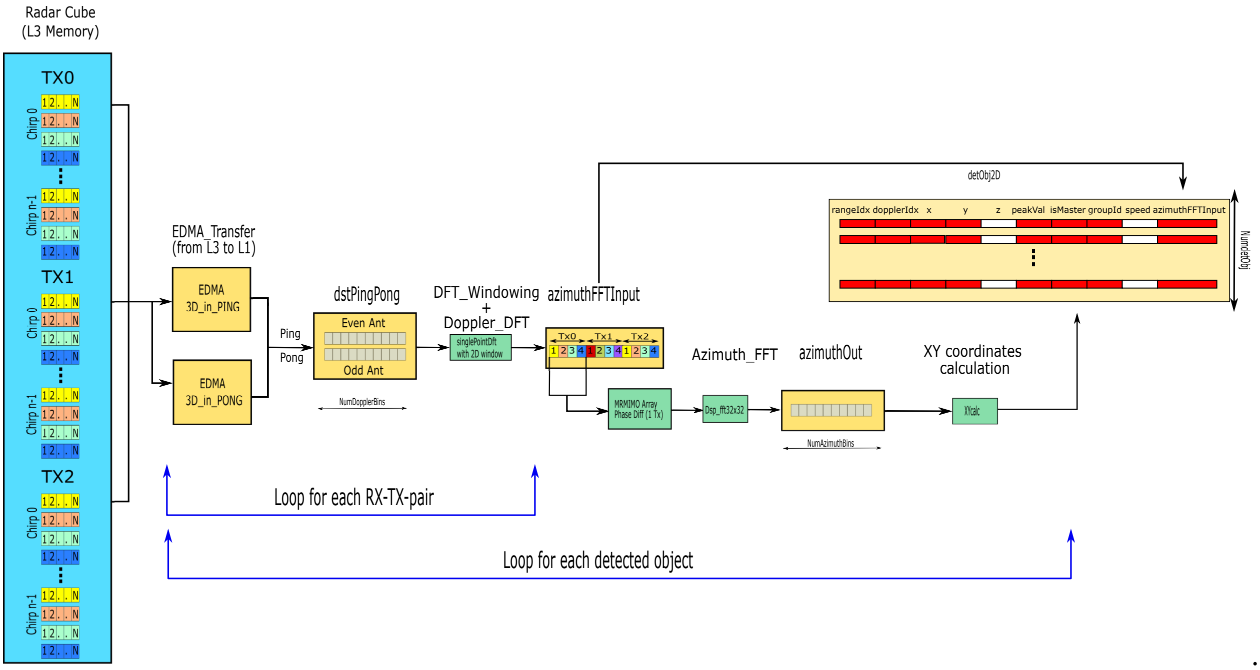

Fig. 3.8 Azimuth XY Datapath

- Phases of the signal for each RX are corrected with calibration coefficients (calibration phase is executed once for each radar board).
- Minimum Redundancy array with 1 TX and 4 RXs is filled with antenna phase differences as explained in Chapter 3.5.
- Zeropadding is applied.
- Azimuth FFT is performed on the samples of only TX1, while all the samples are stored in memory for Doppler correction with the disambiguated velocity obtained from the second SF.
- X and Y coordinates are then calculated and stored in detObj2D.

- If Azimuth Heatmap is requested azimuth FFT is computed, at the desired Doppler, for each range bin (not only to detect objects, i.e. more time is required).

When interframe processing for the first SF is completed, the DSS updates the SF index to select the processing datapath for the second SF, resets the counters, and waits for a new *CHIRP_EVT*. When the *CHIRP_EVT* of the first chirp of the second SF is raised the **chirpProcess** function is executed. For the second SF, the chirpProcess function operations, are the same for the first SF with the difference that all Txs transmit simultaneously is used and that two types of chirps are sent. The Radar Cube allocation is adapted to the bigger of the two subframes. The range FFT datapath for the second subframe is reported in Fig. 3.9 where the ADC buffers management and the positioning of fast and slow chirps in DSP memory can be observed.

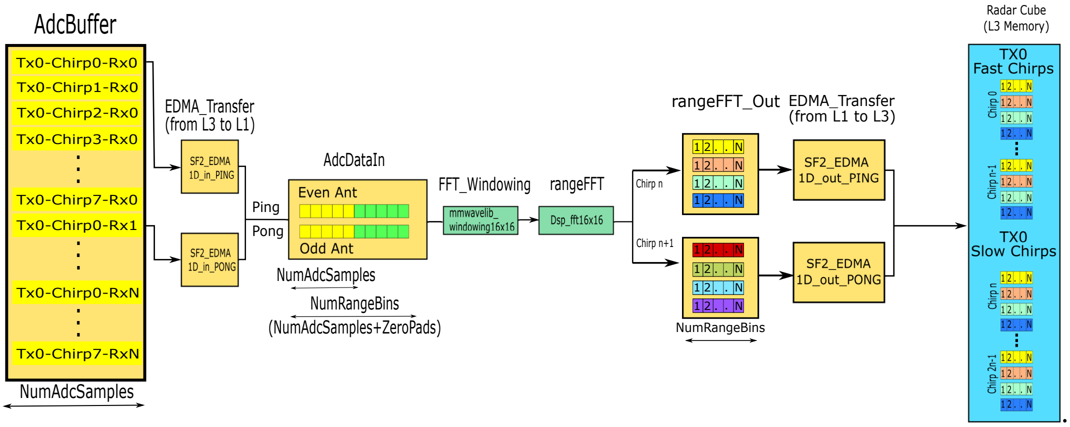

Fig. 3.9 Range FFT Datapath for second SF

After the completion of chirpProcessing for all the chirps of the second SF, the **interFrameProcessing** functions are executed. The interframeProcessing function computes:

- Doppler FFTs for velocity calculation.
- Velocity disambiguation.
- Results are stored as absolute values (only magnitudes to reduce memory occupation) in DetMatrix buffer previously allocated in L3 memory.
- CFAR in both Doppler and range direction.

- FFT for AoA calculation.
- Calculation of XY coordinates of detected objects.
- Ego velocity estimation.
- Association of points between the two SFs.
- Final XYZ coordinate of targets with complete virtual array

The velocity-targets calculation steps, summarized in Fig. 3.10 and Fig. 3.11, are:

- Data are EDMA transferred from RadarCube in L3 memory to dstPingPong buffer in L1 memory alternating odd and even chirps in a ping-pong manner.
- Windowing is applied to the samples: a Hanning window is applied for Doppler FFT.
- Doppler FFT is performed on the samples of the fast chirps.
- For each range, the magnitude values of the Doppler FFTs computed for the fast chirp and each virtual antenna are summed in log2 basis (Q8 format) and stored in the sumAbs vector.
- For each range, the magnitude values of the Doppler FFTs computed for the slow chirp and for each virtual antenna are summed in log2 basis (Q8 format) and stored in the sumAbsSlowChirp vector.
- CFAR threshold is applied to sumAbs to extract the Doppler Index of detected points.
- A bit corresponding to the range and Doppler of the objects which passed the threshold at a certain Doppler line is set in DopplerLineMask in L2 memory.
- Of the detected points only local maxima (actual peak value) are selected with a pruning function while other points are discarded.
- The disambiguation algorithm described in Chapter 3.7 is applied to the sumAbs and sumAbsSlowChirp vector. The computed disambiguated velocity is saved in a structure to be assigned to the target if it passes also the CFAR threshold in the range direction.

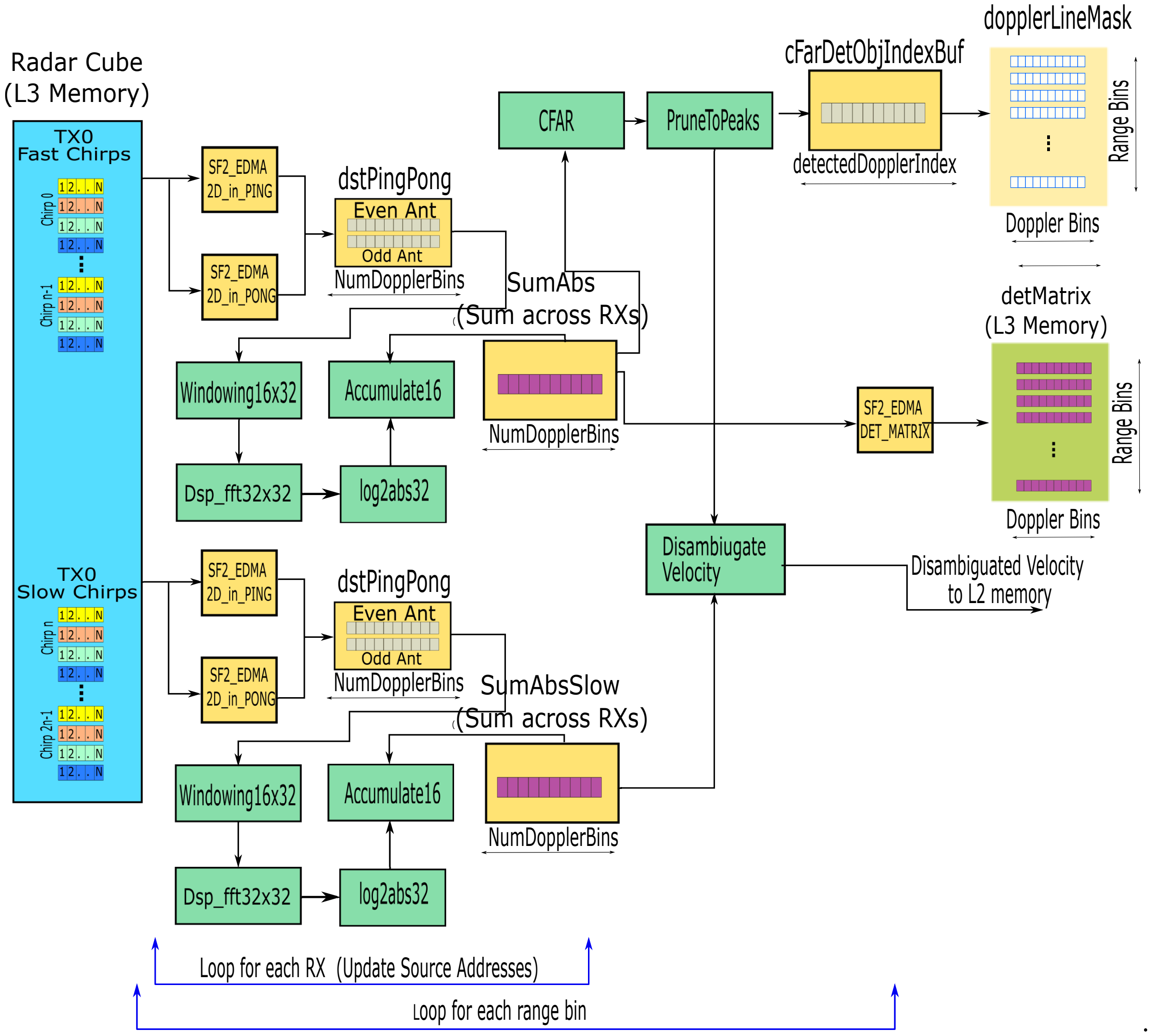

Fig. 3.10 Doppler FFT Datapath for second SF (part 1)

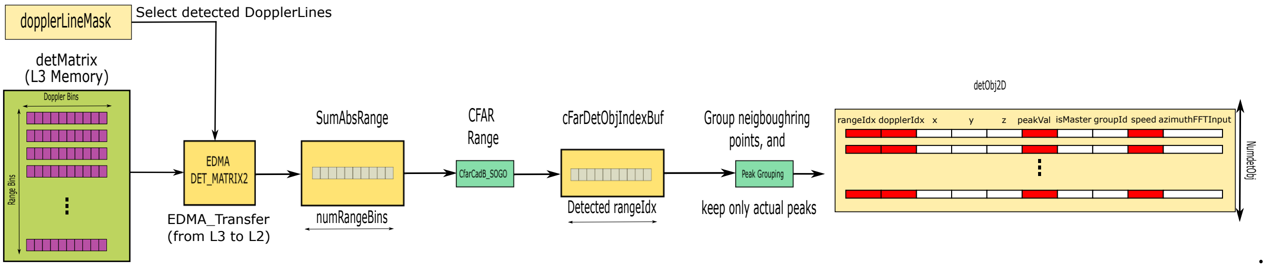

Fig. 3.11 Doppler FFT datapath for second SF (part 2)

- The sumAbs vector values are EDMA transferred in L3 memory to the DetMatrix where values are stored for each range and each Doppler bin.
- CFAR threshold in range direction is applied for each Doppler line which has passed the previous threshold and disambiguated velocities are assigned to the targets.
- A grouping function groups the points (near to each other) which have passed both CFAR thresholds. The points around a local maximum (fixed distance in both range and Doppler direction) are discarded and only the local maximum is kept in memory and identified as Point Cloud Master of the second SF.
- Range index, Doppler index, magnitude value, and disambiguated velocity are stored, for each detected object in an ad hoc structure.

For azimuth-XYZ calculation, the first steps are the same of the first SF while in the second part, summarized in Fig. 3.12, the final target list is created. The performed tasks are:

- Data of the detected objects are EDMA transferred from RadarCube in L3 memory to dstPingPong in L1 memory.
- Single point DFT (32 bits precision for both real and imaginary parts) with windowing is performed at the detected range indices.
- Phases of the signal received for each RX are corrected with calibration coefficients.
- Minimum Redundancy array is filled with antenna phase differences.
- Zeropadding is applied.
- Azimuth FFT is performed on the samples of the only transmitting TX.
- X and Y coordinates are then calculated and stored in the memory.
- Ego velocity is estimated with the algorithm described in Chapter 3.8.
- PCMs of the two SFs are associated by minimum distances criteria. The disambiguated velocity of the PCMs of the second SF is used to correct the Doppler phase shift of the stored FFTantennaInput for the PCMs of the first

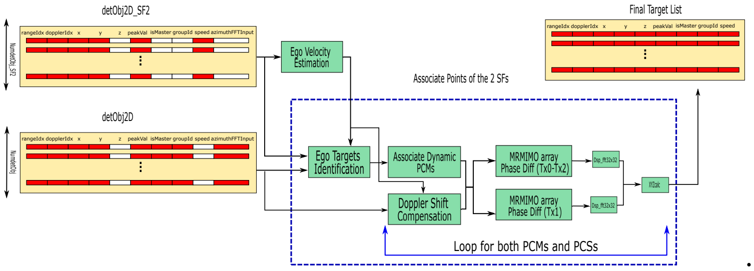

Fig. 3.12 Final target list creation

SF and its corresponding PCSs. After correction, the MRMIMO virtual array is fully filled as explained in Chapter 3.5, and azimuth and elevation DFTs are computed for all the points of the first SF.

- XYZ coordinates are computed.
- The final target list is composed of PCMs of the first SF, with disambiguated velocity, XYZ coordinates computed with fully filled MRMIMO array, and identifiers to distinguish PCM from PCS (isMaster flag) and their group (groupId).
- In the association function, ego velocity, is used with AoA information to separate ego targets from dynamic ones. Targets of the first SF recognized as ego targets are not associated with the PCMs of the second SF and their isMaster flag is set to a different value with respect to associated ones.

At the end of interframe processing, a list of outputs is transmitted in the form of packets to be parsed, or L3 addresses to be directly read from memory (for big size structure) through internal MailBox to the MSS for further processing and transmission to external interfaces. The outputs transmitted to the MSS are FFTs, CFAR thresholds, detected objects' start addresses (used as input for tracking algorithm and also for outputs transmission to the external interface), requested heatmap start addresses, and other auxiliary information.

3.4 Memory Allocation

Due to the finite size of the radar memory, and in particular of the DSP, extra care was taken in the allocation of data structures. An optimized allocation allows the storage of all the desired data while also speeding up the sum of the function by using data in faster memory (L1) and reducing the number of transfers from one memory to the other when possible. Dynamic allocation for the two SFs was necessary to reuse some of the memory occupied by the first SF into the second one. Doubling the memory occupation would have not been a feasible solution. Dynamic allocation was also used in the same SF noticing that some of the structures required for chirp processing were not used during interframe processing. However, some data structures could not be overwritten between the two SFs. For this purpose a portion of all three memories (L1, L2, L3) was dedicated to static allocations. The remaining memory space was dedicated to dynamic allocation. Some data structures were also allocated only for one SF or the other, freeing more space. This was fundamental to increase the number of detectable targets and to enable the transmission of heatmaps. Some details on the size of the structures are given in the following.

The L1 memory (32 kB) was mainly dedicated to the allocation of input and output vectors of the range and Doppler FFTs which require fast computation (especially the range one) to avoid real-time errors. L2 (256 kB) was dedicated mainly to the storage of the detected target information. This solution was necessary since the fields of the detected target data structures are accessed multiple times from the developed algorithms, and storing them in the L3 memory would have increased too much the processing time due to the slower memory access.

Table 3.4 Radar parameters for Radar Cube and Detection Matrix dimensions

Symbol	Description	1^{st} SF	2^{nd} SF
N_{Bs}	Number of Bytes per I/Q sample	4	4
N_{Bd}	Number of Bytes per Detection Matrix Sample	2	2
N_{rb}	Number of Range Bins	256	256
N_{db}	Number of Doppler Bins	64	64
N_{RX}	Number of RX Channels	4	4
N_{TX}	Number of TX channels	3	1
N_{Chirp}	Number of Chirp Types	1	2

L3 (1024 kB) was dedicated to the bigger data structures such as the Radar Cube which, with the radar parameters specified in Table 3.4, has size

$$size(RadarCube) = N_B N_{rb} N_{db} N_{RX} N_{TX} N_{Chirp} = 786.4kB(1^{st}SF)/524.4kB(2^{nd}SF), \tag{3.1}$$

and the Detection matrix with size

$$size(DetMatrix) = N_{db}N_{rb}N_{db} = 32768kB. \tag{3.2}$$

As can be seen, the Radar Cube and the Detection Matrix alone occupy a big portion of the L3 memory. The last part of the L3 was dedicated to data that needed to be shared between the DSP and the ARM without sending them through the limited internal mailbox (max 2 kB).

3.5 Minimum Redundancy MIMO

As mentioned in Chapter 2.4.3 to improve the azimuth resolution of the radar a minimum redundancy antenna scheme has been adopted. In the firmware, these modifications were taken into account to perform the AoA estimation correctly. In the uniform MIMO version, the input vector to the azimuth FFT was composed of the range-Doppler processed signal of each TX-RX couple, and zeropadding was applied to get a sufficient FFT accuracy. In the MRMIMO version, the number of input elements is superior to the number of TX-RX couples. All the 20 uniformly spaced elements of the virtual array are obtained by the phase difference of the RX-TX couples, thanks to the non-uniform spacing of the antennas positioned on the radar board. The obtained elements are ordered with increasing phase difference and the input vector is composed of the 20 elements and zeropadding is applied to get a sufficient FFT accuracy (64 FFT samples). In Fig. 3.13 a comparison of the azimuth FFT (not windowed) obtained with an ideal target at the boresight is reported. The MRMIMO FFT shows a narrower peak (improved resolution) without any distortion and holes confirming the improved performances.

The azimuth resolution obtained with the MRMIMO scheme with 2 TXs and 4 RXs and non-uniform spacing of the antenna is

$$\theta_{MRres} = \frac{2}{N_{MR}}\frac{180^\circ}{\pi} = 5.7^\circ \tag{3.3}$$

which is a huge improvement with respect to the uniform case

$$\theta_{res} = \frac{2}{N}\frac{180^\circ}{\pi} = 14.3^\circ. \tag{3.4}$$

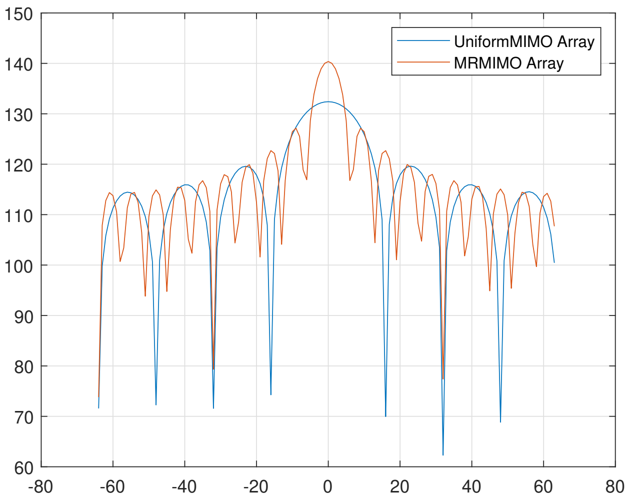

.

Fig. 3.13 Azimuth FFT Comparison of uniform MIMO vs MRMIMO

The TX-RX couple relative positions (u_{TX} and u_{RX} respectively, expressed in half wavelengths) used to compute the phase differences of the virtual array elements (u_a) are reported in Table 3.5 for clarity. From the table, it can also be noticed that when azimuth FFT is computed on signals received from only 1 TX ($u_{TX} = 0$ entries) the obtained virtual array is composed of 7 elements and the angular resolution is

$$\theta_{res} = \frac{2}{N_M ROneTX} \frac{180^\circ}{\pi} = 16.3^\circ \tag{3.5}$$

reaching almost the resolution of the 2 TXs by 4 RXs uniform array. Instead, the 1 TX by 4 RXs uniform array has an angular resolution

$$\theta_{res} = \frac{2}{N_{OneTX}} \frac{180^\circ}{\pi} = 28.6^\circ. \tag{3.6}$$

3.6 Doppler Induced Phase Correction

The TDM-MIMO frame allows obtaining a better direction of arrival resolution but, in non-stationary scenarios, the phase error induced by the switching time T_r between different TXs must be compensated.

In general, for M TXs the error due to the m-th TX at the same RX is [36]

Table 3.5 MRMIMO TX-RX couples (positions expressed in half wavelenghts) to compute phase differences

u_a	u_{TX};u_{RX}	u'_{TX};u'_{RX}
0	0;0	0;0
1	0;1	0;0
2	0;6	0;4
3	0;4	0;1
4	0;4	0;0
5	0;6	0;1
6	0;6	0;1
7	13;0	0;6
8	13;1	0;6
9	13;0	0;4
10	13;1	0;4
11	13;4	0;6
12	13;0	0;1
13	13,0	0;0
14	13;1	0;0
15	13;6	0;4
16	13;4	0;1
17	13;4	0;0
18	13;6	0;1
19	13;6	0;0

$$\Delta\tilde{\phi}_{TX_m} = 2\pi f_d T_r \frac{m-1}{M}. \tag{3.7}$$

Thanks to the estimated target Doppler frequency with the disambiguation algorithm of the second SF, a correction of the input signals for the direction of arrival calculation with signals from the first SF is correctly performed.

3.7 Chinese Reminder Theorem

As known from radar theory and explained in Chapter 1, if we consider a target with radial velocity v_t its Doppler frequency shift f_d is:

$$f_d = \frac{2v_t}{\lambda}. \tag{3.8}$$

If the Doppler frequency shift is larger than half of the PRF, the velocity is ambiguous and the Doppler shift satisfies the equation:

$$f_d = f_{meas} \pm nPRF. \tag{3.9}$$

where n is an integer number. Our approach to recover the correct velocity is the application of the Chinese reminder theorem as shown in [37] and [38].

The Chinese reminder theorem requires the adoption of K>=2 PRFs as in the second frame of our transmitted signals. In this way, the radar measures the Doppler shift induced by targets velocity with different resolutions. We can express eq. 3.9 in term of the Doppler bins (b_d),

$$b_d = b_{ad} + nM \tag{3.10}$$

where M is the number of Doppler bins and, b_{ad} is the ambiguous unsigned Doppler bin {0,1,..;M-1} defined as

$$\begin{cases} b_{ad} = \lfloor | f_{meas} \frac{M}{PRF} | \rfloor, f_{meas} => 0 \\ b_{ad} = \lfloor | M - f_{meas} \frac{M}{PRF} | \rfloor, f_{meas} < 0 \end{cases}, \tag{3.11}$$

The Chinese Reminder Theorem states that if the K PRFs are pairwisely coprime the system of congruence

$$b_d \equiv b_{ad_i} + n_i M, 1 < i < K \tag{3.12}$$

has a solution and the solution is unique. The solution of the system gives the disambiguated Doppler bin and thus the disambiguated velocity of the targets.

The theorem can be applied in the ideal scenario but noise must be taken into account for real applications. The measure of the Doppler bin can have uncertainty and even with an uncertainty of ± 1 bin the solution found for the system of congruence can be different from the real value of the ambiguous velocity by a huge margin. Going back to frequency the same system can be written as

$$f_d \equiv f_{meas_i} \pm n_i PRF, 1 < i < K \tag{3.13}$$

To find a solution to the system the value of n_i for both PRFs should be found. For this purpose, a minimum error approach has been applied in the developed algorithm.

A cycle of tries (NTRY) is applied and the error between the Doppler frequency shift calculated for the different values of n_i and for each PRF is calculated. The couple of n_i that gives the minimum error, if the error is below a certain threshold, is considered as winner and the disambiguated frequency calculated for the fast chirp f_{d1} is the output of the function.

The pseudo-code of the algorithm is here reported.

Algorithm 1 Pseudo-code of the algorithm for Doppler disambiguation.

```
for $\mathbf{i} = 0; \mathbf{i} < NTRY; \mathbf{i}++$
{$fd1 = fmeas1 + (i - (NTRY - 1)/2) * PRF1;$
    for $\mathbf{j} = 0; \mathbf{j} < NTRY; \mathbf{j}++$
    {$fd2 = fmeas2 + (j - (NTRY - 1)/2) * PRF2;$
        if $(abs(fd1 - fd2) < minToll)$
        {$minToll = abs(fd1 - fd2);$
        $fdreal = fd1;$
        }
    }
}
```

An example of the algorithm result for $NTRY = 3$ is reported in the graph of Fig. 3.14: the blue curve is the range of real velocities of the target; the red and yellow curves represent the velocities measured with the two PRFs limited by the ambiguity, and the purple curve shows the recovered velocities which, in this cases match the real one.

With $NTRY = 3$, the unambiguous velocity is extended up to 3 times (including positive and negative directions) with respect to the original ones. Increasing the number of tries can extend further the velocity range.

3.8 RANSAC for Ego Velocity Estimation

As already explained, the estimation of the ego velocity of the radar is necessary to separate the so-called ego targets from the Dynamic ones. The ego velocity can be estimated in different ways: with mechanical rotation of the sensor, with a mixture of sensors such as gyroscopes, wheel speed sensors, and accelerometer, or by performing statistical analysis of the radar data with specific algorithms. One of these

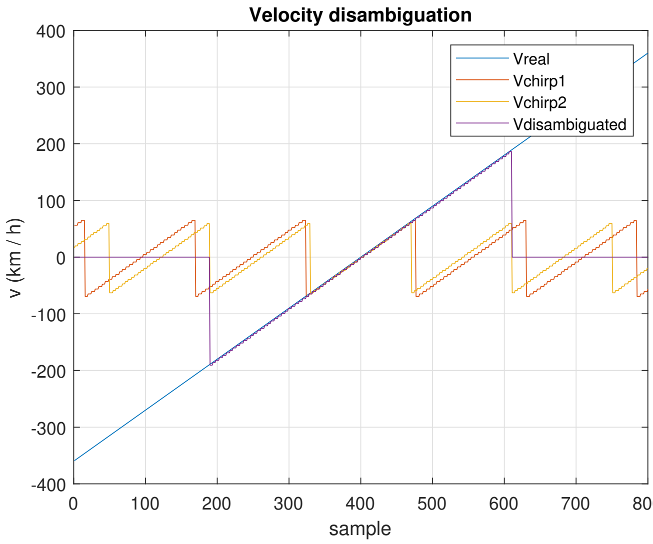

Fig. 3.14 Velocity disambiguated with two PRFs and NTRY=3

algorithms is the Random Sample and Consensus (RANSAC): an iterative algorithm that estimates the parameters of a mathematical model from a set of observed data points that contains both inliers (points that represent the most common trends) and outliers. The inliers are considered as correct points and are used to fit the model, while the outliers are considered to be the points affected by gross errors and thus should not be used for model fitting purposes. The RANSAC algorithm can filter out the outliers by iteratively taking a randomly chosen subset of points from the main data set. This set is then used to fit the mathematical model to the data subset, and then to verify its adequacy in terms of error with respect to the remaining data points. This process ends when the best fit is found or the limit of attempts is reached.

The RANSAC algorithm, developed for the radar of this thesis and implemented in the firmware, to estimate ego velocity follows the implementation presented in [39], where other possibilities (such as a least square error approach) have been explored but the results show that the RANSAC algorithm has better performances when the number of outliers increases. Since only a straight path was initially considered for the movement of the car, the parameter to be estimated from the algorithm is only the sensor velocity and not the heading direction.

The Ego Velocity Estimation routine is implemented as a voting algorithm which bases its vote on the amount of error of a given point with respect to the set of points. The RANSAC algorithm bases its effectiveness on the statistics of a distribution of points. It is done by taking a sample made as a subset of points randomly picked from the larger set. This new set can still be meaningful if the points of the smaller one are taken randomly from the larger one. By doing so, the smaller set has a certain probability of having its mean velocity converge to the trend of the larger set. In order to increase that probability, the estimation is performed more than once, up to a certain number of points, finally extracting the velocity of the subset that produced the smallest error.

The algorithm is structured in order to pick a random set of points from the given list of targets. Then, it proceeds to evaluate which one of these selected points has the least velocity distance with respect to the others. Multiple attempts are performed by trying to take a different set of points for the sub-set. The point which accumulated the least amount of error has then its velocity reported as the chosen one.

Since the radar is mounted with an angle $\beta = 35^\circ$ with respect to the car axis, as shown in Fig. 3.15, this must be taken into account for the estimation. The radial velocity (v_{r_i} measurements given by the radar when the car is moving and the sensor has velocity V_s is strongly dependent on the angular position of the targets θ_i. The relation between v_{r_i} and V_s is

$$v_{r_i} = -cos(\theta_i)cos(\alpha)Vs - cos(\theta_i)cos(\alpha)V_s \tag{3.14}$$

where α is the heading direction of the car. Normally two random points with measured v_{r_i} and θ_i need to be selected for each iteration of the RANSAC to determine V_s and α. Since the tests, presented in Chapter 4, were performed following straight paths the algorithm was simplified considering $\alpha = 0$, and under this assumption the relation becomes

$$v_{r_i} = -cos(\theta_i)Vs. \tag{3.15}$$

In this simplified form only one random point needs to be selected to determine V_s for that iteration. The final ego velocity of the car considering a straight path is obtained by rotating the sensor velocity vector to align with the car axis.

$$V = V_s \cos\beta \tag{3.16}$$

The firmware function that performs the association of the targets of the two SFs also fills a structure with the expected Doppler indexes of ego target for every possible angle bin. Targets that have a Doppler index and angle corresponding to the entry of the structure are considered inliers and therefore ego targets.

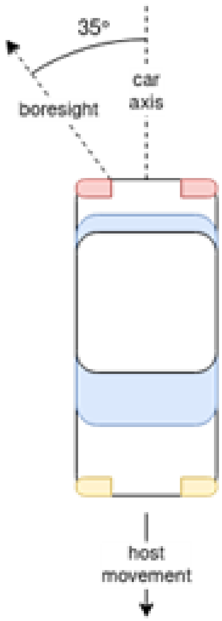

Fig. 3.15 Radar designed mounting angle

3.9 Ghost Target Detection

The effect of multipath propagation gives rise to the possible appearance of ghost targets. In our application, a similar approach to the one proposed in [40] is adopted to tackle this problem. From the estimated values of the range at which ghost targets typically appear, a threshold (Δ_{Rth}) on the difference of distance between the ghost target and the real one can be obtained. If a tracked target is within Δ_{Rth} from another, then it is marked as a probable ghost. To confirm the ghost's presence, a velocity check is performed. The ghost velocity measure is usually similar to the one of the real target even if it can differ slightly since the multipath has a different direction of arrival. Therefore, if the difference in velocities between the real target and the ghost candidate is within a certain limit, the ghost is confirmed and removed from the target list.

3.10 Tracking

The tracking layer of a radar should take the point cloud data, perform target localization, and report the results to a higher layer (e.g., the Classification layer). The output of the tracker is a set of tracked objects that gives information about their position, velocity, physical dimensions, and other features that can be used by a classifier to make an identification decision. The tracking algorithm implemented on the prototyped radar required to allocate a lot of memory since multiple matrices, and many parameters needed to be stored for each created track. Since the algorithm did not require very fast processing, it was implemented on the R4F ARM processor where more memory was available with respect to the DSP. Indeed the ARM was used primarily as the master of the radar operations and for external interfacing (with dedicated allocation, e.g. buffers for SPI/CAN, and other I/O interfaces), and therefore the memory was not heavily exploited for data storage. At the end of both SF processing the ARM receives the list of detected dynamics targets (isMaster=0 or 1) from the DSP. This choice is due to the fact that if a new track had to be created for each static target, memory occupation, and processing cost would not be feasible for the realized radar hardware. The list of targets with range, angle, and radial velocity is directly given as input for the tracking function.

The targets detected by the radar are grouped by means of an elliptical gating [41] in the three dimensions. The centroids of measurements of the groups are computed and by means of a multidimensional Kalman filter [42] with 3 inputs (range, angle, radial velocity) and 6 states (x, y, V_x, V_y, a_x, a_y) the group of points is tracked, while also computing group dimension.

The model used from the Kalman is a 2D space, constant acceleration model which is described in the following.

The state of the filter is

$$s(n) = Fs(n-1) + w(n) \tag{3.17}$$

where the state vector s(n) is defined in Cartesian coordinates,

$$s(n) = \begin{bmatrix} x(n) & y(n) & \dot{x}(n) & \dot{y}(n) & \ddot{x}(n) & \ddot{y}(n) \end{bmatrix} \tag{3.18}$$

the time-dependent transition matrix F of the filter is

$$F = \begin{bmatrix} 1 & 0 & \Delta t & 0.5\Delta t^2 & 0 & 0 \\ 0 & 1 & 0 & 0 & 0.5\Delta t^2 & 0 \\ 0 & 0 & 1 & 0 & \Delta t & 0 \\ 0 & 0 & 0 & 1 & 0 & \Delta t \\ 0 & 0 & 0 & 0 & 1 & 0 \\ 0 & 0 & 0 & 0 & 0 & 1 \end{bmatrix} \tag{3.19}$$

and w(n) is the process noise vector.

The 3 input measurement vectors u(n) are composed of range, angle, and radial velocity

$$u(n) = \begin{bmatrix} r(n) \\ \theta(n) \\ \dot{r}(n) \end{bmatrix}^T . \tag{3.20}$$

The measurement vector is linked to the state of the system by the following relation

$$u(n) = H(s(n)) + v(n), \tag{3.21}$$

where the measurement matrix H is

$$\mathbf{H}(\mathbf{s}(n)) = \begin{bmatrix} \frac{x}{\sqrt{x^2+y^2}} & \frac{y}{\sqrt{x^2+y^2}} & 0 & 0 & 0 & 0 \\ -\frac{y}{x^2+y^2} & \frac{x}{x^2+y^2} & 0 & 0 & 0 & 0 \\ 0 & 0 & 1 & 0 & 0 & 0 \end{bmatrix}, \tag{3.22}$$

and v(n) is the vector of measurement noise.

The relation between measurement vector and state is non-linear but it can be simplified by using an Extended Kalman Filter where the Taylor Expansion of H is retained at the first term and is evaluated at $s_{apr}(n)$ which is the estimation of s(n) based on n-1 measurements. The expression for the measurement vectors u(n) becomes

$$u(n) = H(s_{apr}(n)) + J_H(s_{apr}(n))[s(n) - s_{apr}(n)] + v(n). \tag{3.23}$$

The expression for the Jacobian of H(s) is also reported for completeness of information

$$\mathbf{J_H}(\mathbf{s}) = \begin{bmatrix} \frac{\partial r}{\partial x} & \frac{\partial r}{\partial y} & \frac{\partial r}{\partial \dot{x}} & \frac{\partial r}{\partial \dot{y}} & \frac{\partial r}{\partial \ddot{x}} & \frac{\partial r}{\partial \ddot{y}} \\ \frac{\partial \phi}{\partial x} & \frac{\partial \phi}{\partial y} & \frac{\partial \phi}{\partial \dot{x}} & \frac{\partial \phi}{\partial \dot{y}} & \frac{\partial \phi}{\partial \ddot{x}} & \frac{\partial \phi}{\partial \ddot{y}} \\ \frac{\partial \dot{r}}{\partial x} & \frac{\partial \dot{r}}{\partial y} & \frac{\partial \dot{r}}{\partial \dot{x}} & \frac{\partial \dot{r}}{\partial \dot{y}} & \frac{\partial \dot{r}}{\partial \ddot{x}} & \frac{\partial \dot{r}}{\partial \ddot{y}} \end{bmatrix} = \begin{bmatrix} \frac{x}{\sqrt{x^2+y^2}} & \frac{y}{\sqrt{x^2+y^2}} & 0 & 0 & 0 & 0 \\ -\frac{y}{x^2+y^2} & \frac{x}{x^2+y^2} & 0 & 0 & 0 & 0 \\ 0 & 0 & 1 & 0 & 0 & 0 \end{bmatrix} \tag{3.24}$$

The tracking function at each iteration performs the following operations.

- Prediction - this step computes the predicted estimates:
  - the apriori state
    $$s_{apr}(n) = Fs(n-1) \tag{3.25}$$
  - the apriori error covariance
    $$P_{apr}(n) = FP(n-1)F^T + Q(n-1) \tag{3.26}$$
    where Q(n) is the process noise covariance matrix.
  - measurement matrix $H(s_{apr}(n))$.
- Association - this step tries to associate the detected point cloud data to the existing tracks by constructing a 3D space around the centroids of the tracked objects that acts as a gating function. For each point that is inside the gate of a track a score based on distance is computed. The score is used to resolve cases where a point enters the gates of multiple tracked objects.
- Initialization: this Kalman filter step groups the points that are not already associated and creates a new track object if a group with a sufficient number of points defined with a parameter is found. The new tracked object centroid is given by an average of the group points.
- Updating - this step computes all the necessary innovations:
  - The measurement residual
    $$y(n) = u(n) - H(s_{apr}(n) \tag{3.27}$$

- Innovation covariance

$$C(n) = J_H(s_{apr}(n))P_{apr}(n)J_H^T(s_{apr}(n)) \tag{3.28}$$

- the Kalman gain

$$K(n) = P_{apr}(n)J_H^T(s_{apr}(n))[C(n)]^{-1} \tag{3.29}$$

- the state vector

$$s(n) = s_{apr} + K(n)y(n) \tag{3.30}$$

- The error covariance

$$P(n) = P_{apr}(n) - K(n)J_H(s_{apr}(n))P_{apr}(n) \tag{3.31}$$

- The dimensions (spread of the points) in range, angle, and radial velocity, of the tracked objects are estimated considering the associated points at maximum distance from the centroids in the three considered dimensions.

- State management - this step updates the states of the tracked objects. A tracked object can be in 3 states: **FREE**, **DETECTION**, **ACTIVE**. The tracked objects are in the FREE state when the have not been allocated yet. When a tracked object is initialized it is brought in the DETECTION state. At each iteration, if enough points are associated with the tracked object (hit event), a hit counter is increased. The same counter is decreased after consecutive frames during which not enough points have been associated with the tracked object (miss event). When the hit counter reaches a threshold the tracked object is set in the ACTIVE state. When the tracked object is in the ACTIVE state, a miss counter is increased if no points have been associated. The miss counter is set to zero if a hit event occurs. If the miss counter reaches the threshold for consecutive misses the tracked object is set in the FREE state and allocated memory is released.

3.11 Data Transfer and Laptop PC Interface

The data generated from the radar needs to be sent to an external peripheral for further processing or post-processing analysis. As mentioned in Chapter 2.2 the radar is connected either to the SPI-Ethernet converter or to the CAN transceiver of the lamp. Different functions were developed and implemented on the R4F ARM to interface the AWR1843 chip to the KSZ8851SNL board and obtain the highest throughput possible which was 25 Mb/s with an SPI clock of 40 MHz. The throughput was limited mainly by the compatibility of the AWR1843 chip with the SPI-Ehternet Chip packet queue. In particular, the AWR1843 chip, for the transmission of multiple packets in a row, required several chip select transitions slowing down the overall throughput. The SPI-Ethernet chip has an internal MAC address and communicates with the laptop through a 100 Mbps Physical layer.

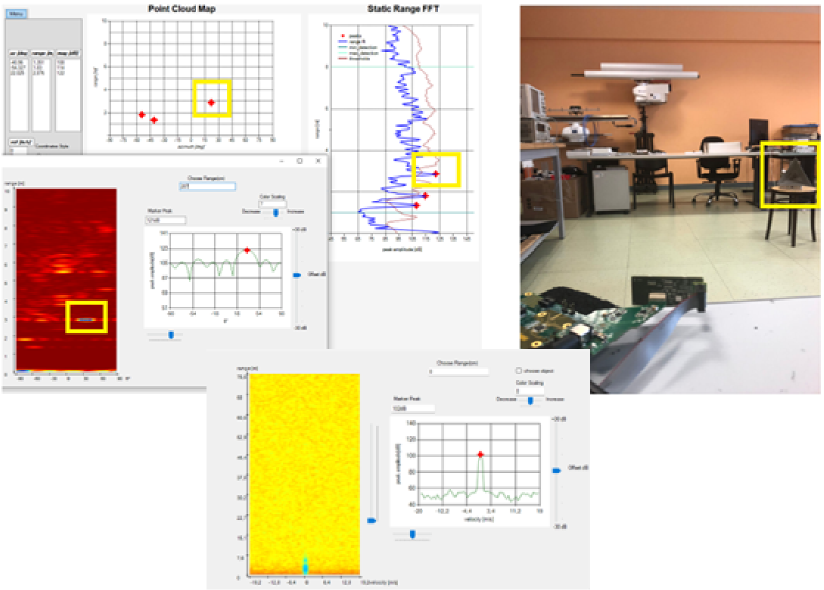

Fig. 3.16 Screen of the interface

A laptop PC interface was developed in C# language for real-time visualization of the radar data received from the radar through an Ethernet connection. The data received on the Ethernet connection are parsed and visualized on different plots and heatmaps. The interface provides the user with the possibility of saving the data for further post-processing.

From the interface, the radar can be started and stopped, and all the radar parameters can be updated and saved to the flash memory. A procedure to update the firmware of the radar was also implemented and a new binary file can be downloaded on the flash memory directly from the interface. A screen of the realized interface is reported in Fig. 3.16 where a detection from the radar performed in the laboratory with a corner reflector positioned at 2.8 m distance is reported. The azimuth-range map is visualized in real-time, as well as the zero Doppler range FFT with CFAR thresholds, target plots in Cartesian coordinates, and the list of targets with XYZ coordinates and peak magnitude information. A Doppler-range map from another detection is reported in the image (only one of the two maps can be sent due to the time required for the transmission). In the version of the interface utilized during the tests performed on the road, information about ego velocity, static/dynamic targets, PCMs/PCSs, and tracking were also visualized in real time. From the menu on the upper left, the radar can be stopped and restarted, and the parameter can be changed.

For the CAN solution, the data were organized and sent as CAN packets following the standard of Fig. 3.17. The packet is composed of:

- An 11 bits packet identifier
- A 6 bits Control Field in which is specified also the data length
- An 8 bytes Data field
- A 16 bits Code Redundancy Control (CRC) field
- A 2 bits Acknowledgement field
- A 7 bits End of Frame field
- Bit stuffing is applied (If 5 consecutive equal bits should be transmitted a bit of opposite polarity is added to the transmitted frame) to maintain synchronization.

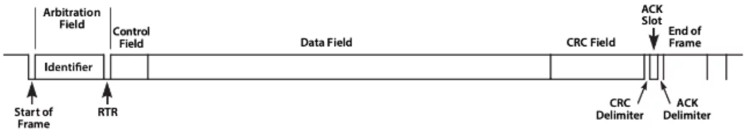

Fig. 3.17 CAN packet standard

The lamp motherboard presented a microcontroller, to mainly manage the lighting functions, and it was also dedicated to data reception. The microcontroller had a limited data management capability and required to be updated to a microcontroller with better performance.

Since the CAN prototype was designed for a demonstration, the data output of the radar was limited to a reduced number of targets, and the lighting function was updated in such a way, that if a target was detected in a zone in front of the lamp, the lamp OLEDs would start to blink for a few seconds. The communication was verified at first with an oscilloscope probe connected to the CAN transceiver installed on the lamp. Fig. 3.18 shows 12 CAN packets (1 per detected target) transmitted every frame with a data size of 64 bits. The content of the data was also verified by fixing the data value of certain packets.

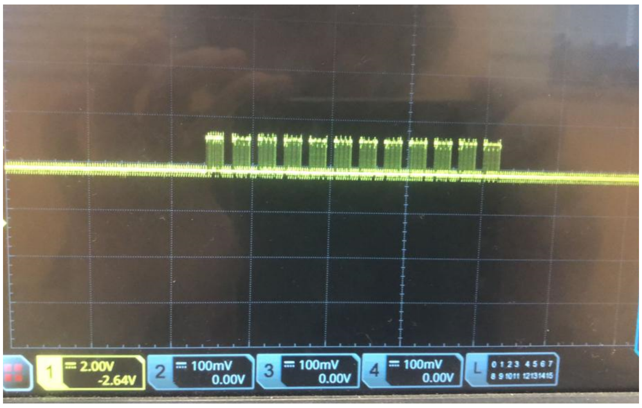

Fig. 3.18 CAN transmission of a frame

The correct reception was also verified with a CAN to USB converter connected to the vehicle connector present on the lamp motherboard and visualizing the received packets on CANalyzer from Vector [43]. An interface to visualize the received data on an XY coordinate plot was developed. A picture of the demonstrator test performed in the laboratory is reported in Fig. 3.19. The CAN packets were correctly received and parsed from the CANalyzer as shown from the point on the XY plot and the highlighted OLEDS were responding as expected.

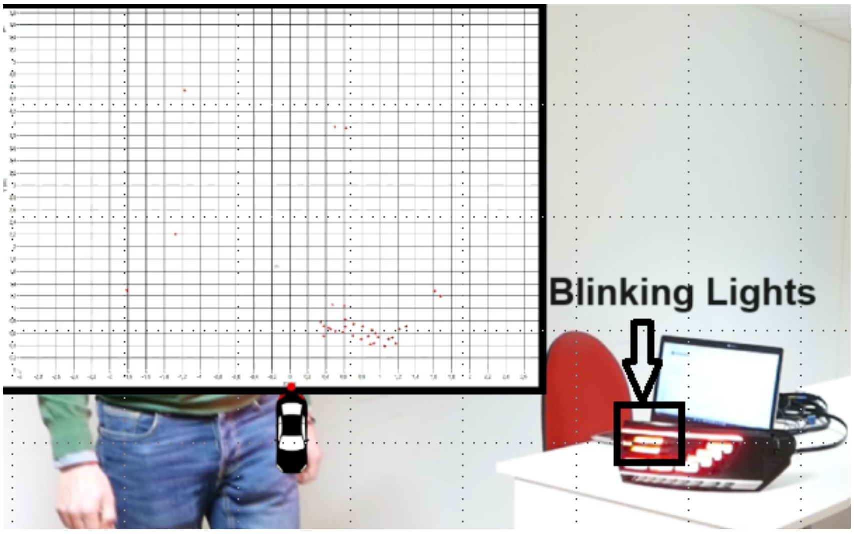

Fig. 3.19 radar with CAN in the lamp demonstrator

Chapter 4

Test Results

4.1 Validation

The radar functionality was tested at first in the laboratory. Both the radar board and the radar power board were initially checked to confirm the absence of any short circuits after fabrication. The radar power board was at first power supplied alone to verify that all the power rails levels were correct. The radar board was power supplied at first with a laboratory power supply to verify it was working properly. Then, the radar was connected to the radar power board, and the whole system functionality was verified. Firmware functionality was initially tested with static targets in an indoor scenario.

4.1.1 Power Supply Noise

As mentioned in Chapter 2, the first radar power board prototype mounted a noisy DC-DC converter whose bad performance was noticed during the laboratory test. A spectrum analyzer and a probe were used to measure the noise level present on the power rails of the radar board while the RF front end was active. In Fig. 4.1 the measurements for the 1.8 V rail when the switching frequency is set to 2 MHz are reported. The switching frequency and its harmonics affect the spectrum even at higher frequencies than 10 MHz and have peak values of several dB higher than the noise floor. A similar effect was verified on each power rail.

The effect of the noise was also clearly visible on the radar data as it is shown in the range-Doppler matrix response of Fig. 4.2. These were measured in an open field with only static targets present in the FOV of the radar. The switching

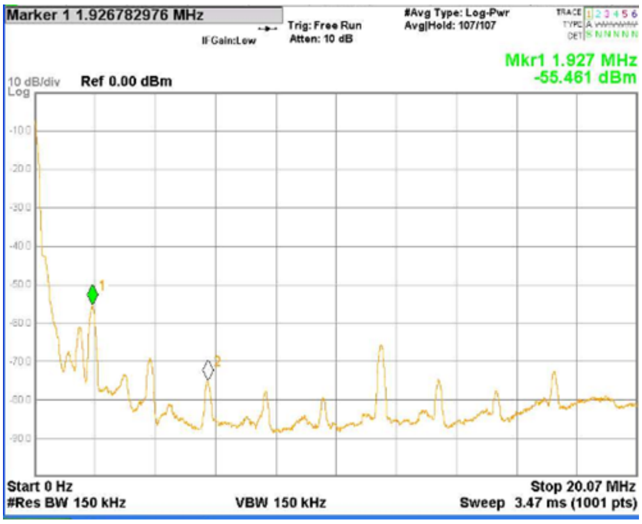

Fig. 4.1 Noise present on the 1.8 V rail on the radar

frequency and its harmonics modulated the chirps and caused multiple ghost peaks with variable phases to appear. A recurring peak at range = 48.2 m, corresponding to an IF frequency of 4 MHz, but with variable Doppler was detected, while a spread noise is located in the closer range of the radar. Some of the peaks were strong enough to pass the CFAR thresholds and caused errors in detection.

The power supply solution adopted for the second radar, with the DC-DC converter with spread spectrum capability solved this problem, and no evident noisy effects were identified during the test, as also shown in the detection Matrix obtained from the same open field measurements reported in Fig. 4.3.

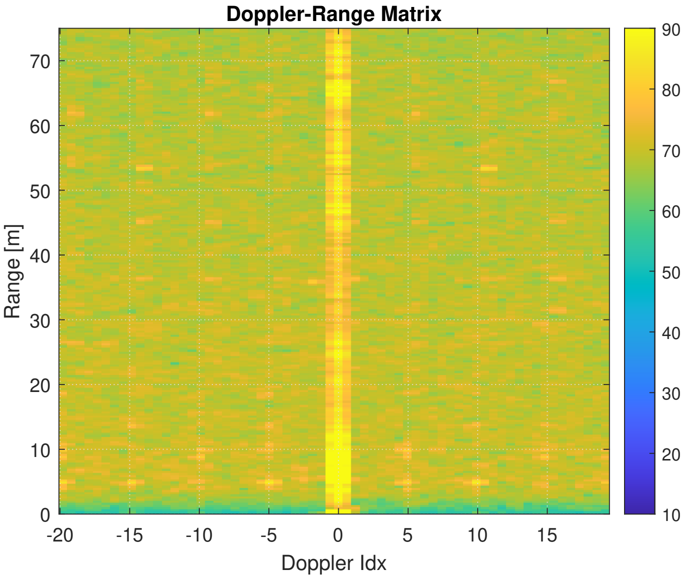

Fig. 4.2 Noise effect on the range-Doppler response of the first radar prototype

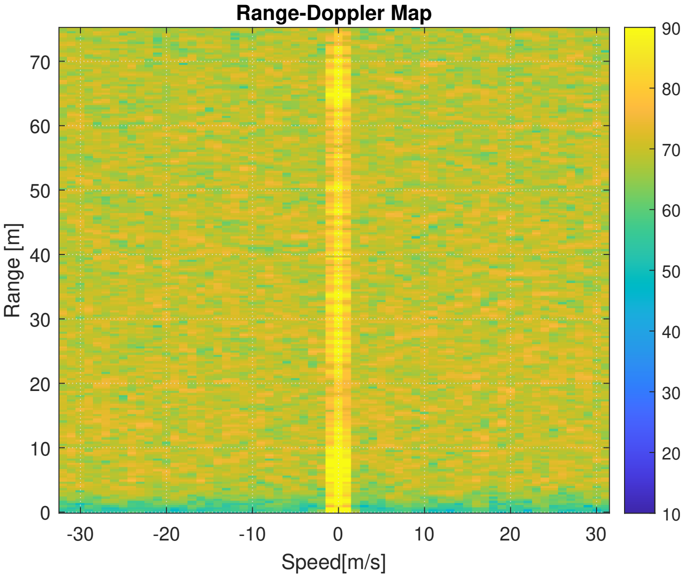

Fig. 4.3 Noise effect on the range-Doppler response of the second radar prototype

4.1.2 Thermal Measurements

For automotive standards, chip temperature must be controlled carefully, up to 70 °C ambient temperature. Heat chamber measurements of the radar system have been performed to verify that the maximum value of the radar chip junction temperature (the temperature of the internal semiconductor) stays below $T_{jmax} = 125$ °C.

In Fig. 4.4 a heat map of the running radar (1^{st} prototype) at ambient temperature outside the rear lamp is reported showing low values for the measured temperature.

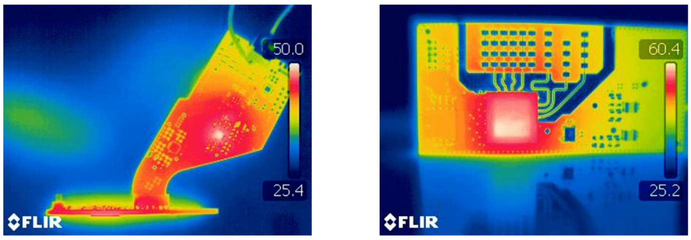

Fig. 4.4 Thermal camera photos of the boards at 25 °C

The running radar inserted in the rear lamp has been tested with lighting and electronics turned on, at different temperatures, in the heat chamber. A thermocouple sensor was attached to the case of the radar chip to measure the case temperature T_c and derive the internal junction temperature T_j as

$$T_j = T_c + \theta_{JC} P_d \tag{4.1}$$

where θ_{JC} is the case to junction thermal resistance specified on the data sheet and P_d is the average power consumption of the chip. The average power consumption of the running radar has been measured, on each power supply rail, by measuring the absorbed current with an oscilloscope, and the results are reported in Table 4.1.

Voltage rail	Mean current [mA]	Power consumption[W]
1.0V	70	0.056
1.24V	556	690
1.8V	155	236
3.3V	24	0.082
Total on RF board		1.15

Table 4.1 Power consumption of the Radar board

The radar and rear lamp set-up in the heat chamber is shown in Fig. 4.5.

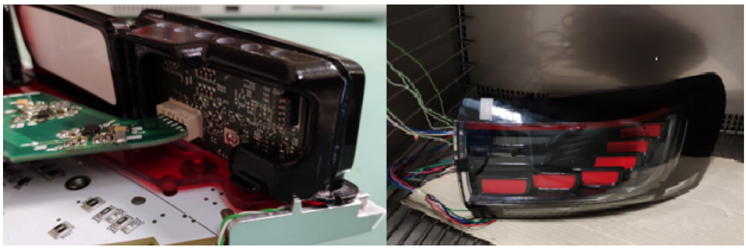

Fig. 4.5 Measurement Set-Up

The heat chamber was set at 40 °C, 60 °C, and 70 °C. When the temperature was reached, radar and light were turned on and the thermocouple values were read after 30 minutes of operations. The measured case temperatures T_c and the derived T_j, assuming the power consumption of Table 4.1, are reported in Table4.2. Only in the worst case scenario, with heat chamber temperature at 70 °C the $T_j = 129°C$ exceeded the maximum rating ($T_{jmax} = 125$°C).

T_{test}[°C]	T_{case} [°C]	T_j [°C]
40	101	106
60	106	111
70	124	129

Table 4.2 Thermal tests of radar in the rear lamp at different working temperatures (1^{st} prototype)

The same thermal tests were repeated for the second prototype and the results are reported in Table 4.3. The thermal results were better for the second prototype thanks to the improved heat dissipation of the board and the improved structure of the petal, modified to help airflow in the rear lamp. Even if, in this case, the junction temperature respected the maximum ratings of the chirp in the worst case, the margin was very small. A solution with a heatsink may be necessary to tackle this issue in the future.

T_{test}[°C]	T_{case} [°C]	T_j [°C]
40	97	102
60	102	107
70	119	124

Table 4.3 Thermal tests of the radar in the lamp at different working temperatures (2^{nd} prototype)

4.1.3 Calibration Procedure

During testing different radars were used and their installation into the rear lamp could lead to slightly different position offsets of the radar with respect to the petal. For this reason, calibration is required after installation.

The calibration procedure consisted of positioning a corner reflector at the boresight and at a known range which was communicated to the radar from the laptop PC interface. The radar was then set in Calibration Mode where it averaged the signals received for each TX-RX couple, at the specified range, for a certain period of time. These signals were then sent to the laptop PC interface which calculated the calibration coefficients forcing to zero the phase difference of all the antenna couples. The interface sent back the computed calibration coefficients to the radar. The calibration coefficients were flashed onto the QSPI memory at a fixed location ready to be read when required for angle correction. The radar was then restarted and if the calibration procedure was correctly executed the corner reflector was detected at $\theta = 0^\circ$ and at the known range.

4.2 Radar Tests with the Rear Lamp not Mounted on the Car

Initially, the radar was tested in an open field to verify the functionality of the system when a 10 dBsm corner reflector was positioned 16 meters at boresight with the radar outside the lamp, inside the lamp with the original petal, and inside the lamp with the optimized petal. In Fig. 4.6 the zero-Doppler range responses in these three scenarios, non-coherently integrated over multiple frames (3 minutes time windows) and averaged over time are shown and the peak amplitudes generated by the corner reflector are marked by the black lines. When the radar is inside the lamp with the original petal, the peak amplitude is 4.5 dB lower with respect to the case when the radar is outside the lamp. With the optimized petal thickness, the peak amplitude is 1.2 dB lower confirming the simulation results of Fig. 2.7 (negligible attenuation due to reflections) and showing a significant improvement.

The detected peak magnitude behavior with respect to the angle of arrival was verified to check if the lamp structure was obstructing the field of view of the radar. A 10 dBsm corner reflector was positioned at a distance of 10 meters and moved at 5° steps in the interval ±45°. The measured zero-Doppler peak value for the detected

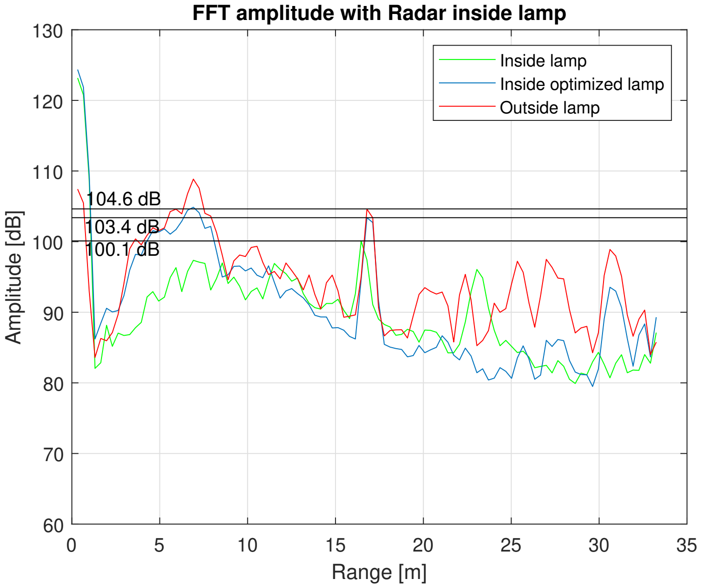

Fig. 4.6 10 dBsm corner reflector non-coherently averaged peak amplitude inside and outside lamp with different petal material thickness

corner reflector in each position was non-coherently integrated over multiple frames (30 seconds time windows). The test was repeated with the radar outside and inside the optimized lamp. The comparative result is shown in Fig. 4.7 where the measured amplitude for the outside case (blue point) and inside case (red points) are reported vs the azimuth angle of the corner reflector (θ). The received signal was attenuated across all the angles of 1 to 2 dB but no major blind spots in the radar field were detected.

Another set of experiments was performed to test the radar performances vs range. A 10 dBsm corner reflector was moved from 0 to 75 meters on the boresight. The range response amplitudes of the moving target at its Doppler index (blue curve), as well as the averaged noise floor at the same Doppler index (red curve) and the maximum value of the noise floor at the same Doppler index (green curve), are reported in Fig. 4.8. The radar response shows continuous detection over all ranges and a SNR of 11.5 dB at the maximum range of 75 m is still good for reliable detection.

A series of tests were performed in an open field with a 10 dBsm corner reflector moved on an "S" shape path. The radar detected the target in each frame with multiple points: the point cloud (blue and green dots) enabled the tracking algorithm

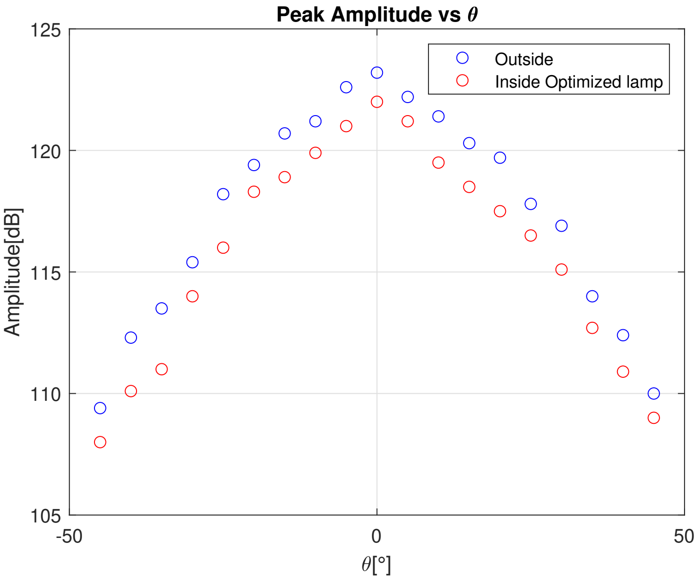

Fig. 4.7 10 dBsm corner reflector non-coherently averaged peak amplitude inside and outside lamp at different angles

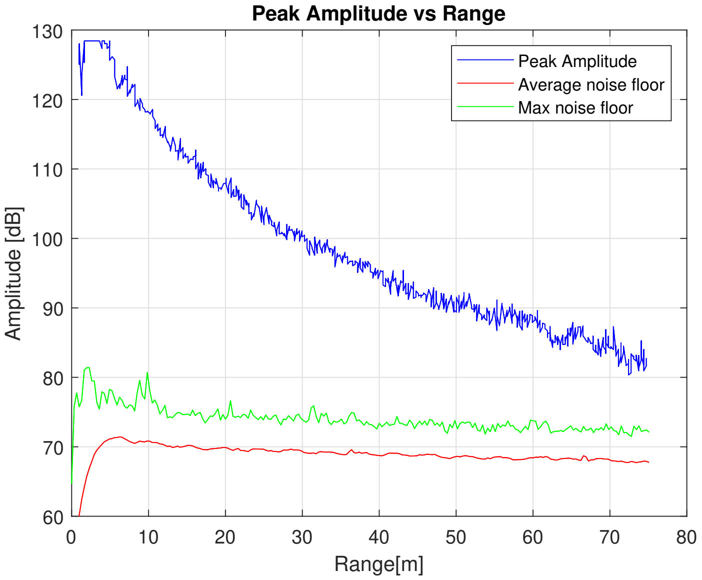

Fig. 4.8 FFT peaks of the corner reflector vs range 75 m

to follow the target even when the movement was transversal to the radar radial direction as shown in Fig. 4.9.

Relevant tests were performed on the road with realistic traffic scenarios. Several data on different days, times, and traffic conditions were collected to test algorithms

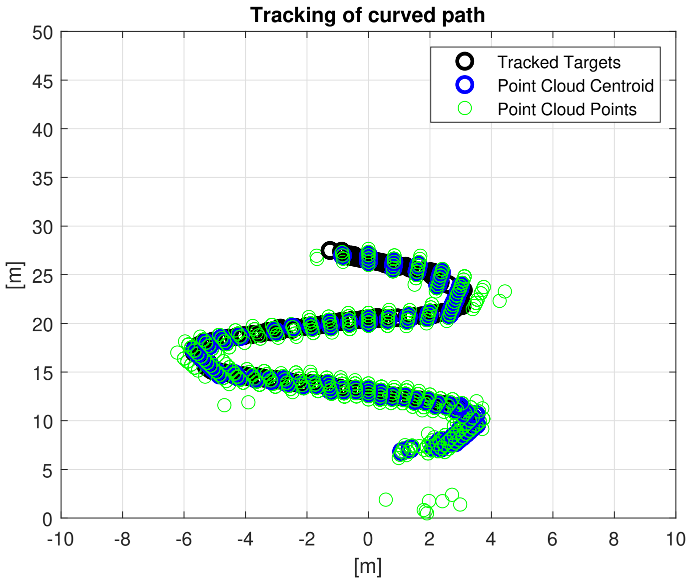

Fig. 4.9 Tracking of a "S" shape path with corner reflector

and radar performances. A typical scenario is reported in Fig. 4.10 where the radar was positioned at the center of a four lanes (two per traffic direction) road. The rear lamp equipped with the radar was laying on a static support between the two traffic directions slightly closer to one of the two and pointing upwards.

Fig. 4.11 shows a snap of the video collected during the test and the real-time processed radar output. In the reported example, two cars were approaching the radar at similar speeds next to each other and two cars were moving in the other direction in the same lane (one of the two cars is partially hidden by the poles in the image). All the moving cars were tracked (black dots) correctly in their respective lanes; a moving ghost target due to multipath reflections was identified and removed by the ghost removal algorithm (pink dots). The poles, trees, and some of the parked cars were detected as static targets (red dots). The blue lines limiting the road were added in post-processing. During a typical test, out of 437 vehicles followed by the tracking algorithm, 96.2% of them have been successfully tracked inside the correct lane. The wrong predictions were due to heavy traffic occluding targets or not enough resolution to separate very close targets at similar angles, speeds, and ranges.

Another set of tests was performed to verify the detection of crossing bicycles and pedestrians. The radar was positioned at a 30° angle with respect to a bicycle lane. In Fig. 4.12 the bicycle was successfully tracked while crossing from left to

Fig. 4.10 Top view of a road used for the radar tests

right. Two pedestrian crossings in the other direction were detected but not tracked due to their low velocity. The poles near the lane and the wall were detected correctly as static targets.

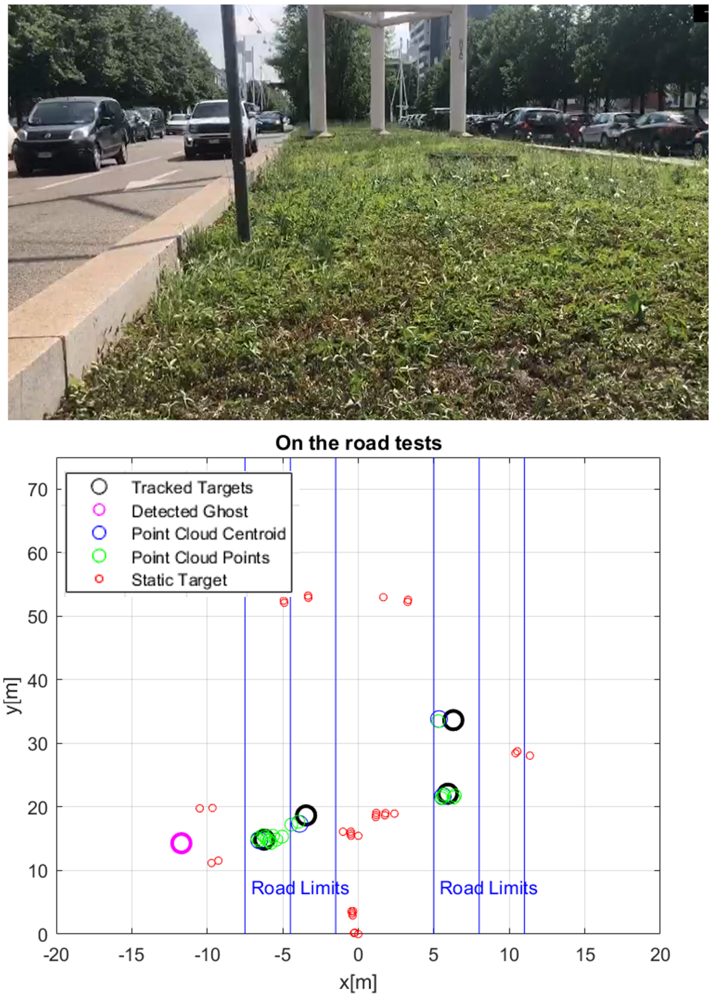

Fig. 4.11 Radar test on the road

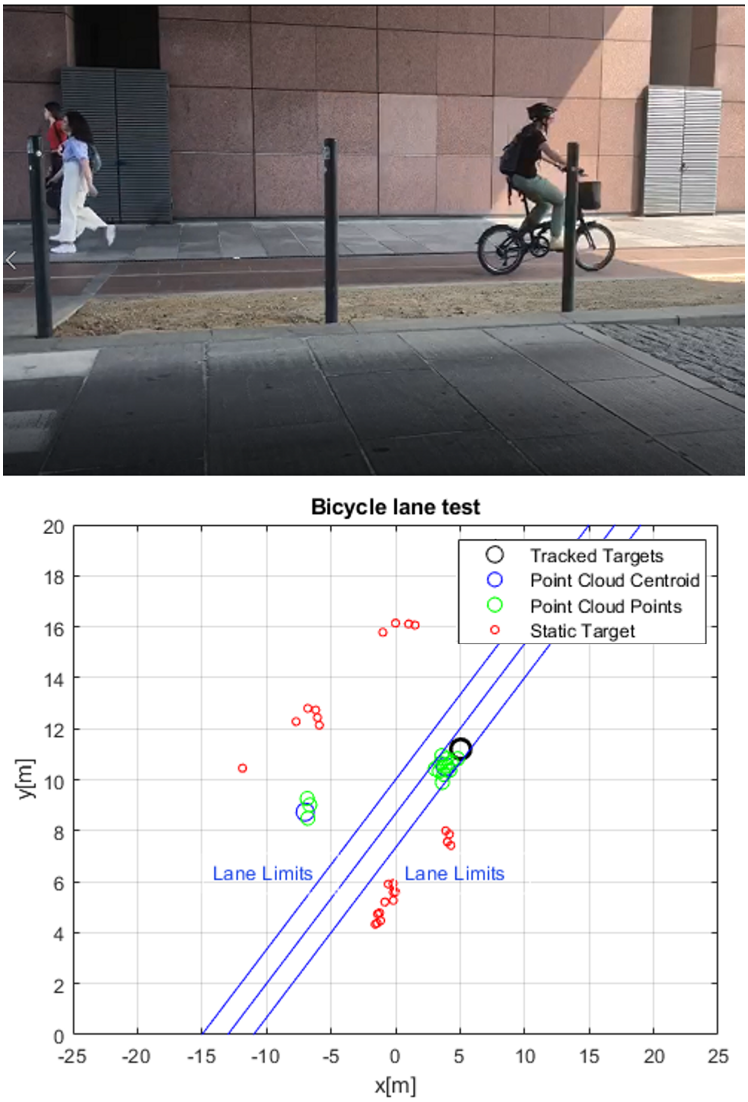

Fig. 4.12 Bicycle lane test

4.3 Radar Test with the Rear Lamp Mounted on the Car

A test campaign with the radar installed in the rear lamp mounted on a host car was carried out. The installation set-up is shown in Fig. 4.13. The lamp was adapted to be mounted on the host car which is not the model for which the lamp was originally designed.

.

Fig. 4.13 Radar installed on a Car

The radar, mounted on the rear-left side of the car was connected to the vehicle connector, from which it received 12 V as input to the radar power board (presented in Chapter 2.4). It pointed toward the rear of the car with an horizontal inclination of 35° with respect to the car's movement direction. The chosen scenery was a parking lot where rows of parked vehicles can be found on each side and a building can be found on one of the two sides of the road. The chosen target was a car which was driven around in various movements with respect to the host car.

Since LCA and BSD, as mentioned in Chapter 1 are possible applications for MRR corner radar, the list of tests that were performed were selected following the guidelines of the BS ISO 17387:2008: "Intelligent transport systems- Lane change decision aid systems (LCDAS)- Performance requirements and test procedures" [44].

These tests are a sequence of situations with the target which is either missing, approaching, or leaving (at different speeds or lane distances), and the host, which is either still or moving. The list of presented tests can be summarized with the following conditions:

- Static host, closing or opening target in an adjacent lane.

- Static host, closing or opening target in a non-adjacent lane.
- Static host, curving target (right).
- Static host, curving target (left).
- Dynamic host, closing target on the adjacent lane.

4.3.1 Static Host, Adjacent Lane

The first tests were performed emulating a scenario in which a car is overtaking on the adjacent lane of the host car. For these acquisitions, the host car was parked on the left side of the road.

The BS ISO 17387:2008 reports two cases to be evaluated for this scenario (reported in Fig. 4.14):

- The first case (Test 1) is summarized in Fig. 4.14a and is required to evaluate the detection of closing vehicles on an adjacent lane.
- The second case (Test 2) is summarized in Fig. 4.14b and is required to evaluate the detection of overtaking vehicles on an adjacent lane and the blind spot detection capability of the radar.

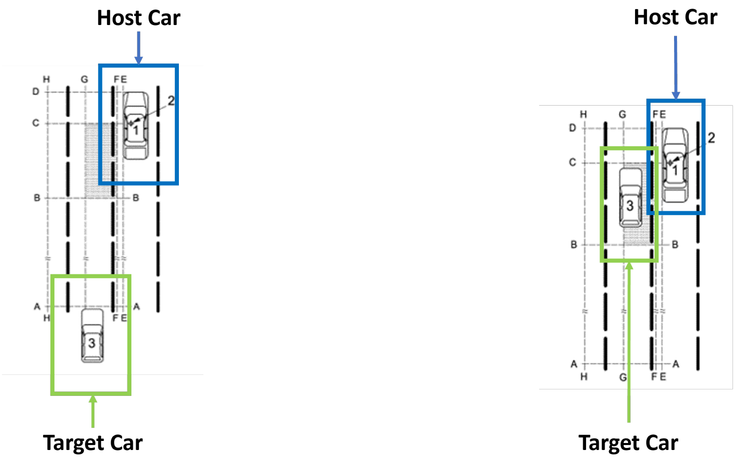

(a) Test to verify capability of closing vehicle detection

(b) Test to verify blind spot detection capability

Fig. 4.14 Static host, adjacent lane tests

For both Test 1 and Test 2 the target car was driven towards and away from the host car at different speeds.

The results for a sample test where the target car was driven at 30 km/h on a straight path and passed close to the host car (<2 m) are reported in Fig. 4.15a. A maximum range line (red line) at 75 m and two parallel lines spaced 3 m to represent two lanes were added (blue lines) in the picture. The radar started to detect the target car at the maximum range and tracked the target in the correct lane for the whole path. Fig. 4.15b shows a zoom of the same detection in the near range of the radar. The target was detected and tracked until it overtook the host car.

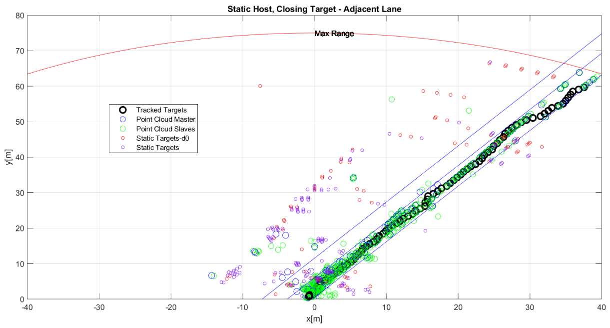

(a) Static Host, Closing Target, Adjacent lane

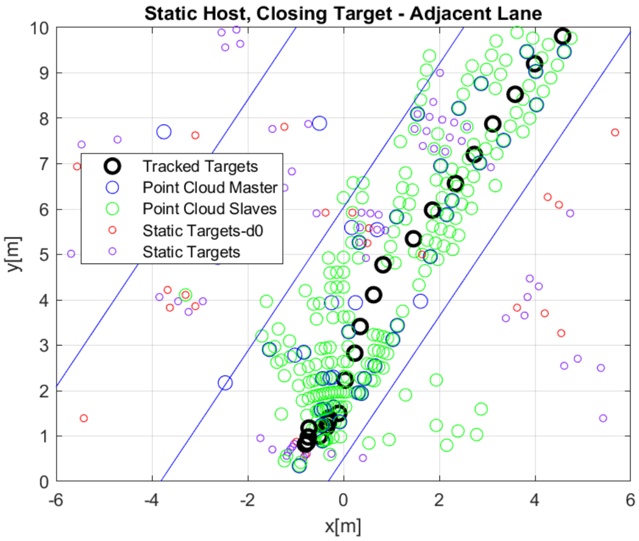

(b) Static Host, Closing Target (close range), Adjacent lane

Fig. 4.15 Result for Test 1 and 2

In Fig. 4.16 a surface plot of a range-Doppler Matrix acquisition with the closing target located at 72 m is reported. Cars have typical RCS which varies from 10-20 dB depending on models, distances, and angle of observation [45]. The target is detected with an SNR of 15 dB as shown from the highlighted peak. This value is in line with the expected one, obtained from eq. 2.7 (16 dB) taking into account the losses shown in the result of Fig. 4.6 and a target at 72 m range, and 32° (as in this test) with $\sigma_{dB} = 10\text{dB}$.

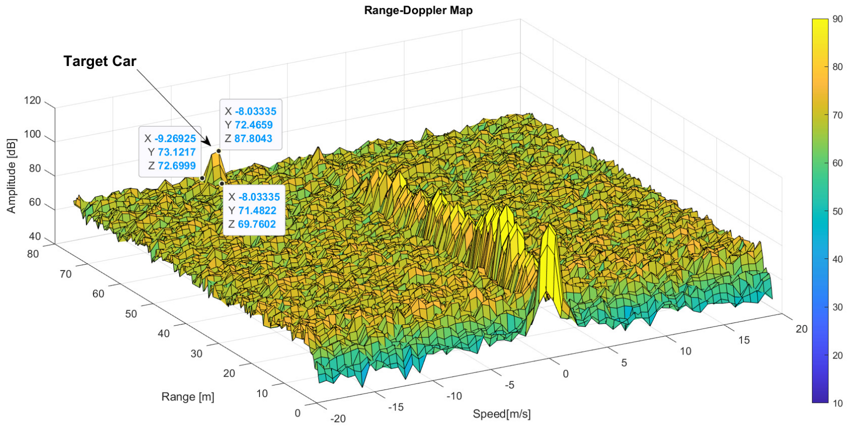

Fig. 4.16 Static Host, Closing Target (72 m), Adjacent lane, Range-Doppler Matrix

4.3.2 Static Host, non Adjacent Lane

The second set of tests was performed emulating a scenario in which a car is overtaking on a non-adjacent lane (distance >3 m) with respect to the host car. For these acquisitions, the host car was still parked on the left side of the road.

The BS ISO 17387:2008 test case for this scenario is summarized in Fig. 4.17. The test is necessary to evaluate the capability of the BSD system of detecting that a target is present in the non-adjacent lane and no warning needs to be activated.

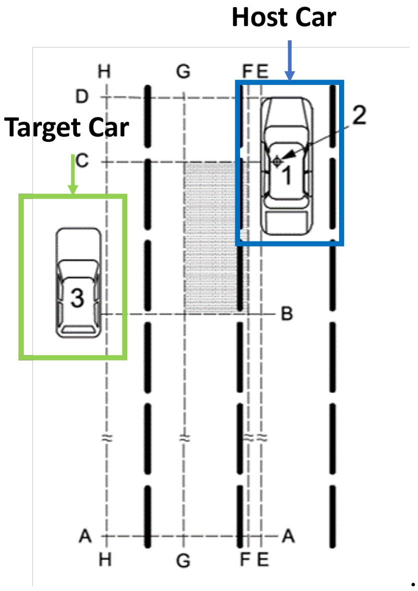

Fig. 4.17 Test to verify capability of detecting vehicles in non-adjacent lane

The results for a sample test where the target car was driven at 30 km/h on a straight path that pass at a distance from the host car corresponding to a non-adjacent lane is reported in Fig. 4.19. In the picture, a maximum range line (red line) at 75 m and two parallel lines spaced 3 m to represent two lanes have been added (blue lines). The radar started to detect the target car at the maximum range and tracked the target in the correct lane for the whole path. Fig. 4.19 shows a zoom of the same detection in the near range of the radar. The target was detected and tracked until it overtook the host car.

Fig. 4.18 Static Host, Closing Target (close range), non Adjacent lane

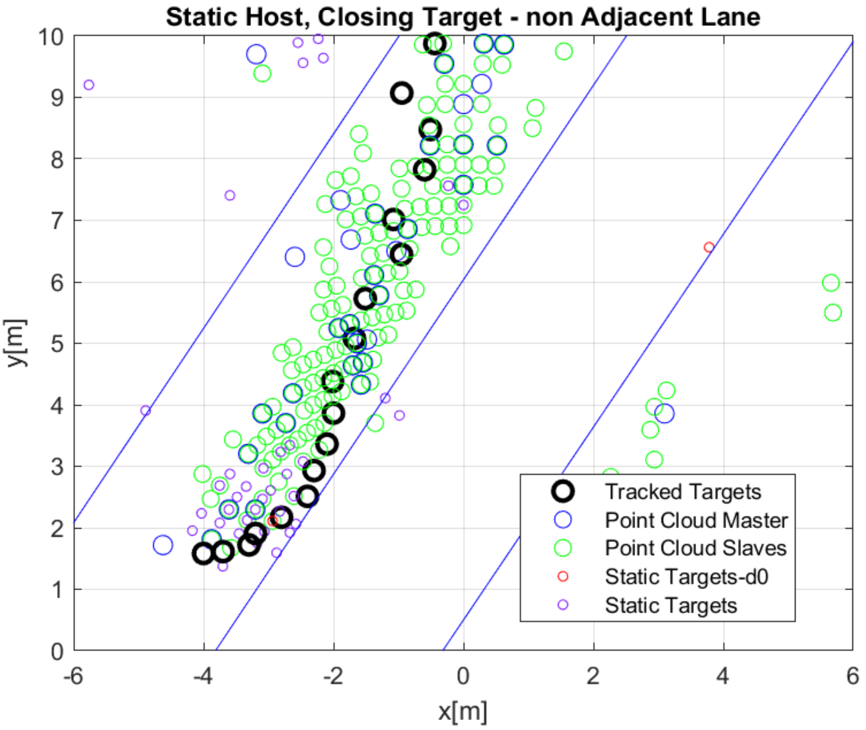

Fig. 4.19 Static Host, Closing Target, non Adjacent lane

4.3.3 Dynamic Host

A set of tests was performed in dynamic conditions with the Host car moving forward. For this acquisition the host car was driven on a straight line along the host's left side of the road, keeping the velocity as constant as possible. The host car was driven in the roadway scenery at different speeds. The target car was driven toward the host starting to move from variable ranges and at different speeds.

It was necessary to know the ego velocity to be able to separate dynamic targets from static ones. In order to do so the RANSAC algorithm presented in Chapter 3.8 was implemented on the AWR1843. The algorithm functionality was also verified during this set of tests by checking the estimated velocity with both the values from the car and the radar data and by checking correct identification of the static targets.

In Fig. 4.20 the results from a sample test where the host car was moving forward at around 12 km/h and the target car was overtaking at 30 km/h are reported. The yellow points highlight the straight path taken by the host car. The target car started moving when the host car was at a 50 m distance (not at the maximum detection range due to limit in the road length).

As in the static tests, also in the dynamic scenario, the car was tracked correctly for the whole path until it overtook the host car (the last frame of detection is reported in the figure).

Regarding the ego velocity estimation, all the parked cars, the building on the right, and the wall on the back of the host car are all identified as static targets and are not considered by the tracking algorithm.

The ego velocity estimated from the radar with the RANSAC algorithm during the test is reported in Fig. 4.21 (blue curve). After the first acceleration phase, the velocity oscillates around at the value of 12 km/h. Due to the nature of the detections, this value can oscillate slightly from one radar frame to the other. By applying a simple exponential forgetting average with forgetting factor k=0.1

$$EgoAvg_i = kEgoV + (1-k)EgoAvg_{i-1} \tag{4.2}$$

a more stabilized measurement representing the velocity of the host car can be obtained (red curve).

Another set of dynamic tests was performed to verify the capability of detecting improvised changes of behavior of the target car. For this purpose the target car was driven behind the host car (starting again at a range of 50 meters) at a higher velocity,

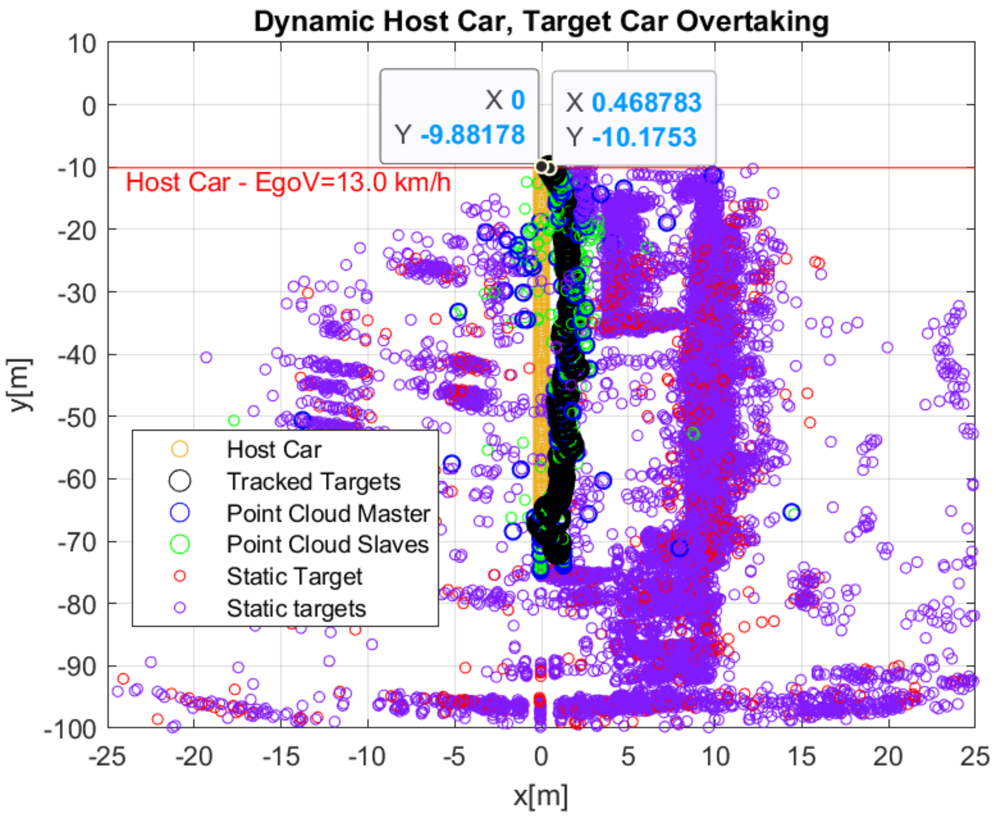

Fig. 4.20 Host car moving at 13 km/h, Target car overtaking at 30 km/h

then the target slowed down to the host car's velocity and, after following the host car at the same speed for a while the target car moved away simulating a turn (in a park or on another street).

In Fig. 4.22 the result of a sample test is reported. The target car is tracked correctly from the beginning to the end. The track was not lost when the car slowed down abruptly and the tracking algorithm followed the target car when it turned right to park.

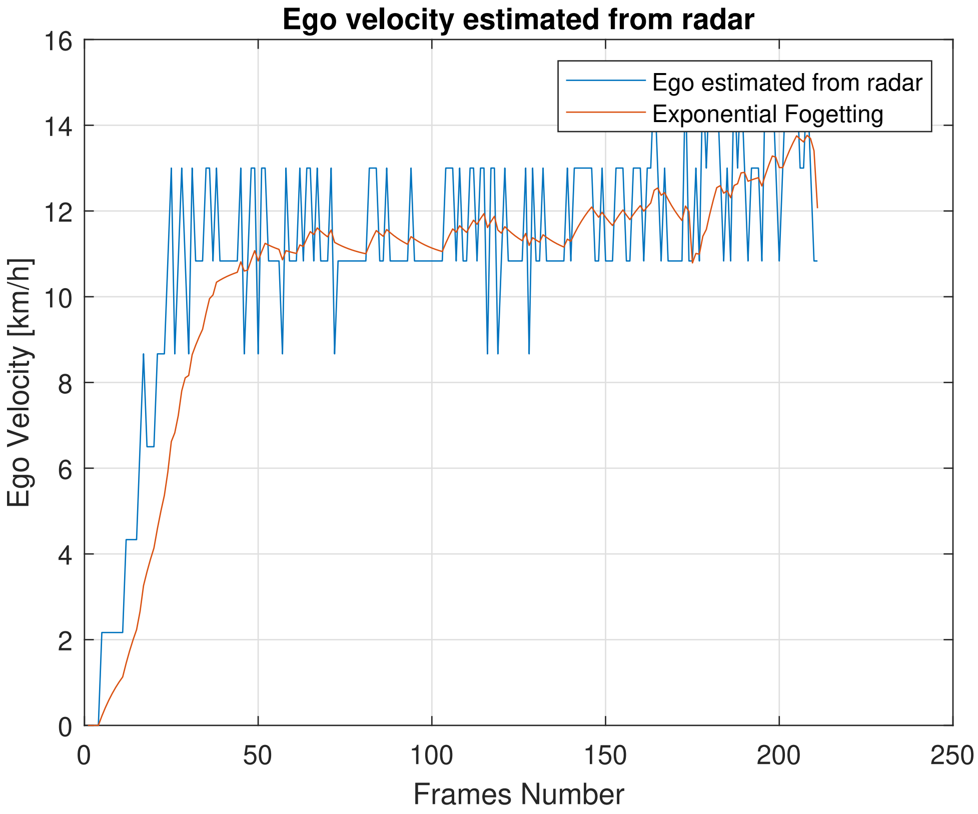

Fig. 4.21 Ego estimated from the radar during the test

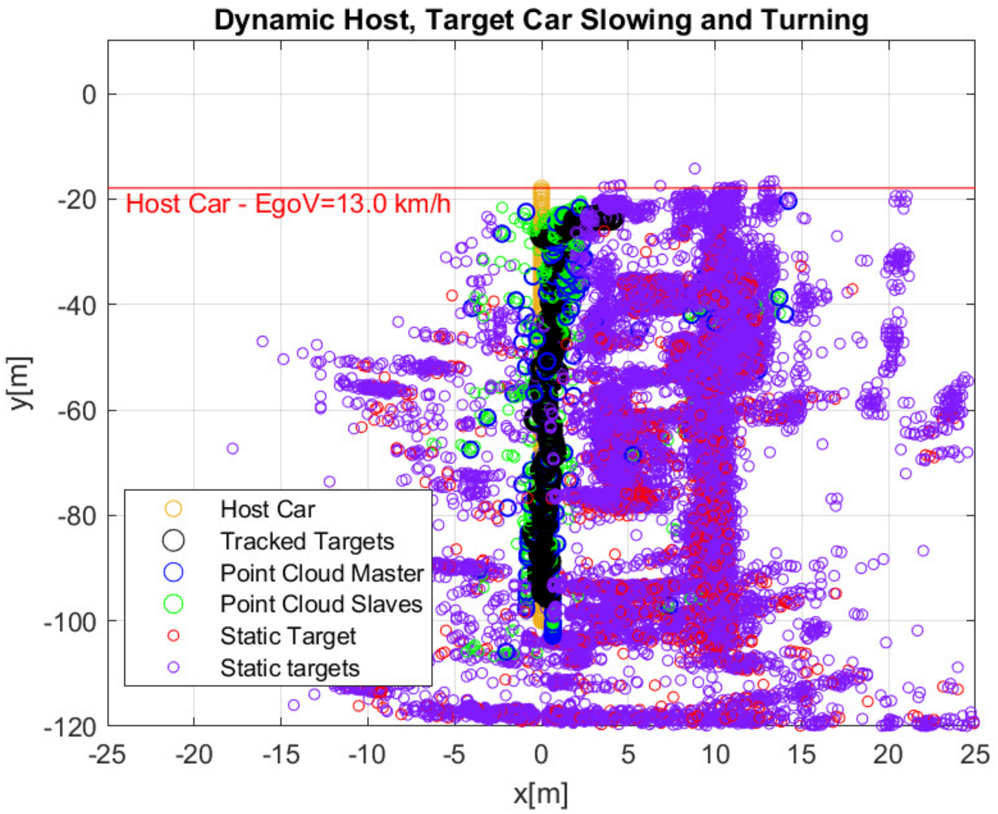

Fig. 4.22 Host car moving at 13 km/h, Target car closing at 30 km/h, slowing down and turning

4.3.4 Static Host, Curving Target Acquisition

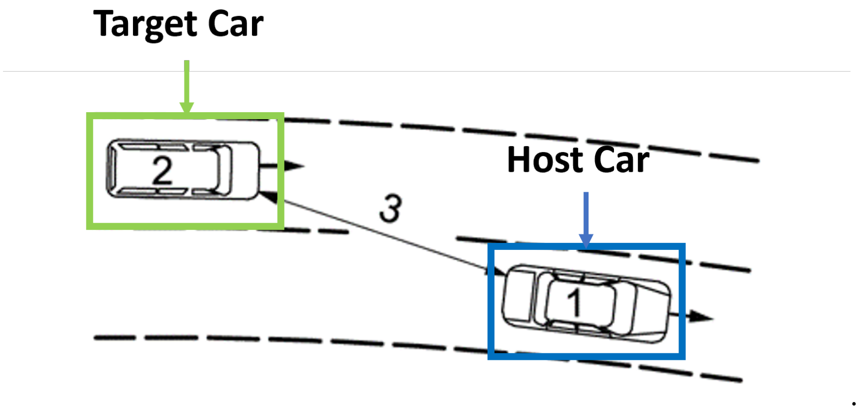

(a) Test to verify capability of detecting curving vehicles

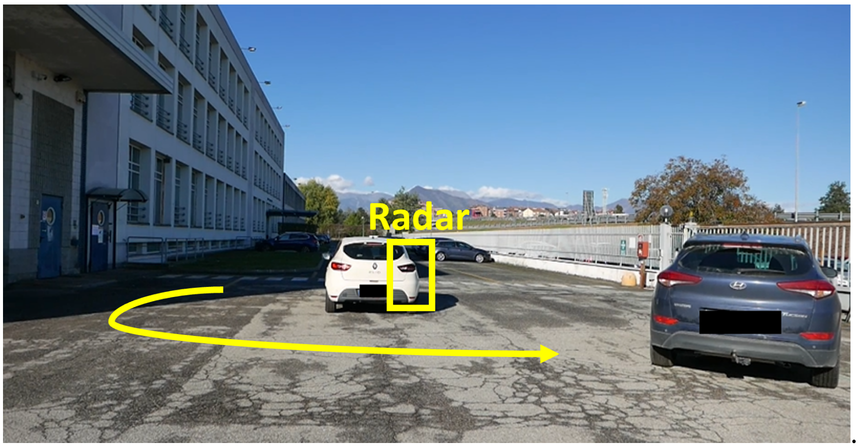

[redacted]

[redacted]

(b) Excerpt of a video of the test

Fig. 4.23 Static host, curving target acquisition

The capability of detecting and tracking targets while curving had also to be tested as shown in Fig. 4.23. Since the space in the parking lot was limited, for safety reasons, it was not possible to perform dynamic tests in this scenario. Static tests were performed with the host car parked in an area where the target car could maneuver around it. The target car curved around the car with a significantly smaller radius of curvature with respect to the minimum required in the BS ISO 17387:2008 for the slower listed vehicles (closing vehicles with v_{max} = 10 m/s, minimum radius for which performances must be granted R_{cmin}=125 m). The target car was driven at close range (at both adjacent and non-adjacent lane distances) overtaking it on the right side. An image of the described scenario is given in Fig. 4.23b.

In Fig. 4.24 the results for a sample test where the target car was curving behind the host car (from left to right) and overtaking at non-adjacent lane distance are shown. The radar data are rotated at an angle opposite to the radar installation angle to have them aligned with respect to the car axis. The target car was detected starting from $\theta_{car} = 40°$ (which is expected since the radar is pointing at $\theta_{car} = -35°$. The radar started to track the target car after a few frames starting from $\theta_{car} = 20°$ and then the tracking followed the car until overtook the host car in the non-adjacent lane.

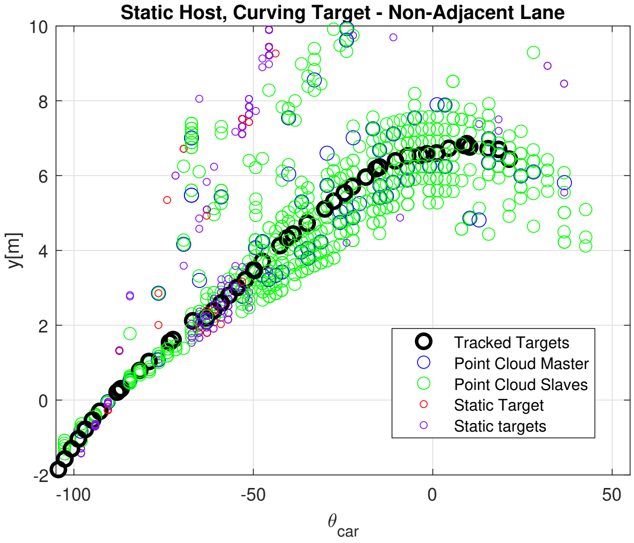

Fig. 4.24 Static host, curving target (left to right of host car) - non adjacent lane

Another sample test similar to the previous one is presented with the target car coming from the opposite direction of movement and turning behind the car (right to the left of the host car) at an adjacent lane distance. The result of the test is reported in Fig. 4.25: the target car detection started when it was still on the right side of the host car. The tracking started after a few frames at $\theta_{car} = -90°$; when the car was in the middle, due to the perpendicular movement with respect to the radar, for some frames the car was identified as a static target and, for this reason, the track was lost at $\theta_{car} = 20°$ instead of following the target car up to the last detection. In real installation, the track is followed by the radar installed in the other left rear lamp.

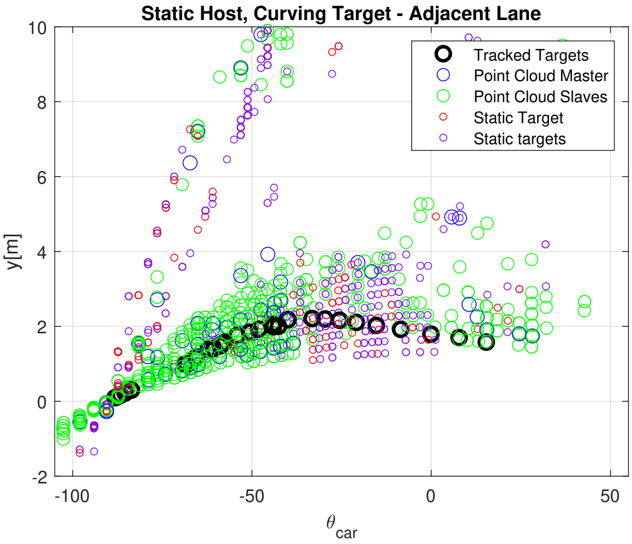

.

Fig. 4.25 Static Host, Curving Target (right to left of host car) - ADL

Chapter 5

More Effective Modulation Schemes

As mentioned in Chapter 1 the FMCW is the most diffused modulation scheme for automotive radars and it is favored by industry due to its several existing implementation solutions.

Due to its nature of sampling beat frequency signals, the FMCW technology exhibits range and Doppler coupling. Target velocity affects range estimations, as shown in eq.1.3, and high Doppler frequency variations can degrade performances. Fast slope chirps can mitigate this effect at the cost of increasing the sampling frequency.

Another drawback is that the typical TDM MIMO scheme to achieve N transmitted signals orthogonality tends to limit the maximum unambiguous velocity since $v_{\max} = \frac{\lambda}{4NT_c}$, where N is the number of transmitting elements. The ambiguous velocity can be recovered in different ways (as shown in Chapter 3.7 for example), but this usually comes with severe drawbacks (processing or hardware complexity).

In the future, each car will have multiple radars installed around the vehicles. The actual bandwidth available all around the world for automotive radar are the 76-77 GHz and 77-81 GHz bands. Therefore radar interference mitigation will be required to be able to operate in high-traffic scenarios.

For this reason, more effective modulation schemes are being studied to tackle some of the mentioned problems. Digital modulation such as Phase Modulated Continuous Wave (PMCW) and Orthogonal Frequency Division Multiplexing (OFDM), have interesting properties that may be exploited.

In this chapter, a comparison between the raw data of a 1 TX/1 RX laboratory-assembled binary PMCW radar and those of an FMCW radar is reported. For the binary PMCW radar, a prototype solution was assembled in our laboratory, using connectorized components and an FPGA for real-time processing. For the FMCW radar, an off-the-shelf development board, equipped with a Texas Instruments AWR1843 SoC, was adopted. Both firmware for radar processing were fully developed and implemented on the FPGA and on the SoC, while the software for data visualizations and post-processing was implemented on a laptop PC.

The radars' parameters and gains were tuned to have the same power budgets, and in such a way that the SNR comparison was not affected by the hardware. A test campaign was conducted, to analyze the range-Doppler responses of the two radars, with real data captured in defined real-world scenarios. For each scenario, the data were captured simultaneously, with the radars close to each other, and in the same conditions, to obtain consistent measurements. The results obtained for the two radars, presented by the author in [46], are compared at the end of this chapter.

5.1 PMCW

PMCW modulated waveform consists of periodically transmitting a certain number of sequences phase modulating a carrier frequency. By correlating the received demodulated signal and transmitted sequence the range of the targets is retrieved. Even if this modulated waveform is widely spread in communication and military radar applications, so far it has not been the main focus for automotive radars. The main reason is that, as opposed to an FMCW radar which samples the beat frequencies with a relatively low bandwidth (5–20 MHz typical for automotive applications), PMCW radar needs to sample the full bandwidth of the transmitted signal (1–2 GHz typical for automotive applications). For this reason, high rates of sampling and accurate ADCs are required. With the advancement in chip integration, giga-sample per second ADCs can now be easily adopted. Another issue to be properly considered is the ADC dynamic range that can be harmonized with logarithmic amplifiers, high processing gains [47], and leaking cancellation techniques [48] to drastically improve sensitivity.

The most common PMCW modulated waveform is the binary PMCW which consists of a certain number of sequences of binary symbols I_n (0,1) called chips with 0–π degree mapping of a carrier frequency. The transmitted sequence with a number of chips equal to N and a chip duration T_{ch} can be written as

$$s_{TX}(t) = \sum_{n=0}^{N-1} g(t - NT_{ch}) cos(2\pi f_0 t + I_n \pi) \tag{5.1}$$

where f_0 is the carrier frequency, I_n is the sequence element and g(t) is a gate function of unit amplitude in the interval [0, T_{ch}]. The received PMCW signal after a propagation delay $t_d = \frac{2R}{c}$ can be modeled as

$$s_{RX}(t) = A s_{TX}(t - t_d) exp(j2\pi f_d t). \tag{5.2}$$

The range response is directly derived by calculating the correlation between the demodulate I/Q signal and the sequence of binary symbols I_n. An FFT calculated per each range-bin along the different sequences extracts the Doppler-induced variations to measure the targets' radial velocity. Also for PMCW radars, a MIMO approach (not present in the system of this work) is possible for angle of arrival estimation.

The range resolution is $R_{res} = \frac{T_{ch} c}{2} = \frac{c}{2B}$ where the difference with FMCW radar is that the bandwidth is determined by the total duration of the chips.

Since PMCW radar relies on sampling a time signal, the maximum unambiguous range is limited, in the case of continuous transmission of the same sequence, by the duration of the sequence (T_s). Therefore, the maximum unambiguous range is $R_{max} = \frac{cT_s}{2}$ and it is independent of the bandwidth, providing greater flexibility in optimizing system parameters. In the case of continuous transmission of orthogonal codes, the unambiguous range can be extended.

An advantage derived from the signal nature of the PMCW is that range-Doppler estimation is not coupled as shown in Equation (5.2).

With PMCW modulated waveform, the adoption of orthogonal codes transmitted simultaneously by different antennas, it is possible to overcome the limitation of TDM and drastically improve the limit on the maximum velocity.

As opposed to FMCW which presents a sync-type function range compressed response when no window is applied, the autocorrelation of the PMCW sequences presents a thumbtack-like range response and sidelobes level can be significantly low with the right choice of the sequence enabling a much better High Contrast Resolution (HCR) performance. HCR is the radar ability to discriminate between small targets that are in close proximity to large targets, in range and angle [49]. Another advantage of PMCW radar is its ability to exploit Joint Communication and

Radar Sensing (JCRS), which is also useful for further mitigating mutual interference [50].

5.2 PMCW vs FMCW Real Data Comparison

5.2.1 FMCW Systems Description

For the FMCW radar the well-known AWR1843BOOST [51] evaluation board of the AWR1843 radar SoC from Texas Instruments was selected.

The FMCW SoC samples the I and Q beat frequency signals with the internal ADCs. Range and Doppler FFTs are performed on the I and Q sampled data by the DSP and are stored in memory as a range-Doppler matrix which is then sent through the KSZ8851SNL SPI-Ethernet converter to a laptop PC to be displayed on a user interface and stored for further analysis.

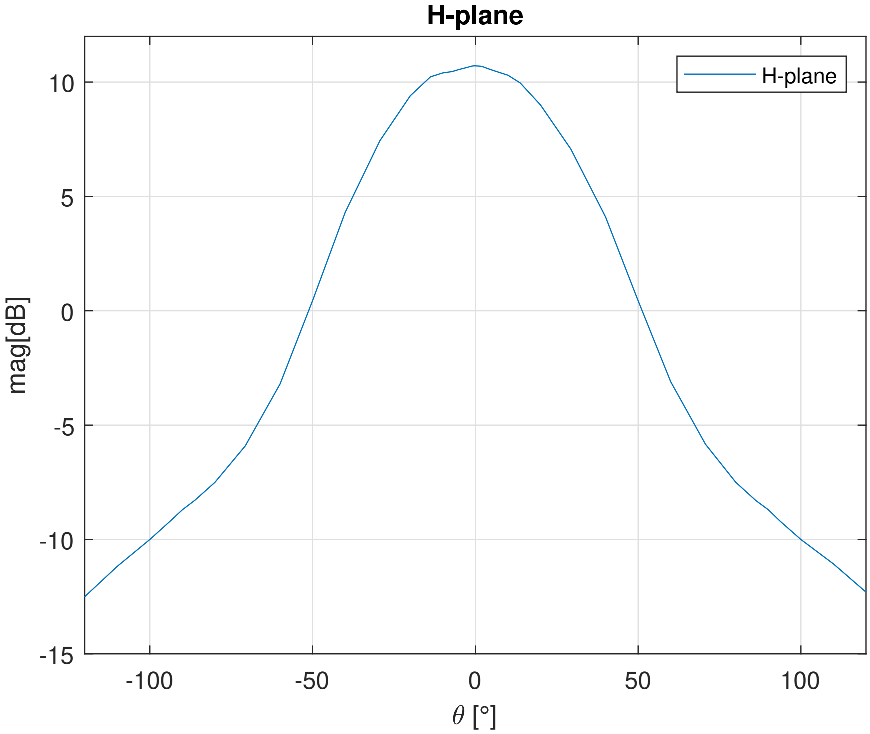

Fig. 5.1 H-plane radiation pattern of the AWR1843BOOST

The antennas printed on the AWR1843BOOST PCB are 3 elements vertical patch arrays with 10 dB gain at the design center frequency of 78 GHz. The calculated

H–plane (horizontal) and E–plane (vertical) radiation patterns at 78 GHz are shown in Fig. 5.1 and Fig. 5.2 respectively. The horizontal 3 dB beamwidth is ±28°, while the vertical 3 dB beamwidth is ±14°.

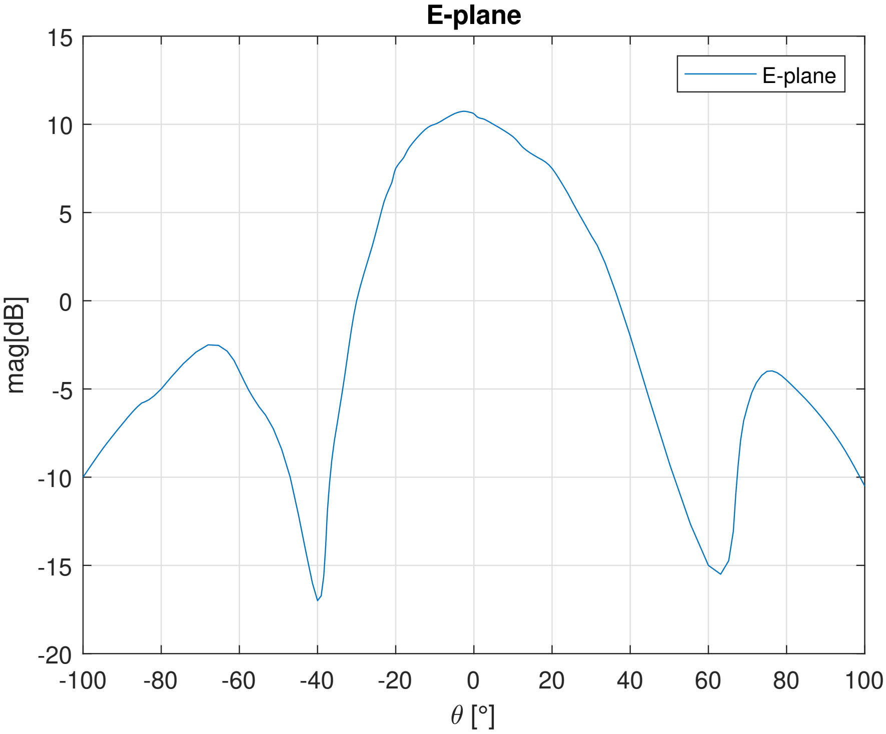

Fig. 5.2 E-plane radiation pattern of the AWR1843BOOST.

5.2.2 Binary PMCW Systems Description

For the binary PMCW radar, a customized solution with 1 TX channel and 1 RX channel was assembled. A block diagram of the prototype is shown in Fig. 5.3 while the manufactured prototype is shown in Fig. 5.4.

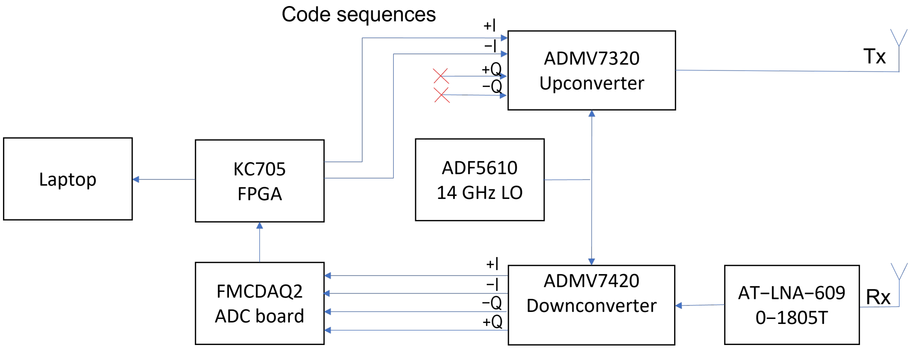

Fig. 5.3 Block diagram of the binary PMCW system assembled.

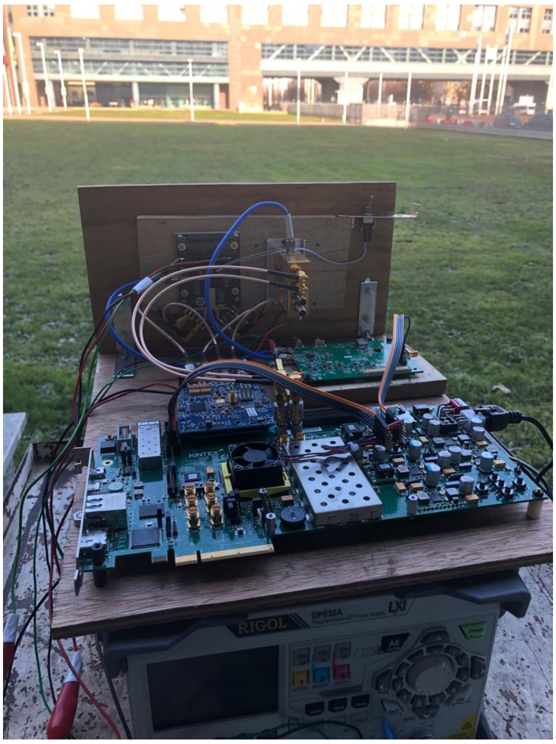

Fig. 5.4 Binary PMCW manufactured prototype.

The transmitter is constituted by the evaluation board of the ADMV7320 [52] 81–86 GHz band upconverter from Analog Devices with typical saturation power $Psat =$ 26 dBm. The receiver is constituted by the evaluation board of the ADMV7420 [53] 81–86 GHz low noise down converter from Analog Devices with baseband from DC to 2 GHz and a typical conversion gain of 10 dB. Between the receiving antenna and the ADM7420 evaluation board a Low Noise Amplifier (LNA), the

AT-LNA-6090-1805T [54] from ATMicrowave, is present with a typical gain of 18 dB.

The evaluation board with the ADF5610 [55] chip from Analog Devices generates a 14 GHz reference signal for both the upconverter and the downconverter which is then internally multiplied by a 6 × factor to obtain an 84 GHz carrier.

The binary PMCW modulating sequences are generated by the XC7K325T-2FFG900C FPGA hosted in the KC705 [56] development board from Xilinx. The sequences are translated into differential signals and sent to the in-phase upconverter input. The downconverted differential, I and Q, received signals are sampled by an AD9680 [57] chip hosted on a FMCDAQ2 board [58] from Analog Devices. The chip has 4 channels with 1 GSps and 14 bits precision and is connected to the FPGA through JESD204b [59] standard.

The FPGA receives the I and Q raw data sampled by the ADC, computes the correlations with the transmitted sequence for the range processing, and sends the outputs through Ethernet to a laptop PC. The laptop PC computes the Doppler FFT in real-time to obtain a range-Doppler matrix which is displayed and stored for further analysis.

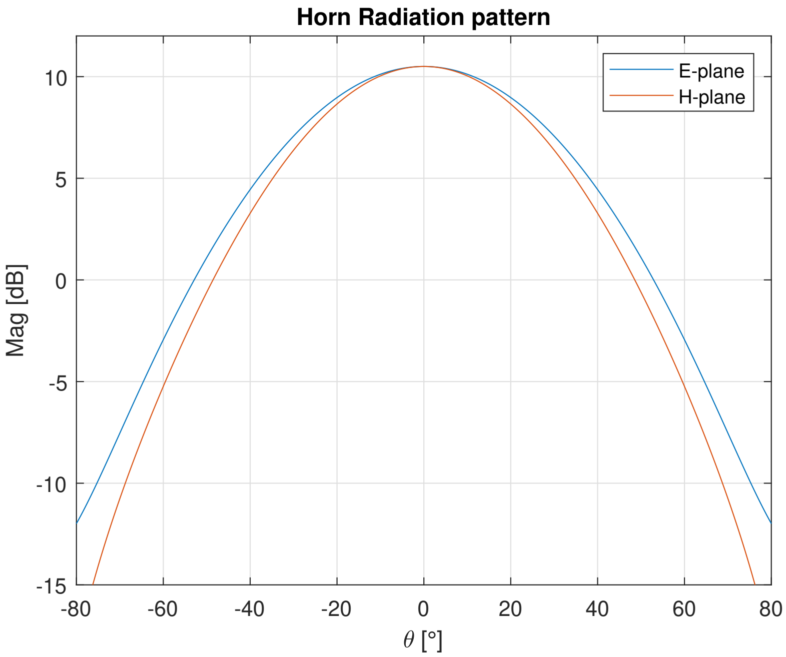

Fig. 5.5 E and H plane radiation patterns of the standard pyramidal horn.

The antennas for the TX and RX channels are equal standard pyramidal horns. The antenna dimensions are 4.2 mm × 3 mm × 20 mm and it has a 10.5 dB gain. The calculated H-plane (horizontal) and E-plane (vertical) radiation pattern at 84 GHz are shown in Fig. 5.5. The horizontal 3 dB beamwidth is ±20.5°, while the vertical 3 dB beamwidth is ±21°.

5.2.3 FMCW Radar Parameters Description

To achieve the comparison with the binary PMCW system only 1 TX and 1 RX were enabled on the AWR1843 chip during the tests.

The FMCW frame is composed of 64 chirps with a duration (T_c) of 50 μs, with a bandwidth (B) of 250 MHz, and with a frame repetition rate (F_r) of 100 ms. The range resolution is $\delta R = \frac{c}{2B} = 0.6$ m, where c is the speed of light. The number of samples of the range FFT for each chirp is equal to 256. Zero padding is performed to get 1024 range samples giving a range accuracy $R_{acc} = \frac{F_s}{2N_{FFT}S} = 15$ cm, where F_s is the sampling frequency equal to 7 MHz and S is the slope of the chirps. The chosen parameters bring to a maximum unambiguous range $R_{max} = \frac{F_s c T_c}{2B} \simeq 150$ m. The key parameters of the chirps and frame structure are reported in Table 5.1.

Table 5.1 Key radar parameters for the FMCW frame and chirps.

Symbol	**Description**	**Value**
B	Bandwidth	250 MHz
T_c	Chirp Duration	50 μs
S	Slope	6.85 MHz/s
N_{FFT}	Number of Range FFT Samples	1024
N	Number of Chirps per TX	64
F_s	Sampling Frequency	7 MHz
F_r	Frame Repetition Rate	100 ms
δR	Range Resolution	0.6 m
R_{acc}	Range Accuracy	0.15 m
R_{max}	Max Unambiguous Range	150 m
δv	Velocity Resolution	0.6 m/s
v_{max}	Max Unambiguous Velocity	19.2 m/s

5.2.4 Binary PMCW Complementary Code Sequences

The code sequences exploited by the binary PMCW modulation are Golay complementary sequences [60]. This types of code is formed by complementary pairs which satisfy the properties of having out-of-phase aperiodic auto-correlation coefficients sum equal to zero [61]. Let a $(a_0, a_1, a_2 ... a_N)$ be a sequence of length N with $a_i \in \{+1, -1\}$ and its complementary pair b $(b_0, b_1, b_2 ... b_N)$ with $b_i \in \{+1, -1\}$ and define the aperiodic auto-correlation function as

$$\rho_a(k) = \sum_{N=1}^{N-k-1} a_i a_{i+k},\ 0 \leq k \leq N-1. \tag{5.3}$$

For the Golay complementary pair we obtain,

$$\rho_a(k) + \rho_b(k) = 0, k \neq 0. \tag{5.4}$$

This property is such that the sum of the responses of the complementary pair, transmitted one after the other, cancels out the sidelobes and doubles the peaks, resulting in a 2 × improvement in SNR and nulling of the range sidelobes.

The sequences are generated through recursive construction. To generate the next code the previous code is concatenated to its complement. To generate the complement code the previous code is concatenated to the inverse of the previous code [62] as shown in Table 5.2.

Table 5.2 Golay complementary sequences construction.

Code Length	**Code**	**Complement**
2^1	α	β
2^2	$\alpha\beta$	$\alpha\overline{\beta}$
2^3	$\alpha\beta\alpha\overline{\beta}$	$\alpha\beta\overline{\alpha}\beta$
...	...	...
2^N	$code_{N-1}compl_{N-1}$	$code_{N-1}\overline{compl}_{N-1}$

5.2.5 Binary PMCW Radar Parameters Description

The binary PMCW system generates Golay complementary sequences to modulate a carrier to be transmitted. On the receiver side, after downconversion, the I and Q signals are sampled. For each complementary sequence pair the correlation for a certain number (N_d) of delays (τ) between the transmitted sequence (a and its complementary b) and the received I and Q signal (a_{RX} and its complementary b_{RX}) is performed. The results are summed yielding a range response $R_{ab}(\tau)$

$$R_{ab}(\tau) = \sum_{i=1}^{i=N_d} a(t)a_{RX}(t+i\tau) + \sum_{i=1}^{i=N_d} b(t)b_{RX}(t+i\tau). \tag{5.5}$$

For each range bin a Doppler FFT is calculated obtaining a range-Doppler matrix.

The binary PMCW frame is composed of 128 complementary sequences (64 pairs). Each sequence has 256 chips with a duration of 4 ns with a bandwidth of 250 MHz. Also in this case, the range resolution depends on the bandwidth and is equivalent to the FMCW range resolution $\delta R = 0.6$ m. The range accuracy depends on the ADC sampling frequency (F_s). Since $F_s = 1$ GHz we obtain $\tau = 1$ ns and $Racc = \frac{\tau c}{2} = 0.15$ m. The a and b complementary sequences are transmitted continuously while, between the start of each pair, there is a 50 μs blank time interval to obtain the same maximum velocity of the FMCW radar. The frame repetition rate as for the FMCW is equal to 100 ms.

The key parameters of the sequences and frame structure are reported in Table 5.3.

Table 5.3 Key radar parameters for the binary PMCW frame and sequences.

Symbol	**Description**	**Value**
B	Bandwidth	250 MHz
T_ch	Chip Duration	4 ns
N	Number of Chips in a Sequence	256
N_p	Number of Complementary Pairs	64
F_s	Sampling Frequency	1 GHz
F_r	Frame Repetition Rate	100 ms
δR	Range Resolution	0.6 m
R_{acc}	Range Accuracy	0.15 m
δv	Velocity Resolution	0.6 m/s
v_{max}	Max Unambiguous Velocity	19.2 m/s

5.2.6 Power Budget Analysis

To accurately compare the results, it was important to ensure that the power budget of the two radars was the same so that the SNR was not affected by the hardware. Since the duration of the transmitted signal differed between the two radars, this needed to be considered when calculating the power budget. For this reason, the binary PMCW system transmitter gain was set to obtain an output power $PTX_P = 22$ dBm and the FMCW transmitter output power was set to be $PTX_F = 10$ dBm. Since the gain of the transmitting antennas, the number of complementary sequence pairs, and the number of chirps were the same, the effect to be considered in the power budget for the different transmitted signal durations (GTX_t) was given by the ratio of the effective sampled time of a chirp ($T_{cs} = N_{ADC}/F_S = 35\ \mu$s) and the time duration of a complementary pair $T_s = 2NTch = 2\ \mu$s,

$$GTX_t = 10\log_{10}(\frac{T_{cs}}{T_s}) = 10\log_{10}(\frac{35\mu s}{2\mu s}) = 12dB. \tag{5.6}$$

With these settings, the relative power ratio (R_r) between the two systems was 0 dB,

$$R_r = \frac{PTX_P+GTX_{ant}}{PTX_F+GTX_{ant}+GTX_t} = \frac{22\ dBm+10\ dB}{10\ dBm+10\ dB+12\ dB} = 0\ dB. \tag{5.7}$$

On the receiver side, the gains were set to achieve the same received signal strength and to comply with a dynamic range of the ADC in both systems. In this way, the binary PMCW system LNA gain (G_{LNA}) together with the downconversion gain (G_{dc}) achieved the same gain value of the FMCW internal LNA of the AWR1843:

$$\begin{aligned} GRX_P = GRX_{ant} + G_{LNA} + G_{dc} = 10\ dB + 18\ dB + 10\ dB = 38\ dB \\ GRX_F = GRX_{ant} + GRX_{ch} = 10\ dB + 28\ dB = 38\ dB. \end{aligned} \tag{5.8}$$

5.3 Testing and Results

The two radar systems were tested simultaneously in an open grass field next to each other to capture the results from the same real-world scenario. The two radars are shown in Fig. 5.6. On the left side, the two standard horn antennas of the binary PMCW radar are visible on a wooden tile supporting the RF modules on the other side. On the right side, the AWR1843BOOST evaluation board is clearly visible on the little wall.

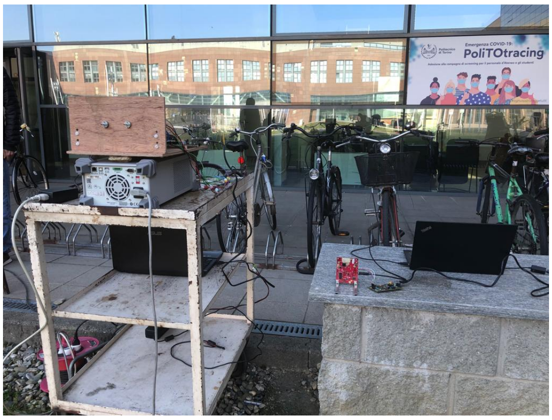

Fig. 5.6 Tests set-up.

As a first test, a 10 dBsm RCS corner reflector was positioned at the boresight of the two radars at a 12 m distance. The measured range-Doppler matrices (on top) and the range responses (on bottom) of a few consecutive frames are shown in Fig. 5.7. In the range response of the FMCW radar (Fig. 5.7b) the typical -13 dB sidelobes of the peak can be observed. Instead, thanks to the Golay complementary sequences the sidelobes were practically cancelled out in the PMCW response (Fig. 5.7a). To evaluate the effects of typical windowing, a Blackman window [35] with the frequency response parameters of Table 5.4 was applied (as shown in Fig. 5.7c) to the range FFT inputs of the FMCW radar to reduce the sidelobes. While the sidelobes were effectively reduced, as a drawback the peak width doubled and the maximum peak was reduced of 3 dB.

Table 5.4 Blackman window frequency response parameters.

Description	**Value**
Max peak attenuation	3 dB
Sidelobes suppression	35 dB
Peak widening factor	2

A test to verify the HCR capability of both technologies was performed by walking aside the corner reflector. Fig. 5.8 shows the measured range-Doppler matrices (on top) and the range responses (on bottom) of a few consecutive frames when the pedestrian was positioned near the corner reflector at a relative distance of 0.6 m. The binary PMCW radar (Fig. 5.8a) clearly separated the two targets presenting 15 dB difference in RCS (pedestrian typical $RCS = -5$ dBsm [63]) and

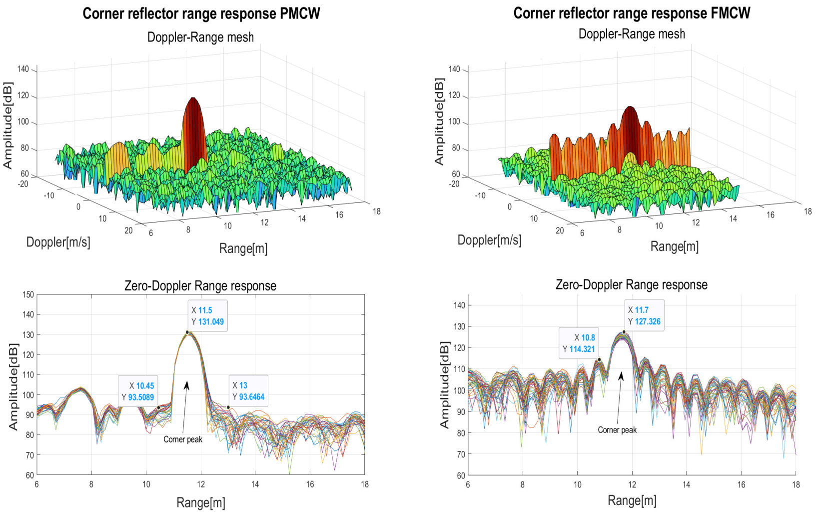

(a) PMCW

(b) FMCW

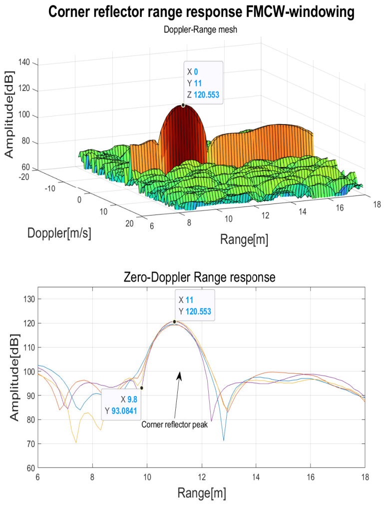

(c) FMCW-windowing

Fig. 5.7 10$dBsm$ Corner reflector range response

corner reflector $RCS = 10$ dBsm). The range resolution $\delta R = 0.6$ m limited further separation. For the FMCW radar (Fig.5.8b), despite having the same resolution δR=0.6 m, the sidelobes range response of the corner reflector did not allow to separate the two targets. When Blackman windowing was applied to the range FFT inputs of the FMCW radar, despite the mitigation of sidelobes, due to the doubling of the peak width, only a slight deformation was observable which was not sufficient to separate the two targets (Fig. 5.8c).

The test results showed that the minimum distance at which the FMCW radar could separate the two targets was $\Delta R \geq 1.2$ m even if the resolution was lower. In Fig. 5.9 the results of the test when the pedestrian and the corner reflector are at $\Delta R = 1.2$ m are reported. Also in this case the binary PMCW radar (Fig.5.9a) showed better performances separating clearly the two targets. The FMCW radar (Fig. 5.9b) could barely separate the two targets but the detection was severely affected by the sidelobes. The FMCW radar with Blackman window (Fig. 5.9c) could reveal the small target but with a significantly worse SNR compared to the binary PMCW radar.

The behavior of the two radars with moving targets was compared by detecting a walking pedestrian in front of the two radars. The pedestrian walked straight away from the radars, at their boresights, at about 1.2 m/s, without changing speed and direction. In Fig. 5.10, the range responses containing the maximum Doppler peak for each frame are reported, the two radars presented identical performances and SNR as expected. In the AWR1843 RX chain, two first-order internal high-pass filters are applied to the analog beat frequency signal. This filtering improves the range dynamics attenuating strong RCS targets in close proximity of the radar. The two filters were set to the lowest possible cut-off frequencies equal to 175 kHz and 350 kHz.

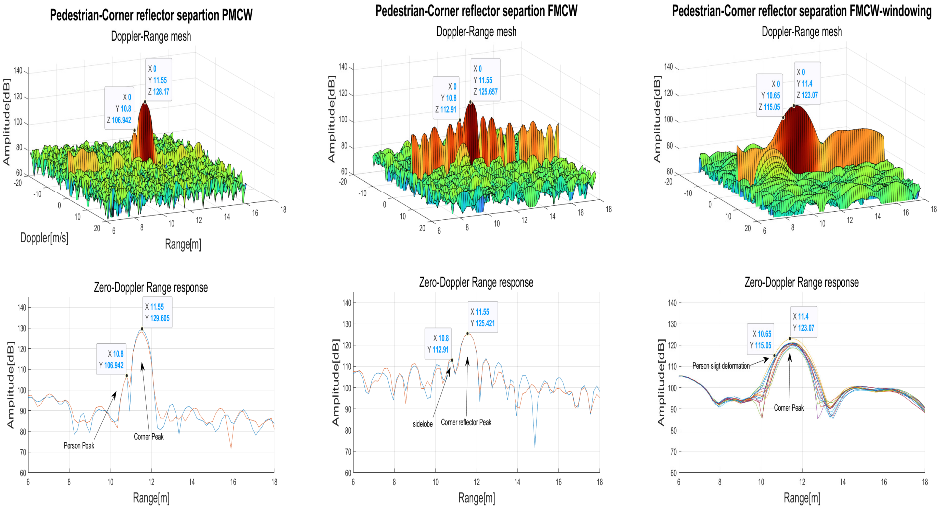

(a) PMCW (b) FMCW (c) FMCW with windowing

Fig. 5.8 Separation of a pedestrian near to a corner reflector $\Delta R = 0.6m$

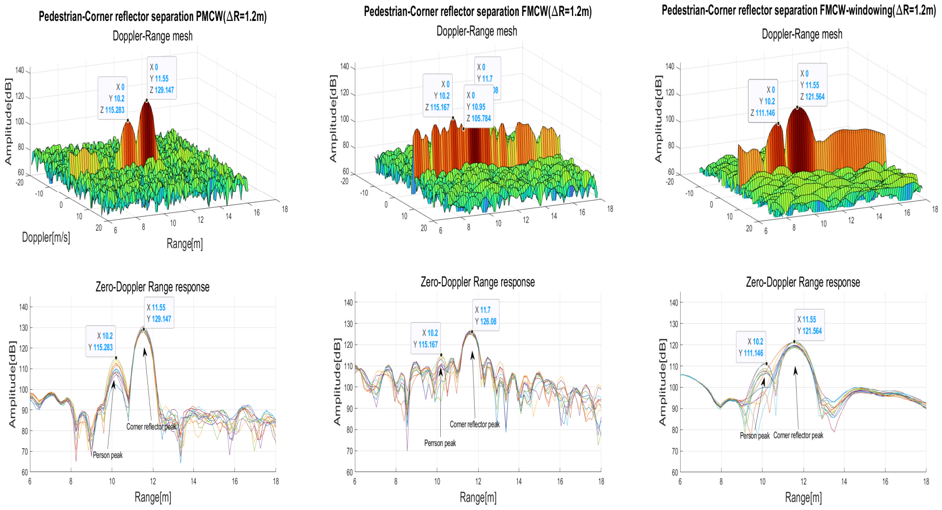

(a) PMCW (b) FMCW (c) FMCW with windowing

Fig. 5.9 Separation of a pedestrian near to a corner reflector $\Delta R = 1.2m$

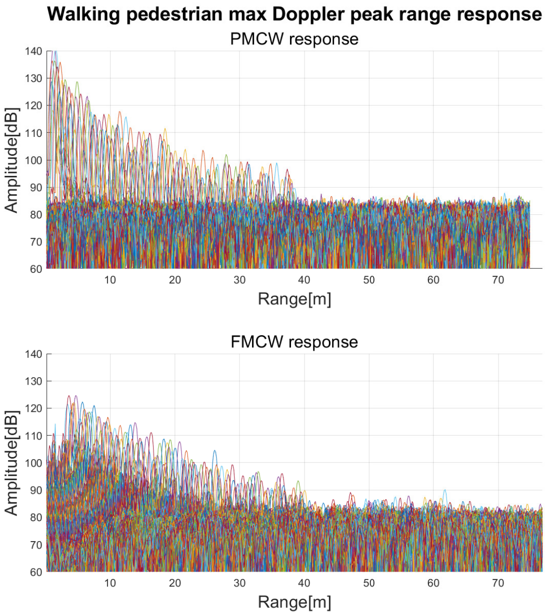

Fig. 5.10 Maximum Doppler peaks of a walking pedestrian for each range.

Tests to compare the Doppler responses were also performed moving a corner reflector toward and away from the radars. In Fig. 5.11 the Doppler and range cut of the range-Doppler matrix for the position of the moving target are reported. Behavior of the Doppler response was identical for the two radars, as expected.

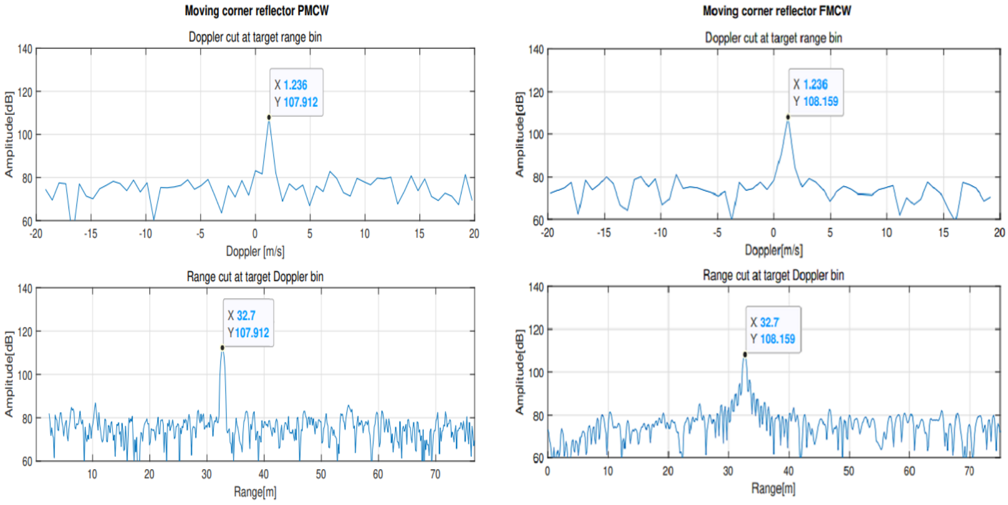

(a) PMCW (b) FMCW

Fig. 5.11 10 dBsm Moving corner reflector Doppler and range cuts.

5.4 Conclusions on the PMCW vs FMCW performances

A comparison of measured data in real-world scenarios, from a radar based on the currently most popular modulated waveform for automotive radar applications, the FMCW, and from a radar based on its main competitor modulated waveform, the binary PMCW was presented. Tests were performed on a grass field with an off the shelf FMCW radar and an assembled prototype binary PMCW radar in the same perfect conditions. The binary PMCW radar exploited Golay complementary sequences.

The binary PMCW modulated waveform enabled a reduction in the sidelobe levels and a drastically improved HCR capability. The results of the tests showed that the two modulated waveforms have identical performances in the Doppler response. Binary PMCW radars have some intrinsic advantages such as no range-Doppler coupling, shorter transmission time allowing for more transmitting antennas or larger unambiguous velocity, and natural integration of communication and sensing. The only trade-off required to gain all these advantages is the use of higher sampling frequency ADCs that must be integrated into the binary PMCW radar chip.

The presented analysis demonstrates that the binary PMCW radar should be considered in the next generation of automotive radars.

Chapter 6

Conclusions

Radar sensors are commonly installed as black boxes behind bumpers. In this thesis, it was shown that the full integration of an automotive FMCW-MIMO 77-81 GHz radar sensor into a rear lamp is possible following the described approach. This solution offers various benefits in terms of performance, increased protection, and improved installation convenience. The radar installed into the rear lamp was successfully prototyped and tested. The materials of the lamp were optimized to reduce reflections and improve the SNR of the received signals.

Preliminary temperature tests required by automotive standards were performed with the radar operating inside the lamp. The results suggest that the heat distribution of the board can be acceptable.

To assess performance, static tests were conducted both in an open field and on the road. Optimal results for the detection and tracking of vehicles and bicycles were obtained up to 75 m range.

A dynamic test campaign following ISO guidelines for blind spot detection has been carried out with the radar installed on a car. The ego velocity was estimated through radar data statistics, and the capability of the radar to separate ego targets from moving ones and to track targets optimally when the car is moving was tested.

Finally, a preliminary analysis of newer and more efficient modulations for radars to address some of the issues associated with conventional FMCW was presented. The real-world data comparison has shown excellent results regarding the Binary PMCW modulation.

Future works will focus on the analysis of high- performance waveguide antennas for automotive radar since traditional automotive on-board printed antennas are currently a limiting factor due to high propagation losses in the PCB materials. An investigation into other potential smart radar integrations for automotive applications (rear mirror, front lamp, etc..) or various other fields will be conducted. An analysis of new integrated radars, exploiting PMCW modulation to enhance radar performances, improve interference mitigation, and enable JCRS will be performed.

References

[1] C. Waldschmidt, J. Hasch, and W. Menzel, “Automotive radar — from first efforts to future systems,” IEEE Journal of Microwaves, vol. 1, no. 1, pp. 135–148, 2021.

[2] S. Roehr, P. Gulden, and M. Vossiek, “Precise distance and velocity measurement for real time locating in multipath environments using a frequency-modulated continuous-wave secondary radar approach,” IEEE Transactions on Microwave Theory and Techniques, vol. 56, no. 10, pp. 2329–2339, 2008.

[3] C. Sturm and W. Wiesbeck, “Waveform design and signal processing aspects for fusion of wireless communications and radar sensing,” Proceedings of the IEEE, vol. 99, no. 7, pp. 1236–1259, 2011.

[4] A. Bourdoux, U. Ahmad, D. Guermandi, S. Brebels, A. Dewilde, and W. V. Thillo, “Pmcw waveform and mimo technique for a 79 ghz cmos automotive radar,” 2016 IEEE Radar Conference (RadarConf), pp. 1–5, 2016.

[5] K. V. Mishra, M. Bhavani Shankar, V. Koivunen, B. Ottersten, and S. A. Vorobyov, “Toward millimeter-wave joint radar communications: A signal processing perspective,” IEEE Signal Processing Magazine, vol. 36, no. 5, pp. 100–114, 2019.

[6] J. A. Zhang, F. Liu, C. Masouros, R. W. Heath, Z. Feng, L. Zheng, and A. Petropulu, “An overview of signal processing techniques for joint communication and radar sensing,” IEEE Journal of Selected Topics in Signal Processing, vol. 15, no. 6, pp. 1295–1315, 2021.

[7] G. K. Carvajal, M. F. Keskin, C. Aydogdu, O. Eriksson, H. Herbertsson, H. Hellsten, E. Nilsson, M. Rydström, K. Vänas, and H. Wymeersch, “Comparison of automotive fmcw and ofdm radar under interference,” in 2020 IEEE Radar Conference (RadarConf20), 2020, pp. 1–6.

[8] M. Caffa, F. Biletta, and R. Maggiora, “Binary-phase vs. frequency modulated radar measured performances for automotive applications,” Sensors, vol. 23, no. 11, 2023. [Online]. Available: https://www.mdpi.com/1424-8220/23/11/5271

[9] M. Bauduin and A. Bourdoux, “Code diversity for range sidelobe attenuation in pmcw and ofdm radars,” in 2021 IEEE Radar Conference (RadarConf21), 2021, pp. 1–5.

[10] J. Hasch, E. Topak, R. Schnabel, T. Zwick, R. Weigel, and C. Waldschmidt, "Millimeter-wave technology for automotive radar sensors in the 77 ghz frequency band," IEEE Transactions on Microwave Theory and Techniques, vol. 60, no. 3, pp. 845–860, 2012.

[11] D. Bliss and K. Forsythe, "Multiple-input multiple-output (MIMO) radar and imaging: degrees of freedom and resolution," in The Thirty-Seventh Asilomar Conference on Signals, Systems Computers, 2003, vol. 1, 2003, pp. 54–59 Vol.1.

[12] C. Pfeffer, R. Feger, C. Wagner, and A. Stelzer, "Fmcw mimo radar system for frequency-division multiple tx-beamforming," IEEE Transactions on Microwave Theory and Techniques, vol. 61, no. 12, pp. 4262–4274, 2013.

[13] S. Sun, A. P. Petropulu, and H. V. Poor, "Mimo radar for advanced driver-assistance systems and autonomous driving: Advantages and challenges," IEEE Signal Processing Magazine, vol. 37, no. 4, pp. 98–117, 2020.

[14] "Arbe robotics radar page," (Accessed on 08/08/2023). [Online]. Available: https://arberobotics.com/perception-radar

[15] "Uhnder s80 chip pmcw automotive band radar," (Accessed on 08/08/2023). [Online]. Available: https://www.uhnder.com/images/data/S80_PTB_Rev1.0_May_5_2022_.pdf

[16] "Vayyar 79 ghz radar page," (Accessed on 08/08/2023). [Online]. Available: https://vayyar.com/auto/technology/79ghz/

[17] M. Gottinger, M. Hoffmann, M. Christmann, M. Schütz, F. Kirsch, P. Gulden, and M. Vossiek, "Coherent automotive radar networks: The next generation of radar-based imaging and mapping," IEEE Journal of Microwaves, vol. 1, no. 1, pp. 149–163, 2021.

[18] A. Correas-Serrano, M. Gonzalez-Huici, R. Simoni, T. Bredderman, E. Warsitz, T. Müller, and O. Kirsch, "Performance analysis and design of a distributed radar network for automotive application," in 2022 23rd International Radar Symposium (IRS), 2022, pp. 30–35.

[19] R. Schnabel, D. Mittelstrab, T. Binzer, C. Waldschmidt, and R. Weigel, "Reflection, refraction, and self-jamming," IEEE Microwave Magazine, vol. 13, no. 3, pp. 107–117, 2012.

[20] J. C. Dash, M. Parikh, N. Modi, J. Mukherjee, S. VR, T. SaiDeepak, and V. Dhoot, "Performance evaluation of automotive radar in the presence of bumper with multiple paint layers using bidirectional loss model," in 2021 15th European Conference on Antennas and Propagation (EuCAP), 2021, pp. 1–5.

[21] F. Norouzian, E. Marchetti, E. G. Hoare, M. Gashinova, C. C. Constantinou, P. Gardner, and M. Cherniakov, "Experimental study on low-thz automotive radar signal attenuation during snowfall," IET Radar, Sonar & Navigation, 2019.

[22] S. Hamid, D. Heberling, M. Junghähnel, T. Preussner, P. Gretzki, L. Pongratz, C. Hördemann, and A. Gillner, “Optically transparent antenna integrated inside a headlamp for automotive radar application,” in 2020 14th European Conference on Antennas and Propagation (EuCAP), 2020, pp. 1–5.

[23] N. Y. K. K. W. Yamamura, “Millimeter wave radar-equipped headlamp,” 2014, uS Patent: US8803728B2.

[24] “Texas instrument site, awr1843 product page.” [Online]. Available: https://www.ti.com/product/AWR1843

[25] “Microchip site , ksz8851snl-eval product page,” (Accessed on 20/12/2021). [Online]. Available: https://www.microchip.com/en-us/development-tool/KSZ8851SNL-EVAL

[26] “Maxim integrated,” (Accessed on 09/01/2022). [Online]. Available: https://www.maximintegrated.com/en/products/power/switching-regulators/MAX15062.html

[27] “Texas instruments site, tps7a53-q1 product page.” [Online]. Available: https://www.ti.com/product/TPS7A53-Q1

[28] “Aec council site,” (Accessed on 10/02/2022). [Online]. Available: http://www.aecouncil.com

[29] “Macronix site , mx25v1635l product page,” (Accessed on 23/12/2021). [Online]. Available: https://www.mxic.com.tw/en-us/products/NOR-Flash/Serial-NOR-Flash/Pages/spec.aspx?p=MX25V1635F&m=Serial+NOR+Flash&n=PM2257

[30] “ROGERS Corporation Site, RO4835 Laminates Page,” (Accessed on 25/09/2021). [Online]. Available: https://rogerscorp.com/advanced-electronics-solutions/ro4000-series-laminates/ro4835-laminates

[31] M. Caffa, S. Bottigliero, F. Ramonda, L. Gioanola, and R. Maggiora, “Integrated design and prototyping of a 77 ghz automotive medium range radar into car rear lamp,” IEEE Transactions on Vehicular Technology, pp. 1–10, 2023.

[32] “Lm63635 product page,” accessed on 15/10/2022. [Online]. Available: https://www.ti.com/product/LM63635-Q1

[33] C.-Y. Chen and P. P. Vaidyanathan, “Minimum redundancy mimo radars,” in 2008 IEEE International Symposium on Circuits and Systems (ISCAS), 2008, pp. 45–48.

[34] A. Moffet, “Minimum-redundancy linear arrays,” IEEE Transactions on Antennas and Propagation, vol. 16, no. 2, pp. 172–175, 1968.

[35] A. W. Oppenheim, Discrete- time signal processing / Alan W. Oppenheim, Ronald W. Schafer, ser. Prentice- Hall signal processing series. Englewood Cliffs: Prentice-Hall, 1989.

[36] J. Bechter, F. Roos, and C. Waldschmidt, “Compensation of motion-induced phase errors in TDM MIMO radars,” IEEE Microwave and Wireless Components Letters, vol. 27, no. 12, pp. 1164–1166, 2017.

[37] F. D. A. García, A. S. Guerreiro, G. R. d. L. Tejerina, J. C. S. S. Filho, G. Fraidenraich, and M. D. Yacoub, “Doppler estimation for high-velocity targets using subpulse processing and the classic chinese remainder theorem,” 2021, (Accessed on 12/10/2021). [Online]. Available: https://arxiv.org/abs/2101.11311

[38] B. Silva and G. Fraidenraich, “Performance analysis of the classic and robust chinese remainder theorems in pulsed doppler radars,” IEEE Transactions on Signal Processing, vol. 66, no. 18, pp. 4898–4903, 2018.

[39] D. Kellner, M. Barjenbruch, J. Klappstein, J. Dickmann, and K. Dietmayer, “Instantaneous ego-motion estimation using doppler radar,” in 16th International IEEE Conference on Intelligent Transportation Systems (ITSC 2013), 2013, pp. 869–874.

[40] C. Liu, S. Liu, C. Zhang, Y. Huang, and H. Wang, “Multipath propagation analysis and ghost target removal for FMCW automotive radars,” in IET International Radar Conference (IET IRC 2020), vol. 2020, 2020, pp. 330–334.

[41] S. S. Blackman, Design and analysis of modern tracking systems, ser. Artech House radar library. Boston, Mass. ; London: Artech House, 1999.

[42] E. Brookner, Tracking and Kalman filtering made easy. New York: Wiley, 1998.

[43] “Canalyzer sofwtare product page,” accessed on 08/05/2023. [Online]. Available: https://www.vector.com/it/it/prodotti/products-a-z/software/canalyzer

[44] “Iso 17387:2008 - intelligent transportation system lane change decision aid systems (lcdas) performance requirements and test procedures,” accessed on 26/05/2022. [Online]. Available: https://www.iso.org/standard/43654.html

[45] E. Bel Kamel, A. Peden, and P. Pajusco, “Rcs modeling and measurements for automotive radar applications in the w band,” in 2017 11th European Conference on Antennas and Propagation (EUCAP), 2017, pp. 2445–2449.

[46] M. Caffa, F. Biletta, and R. Maggiora, “Binary-phase vs. frequency modulated radar measured performances for automotive applications,” Sensors, vol. 23, no. 11, 2023.

[47] M. Bauduin and A. Bourdoux, “Mixed-signal transmitter leakage cancellation for pmcw mimo radar,” in 2018 15th European Radar Conference (EuRAD), 2018, pp. 293–296.

[48] W. Van Thillo, V. Giannini, D. Guermandi, S. Brebels, and A. Bourdoux, “Impact of adc clipping and quantization on phase-modulated 79 ghz cmos radar,” in 2014 11th European Radar Conference, 2014, pp. 285–288.

[49] "Uhnder-digital code modulation (dcm) , radar for automotive application," accessed on 11/10/2022. [Online]. Available: https://www.uhnder.com/images/data/DCM_Radar_for_Automotive_Application_Final.pdf

[50] K. V. Mishra, B. S. M. R., V. Koivunen, B. Ottersten, and S. A. Vorobyov, "Toward millimeter wave joint radar-communications: A signal processing perspective," 2019. [Online]. Available: https://arxiv.org/abs/1905.00690

[51] "Awr1843boost product page," accessed on 10/11/2022. [Online]. Available: https://www.ti.com/product/AWR1843BOOST/part-details/AWR1843BOOST

[52] "Admv7320 product page," accessed on 20/11/2022. [Online]. Available: https://www.analog.com/en/products/admv7320.html

[53] "Admv7420 product page," accessed on 20/11/2022. [Online]. Available: https://www.analog.com/en/products/admv7420.html

[54] "At-lna-6090-1805t product page," accessed on 15/01/2023. [Online]. Available: https://www.atmicrowave.com/uploads/PDF/AT-LNA-6090-1805T.pdf

[55] "Adf5610 product page," accessed on 15/11/2023. [Online]. Available: https://www.analog.com/en/products/adf5610.html

[56] "Amd kintex7 fpga kc705 evaluation kit product page," accessed on 28/12/2023. [Online]. Available: https://www.xilinx.com/products/boards-and-kits/ek-k7-kc705-g.htmll

[57] "Ad9680 chip product page," accessed on 8/01/2023. [Online]. Available: https://www.analog.com/en/products/ad9680.html

[58] "Fmcdaq2 evaluation board product page," accessed on 09/01/2023. [Online]. Available: https://www.analog.com/en/design-center/evaluation-hardware-and-software/evaluation-boards-kits/eval-ad-fmcdaq2-ebz.html

[59] "Jesd204b high speed serial interface," accessed on 10/01/2023. [Online]. Available: https://www.intel.it/content/www/it/it/products/details/fpga/intellectual-property/interface-protocols/jesd204b.html

[60] M. Golay, "Complementary series," IRE Transactions on Information Theory, vol. 7, no. 2, pp. 82–87, 1961.

[61] M. G. Parker, K. G. Paterson, and C. Tellambura, Golay Complementary Sequences. John Wiley Sons, Ltd, 2003.

[62] K. Harman and B. Hodgins, "The next generation of guidar technology," in 38th Annual 2004 International Carnahan Conference on Security Technology, 2004., 2004, pp. 169–176.

[63] J. R. Centre, I. for the Protection, S. of the Citizen, J. Chareau, and J. Fortuny-Guasch, Radar cross section measurements of pedestrian dummies and humans in the 24/77 GHz frequency bands : establishment of a reference library of RCS signatures of pedestrian dummies in the automotive radar bands. Publications Office, 2013.